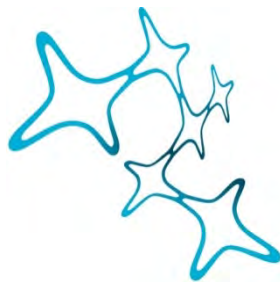


A biophysical exploration of the motion vision pathway in *Drosophila*

Jonatan G. Malis



Graduate School of
Systemic Neurosciences
LMU Munich



Dissertation der Graduate School of
Systemic Neurosciences der Ludwig-
Maximilians-Universität München

March 2nd, 2022

Supervisor
Prof. Dr. Alexander Borst
Max Planck Institute of Neurobiology, Martinsried, Germany

First Reviewer: Prof. Dr. Alexander Borst
Second Reviewer: Prof. Dr. Ruben Portugues
External Reviewer: Dr. Katrin Vogt

Date of submission: March 2nd, 2022
Date of Defense: June 13th, 2022

„Und die Erkenntnis selber: mag sie für Andere etwas Anderes sein, zum Beispiel ein Ruhebett, oder eine Unterhaltung, oder ein Müßiggang, – für mich ist sie eine Welt der Gefahren und Siege, in der auch die heroischen Gefühle ihre Tanz- und Tummelplätze haben. ‚Das Leben ein Mittel der Erkenntnis‘ – mit diesem Grundsatz im Herzen kann man nicht nur tapfer, sondern sogar fröhlich leben und fröhlich lachen!“ (Nietzsche, 1882)

SUMMARY

The ability of neurons to filter, to add and subtract, to divide or to multiply synaptic inputs gives any neuronal system a computational ascendancy. Theories of motion vision which explain the capacity to perceive the physical displacement of an image through time, include all of these computational tools. Two essential ingredients of the so-called elementary motion detectors are the temporal filtering of signals and the performance of nonlinear arithmetic operations. In other words, light signals coming from two points separated in space are filtered so as to create a coincidental synaptic input onto a direction-selective cell. A following nonlinear operation multiplies or divides these signals in order to compute the direction of motion. How such algorithmic steps are biophysically implemented in neurons remains elusive.

In *Drosophila melanogaster*, the motion vision pathway offers an ideal testing ground to explore these questions. Extensive research has led to the discovery of connectivity patterns and to the discovery of the functional properties of neurons in this pathway. Furthermore, the motion vision pathway in fruit fly is constrained to a relatively small circuit of stereotypical columnar neurons whose somata are readily accessible for electrophysiological recordings *in vivo*. In this context, the main focus of my thesis was the investigation of the cellular and biophysical substrate of 1) the nonlinear operation happening at the level of the dendrites of primary motion sensing T4 neurons and 2) the differential temporal filtering ascribed to the presynaptic partners of T4 neurons. In this cumulative thesis, my findings are presented chronologically.

In **manuscript 1**, my co-authors and I recorded the membrane potentials of direction-selective T4 neurons and of their columnar input elements in response to visual and pharmacological stimuli *in vivo*. We showed that a multiplication-like operation essential to the computation of direction selectivity arises from the release of glutamatergic inhibition and a coincident cholinergic excitation.

In **manuscript 2**, we recorded the membrane potentials of Mi9, Tm3, Mi1, Mi4, and C3 neurons in response to visual stimuli *in vivo*. We showed that the differential filtering of the columnar inputs to T4 neurons, the first stage of the elementary motion detector, emerges from the architecture of a passive network. Taken together, these manuscripts exemplify the biological implementation of an algorithmic model of motion detection.

CONTENT

INTRODUCTION	1
1.1 Neurons as electrical elements of a biological circuit	1
1.1.1 Branching in history	1
1.1.2 Neurons as biological elements of an electrical circuit	1
1.1.3 Transmembrane ion channels	3
1.2 Signal Processing	4
1.2.1 Delay	5
1.2.2 Low-pass filtering	5
1.2.3 Band-pass filtering	6
1.3 Biological arithmetic	10
1.3.1 Addition	10
1.3.2 Subtraction	12
1.3.3 Multiplication and division	13
1.4 Motion vision and correlation-type motion detectors	16
1.4.1 Optomotor response	16
1.4.2 Hassenstein–Reichardt detector	17
1.4.3 Barlow–Levick detector	18
1.5 <i>Drosophila</i> and the insights it brings	19
1.5.1 The genetic toolbox of <i>Drosophila</i>	19
1.5.2 Functional imaging	21
1.5.3 Anatomical reconstructions of neural circuits	21
1.5.4 Electrophysiology	22
1.6 Motion vision in <i>Drosophila</i>	23
1.6.1 Columnar system	23
1.6.2 T4 neurons and their inputs	26
1.7 Concluding words	30
MANUSCRIPTS	32
2.1 Manuscript 1: A biophysical account of multiplication by a single neuron	32
2.2 Manuscript 2: Differential temporal filtering in a small neuronal network	58
DISCUSSION	95

3.1 Mechanisms of direction selectivity in T4 cells	95
3.1.1 Differential filtering of input signals to T4	95
3.1.2 Multiplication-like arithmetic on T4 dendrites	98
3.1.3 Mechanisms of null direction suppression	99
3.1.4 Other nonlinearities	100
3.2 Biophysically realistic, conductance-based modeling	102
3.2.1 Single- vs. multi-compartmental modeling	103
3.2.2 Parameter Search	104
3.2.3 Assessment of parameter-estimation	106
3.2.4 Simulator-based models	107
3.3 Temporal filtering strategies in the optic lobe	108
3.3.1 Feedforward network motifs	109
3.3.2 Feedback network motifs	110
3.3.3 Hyper-motifs	111
3.4 Conclusion and outlook	113
BIBLIOGRAPHY	115
APPENDIX	127
5.1 Acknowledgements	127
5.2 Curriculum Vitae	128
5.3 Affidavit	129
5.4 List of manuscripts and author contributions	130

LIST OF FIGURES

- Figure 1.** Representation of an axon membrane as an equivalent circuit.
- Figure 2.** Network architecture and time constants.
- Figure 3.** Frequency-dependent properties of R, RC, RLC circuits and of a neuron.
- Figure 4.** Prerequisites for neurons with intrinsic band-pass filter properties.
- Figure 5.** Table comparing addition with the Boolean logical OR operator.
- Figure 6.** Table comparing multiplication with the Boolean logical AND operator.
- Figure 7.** AND-NOT applications.
- Figure 8.** The optomotor response.
- Figure 9.** Hassenstein–Reichardt detector.
- Figure 10.** Barlow–Levick detector.
- Figure 11.** Gal4-UAS system crossing scheme.
- Figure 12.** *Drosophila*'s optic lobe.
- Figure 13.** Inputs to the ON motion circuit.
- Figure 14.** Direction-selective T4 neurons.
- Figure 15.** Gradient descent and output of the fit function in parameter space.
- Figure 16.** Compensating degeneracy.
- Figure 17.** Feedforward loop motifs.
- Figure 18.** Feedback loop motifs.
- Figure 19.** Feedforward in disguise.
- Figure 20.** Direction selectivity at single boutons.

INTRODUCTION

1.1 Neurons as electrical elements of a biological circuit

1.1.1 Branching in history

In the 19th century, the appearance of the *neuron doctrine* draws attention to one of the building blocks of the nervous system (the **neuron**) (de Castro, 2019). This doctrine states that the nervous system is composed of a multitude of small cells which are interconnected to create a network. Golgi staining performed by Santiago Ramon y Cajal at the beginning of the 20th century lead the *neuron doctrine* to become the accepted theory (de Castro, 2019). Once the *neuron theory* is accepted, it becomes clear that if one wants to understand the workings of the human brain, he or she needs to understand what the neurons are and how they interact with one another.

1.1.2 Neurons as biological elements of an electrical circuit

If the nervous system is made of many single cells assembled into complex networks, it follows that neurons need strategies to encode, transmit, and decode information. The popularization of the *neuron theory* sees with it the rise of **electrophysiology**. In 1874, Ludimar Hermann proposes that changes in the potential of regions of an axon lead to small electrical impulses. He describes these impulses as ‘Strömchen’¹ down the neuron’s axis and through its ‘Hüllen’² (Hermann, 1874). Following Hermann’s lead, Julius Bernstein’s membrane hypothesis introduces the idea that the **membrane** of a neuron must during an electrical impulse lower its resistance in order to allow for the necessary flow of ions (Hille, 1991; Seyfarth and Peichl, 2002). This implies that a neuron has electrical properties and that these properties are dependent on the composition of its membrane, on the intracellular and extracellular ionic concentrations, and on conductances. The conductance is the ease with which charges flow across the membrane for a given voltage difference. By placing the membrane of the neuron at the center of its function, Hermann and Bernstein pave the way for a generation of electrophysiologists who revolutionize the field of neuroscience through their kinetic description of membrane permeability (Hille, 1991). In 1949, the sodium hypothesis, which correctly blames the positive

¹ Small currents

² Now known as the phospholipid polar bilayer membrane

overshoot during action potentials on increased permeability to Na^+ ions is proven by Hodgkin and Katz (Hodgkin and Katz, 1949). The voltage-clamp technique and its use as a direct measurement of ion flow through the membrane solidifies between 1949 and 1952. Thereafter, the electrical properties of a neuron arise from 1) the neuron's membrane made of a phospholipid bi-layer with high resistance, and 2) the difference in ionic concentrations in and outside the neuron. This creates electromotive forces on either side of the membrane and a **potential**.

The movement of ions across a membrane with high resistance is an essential characteristic of neurons. Hodgkin and Huxley propose the modeling of a piece of the giant squid's axon's membrane as a resistor–capacitor **equivalent circuit**. The circuit contains a **capacitor** representing the dielectric property of the membrane, three conductive branches representing the Na^+ , K^+ , and leak conductances with their respective electromotive forces, as well as **resistors** representing the time- and voltage-varying resistances (ref. Hodgkin and Huxley, 1952a; Fig. 1). In Hodgkin and Huxley's equivalent circuit, the Na^+ - and K^+ -associated conductances g_{Na} and g_{K} can be calculated as

$$g_{\text{Na}} = \frac{I_{\text{Na}}}{E - E_{\text{Na}}} \quad (1)$$

$$g_{\text{K}} = \frac{I_{\text{K}}}{E - E_{\text{K}}} \quad (2)$$

Here, I_{Na} and I_{K} are the respective Na^+ and K^+ currents, E is the membrane potential, and E_{Na} and E_{K} are the respective reversal potentials of Na^+ and K^+ (Hodgkin and Huxley, 1952a). Using the *Nernst equation*, the relationship between reversal potential and the ionic concentrations inside and outside the neuron can be expressed for E_{Na} and for E_{K} as

$$E_{\text{Na}} = \frac{RT}{zF} \ln \frac{[\text{Na}]_o}{[\text{Na}]_i} \quad (3)$$

$$E_{\text{K}} = \frac{RT}{zF} \ln \frac{[\text{K}]_o}{[\text{K}]_i} \quad (4)$$

Here, R is the gas constant, T is the absolute temperature on the Kelvin scale, z is the charge of the ion, F is Faraday's constant, $[x]_o$ is the external concentration of ion x , and $[x]_i$ is the internal concentration of ion x . Owing to the electrical properties of its membrane, the single neuron is thus represented as an electrical element. When assembled into networks, neurons become part of an electrical circuit.

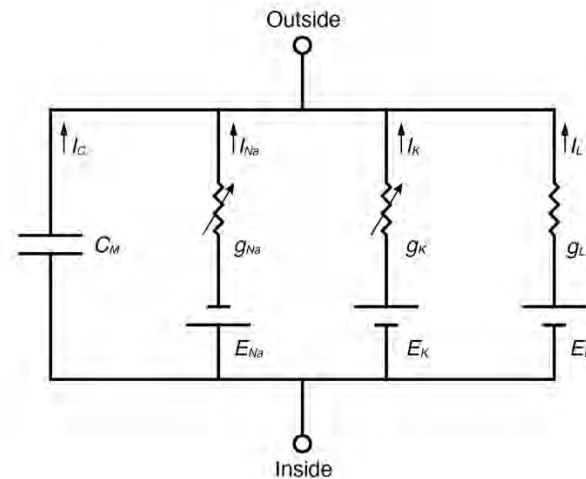


Fig. 1. Representation of an axon membrane as an equivalent circuit

Outside (top) and inside (bottom) are the extra-cellular and intra-cellular space, respectively. I_C , I_{Na} , I_K , and I_L are the respective capacitive, sodium, potassium, and leak current densities. C_M is the membrane capacity per unit area. E_{Na} , E_K , and E_L are the respective equilibrium for Na^+ , K^+ , and for the leak. They create the electromotive batteries (bottom). g_{Na} , g_K , and g_L are the three conductive branches for Na^+ , K^+ , and for the leak conductances. The resistances with arrows through them represent the non-linear time- and voltage-varying conductances dependent on voltage-gated ion channels (Hille, 1991; Hodgkin and Huxley, 1952a).

1.1.3 Transmembrane ion channels

The electrical properties of the neuron arise from the potential appearing at the level of the cell membrane. The maintenance and the changes applied to the membrane potential are controlled by an abundance of differently specialized transmembrane proteins. These proteins let specific ions flow across the membrane (Hille, 1991). As shown in (Fig.1), changes applied to the membrane potential do not follow a linear process. Non-linear time- and voltage- varying conductances depend on the identity and kinetics of specific transmembrane channels.

Among the different types of channels, **Voltage-gated ion channels** are sensitive to local changes in the membrane potential. In other words, movements of the membrane potential away from the resting membrane potential lead to conformational changes of the pore of the channel. These conformational changes allow for the passage of ions. Some of these channels are sensitive to the **depolarization** of the membrane (Warmke et al., 1997) while others respond to its **hyperpolarization** (Brown et al., 1979; Difrancesco and Ojeda, 1980; Masuda et al., 2006). Voltage-gated ion channels are permeable to Na^+ (Hille, 1991; Warmke et al., 1997), Ca^{2+} (Catterall, 1998), or K^+ (Frolov et al., 2012; Hille, 1984; Kamb et al., 1987). Because neurons are reliant on their ion channels, the specific expression levels and the subcellular localization of these proteins on the membrane can allow

for complex biological signal processing. Such signal processing can underlie signal filtering and arithmetic operations performed by neurons. This is reviewed in more detail in sections 1.2 and 1.3.

Ionotropic receptors for their part, are ligand-gated ion channels. They are present in high concentrations in so-called chemical synapses. These synapses are structures formed between two neurons. Synapses are specialized in mediating chemical communication between neurons via the use of **neurotransmitters**. It is only upon binding of specific ligands that the ionotropic receptors allow ions to cross the membrane. A special case are N-methyl-D-aspartate (NMDA) receptors, which additionally require membrane depolarization (Nowak et al., 1984). Further description of the specificity of NMDA receptors and of its implication in neuronal computations are reviewed in 1.3.3. The ions which can pass through ionotropic pores include Na^+ , Cl^- , Ca^{2+} , or K^+ (Cascio, 2004). Endogenous ligands binding to these channels include acetylcholine (ACh), λ -aminobutyric acid (GABA), and glutamate (Glu). Furthermore, many monoamines such as serotonin, histamine, or octopamine (in *Drosophila*) can act as neurotransmitters or as neuromodulators.

Gap junctions are yet another type of transmembrane protein allowing for the communication of signals between neurons. They are found in the so-called electrical synapse. Gap junctions consist of a pair of connexons. One connexon is in the presynaptic cell membrane and one is in the postsynaptic cell membrane (Unwi and Zampighi, 1980). Together, these connexons form a continuous bridge between neurons allowing the passage of inorganic ions and of small organic molecules (Nielsen et al., 2008).

Thus, conductances introduced in the neuron by its transmembrane ion channels do not only allow a control of its membrane potential. They are also the basis of the communication between neurons in a network.

1.2 Signal Processing

Neurons are electrical elements assembled into complex neuronal circuits. They can communicate with one another via chemical or via electrical synapses. If the activity in the brain is reduced to a complicated set of computations emerging from these neuronal circuits (Groschner and Miesenbock, 2019), then the timing at which each single neuron communicates information to its post-synaptic partners is of utmost importance. As Buzsáki puts it, the brain is a “foretelling device”, and its “activity

can be tuned to become an ideal observer of the environment” (Buzsáki, 2006). In other words, brains have developed strategies to optimally process environmental cues which are important to the animal. One of these strategies is the creation of a delay between two sensors.

1.2.1 Delay

Delays result from the distance in space between two spatially offset sensors. They allow for a temporal or spatial control of neuronal activity in response to environmental cues. To avoid confusion, in this section, delay refers to the timing difference of environmental signals (such as sound or moving visual stimuli) resulting from the distance in space of two or more sensors. On the other hand, “filtering” refers to a set of strategies implemented by the brain so as to change the timing of individual circuit elements. The implementation of delays in the brain is clearly exemplified by the use of interaural time differences in sound processing (Darrow et al., 2006). Shortly, the distance between the two ears (interaural) creates an asymmetry in the processing of sounds emitted from a point in space. The localization of the provenance of sounds is possible if an array of detectors of **coincident inputs** is created using axons with different lengths (Jeffress, 1948). The ability to localize the provenance of a sound is vital to nocturnal animals such as the barn owl where the implementation of coincidence detector arrays has been found (Carr, 1993). In mammals, the use of filtering lines implemented by differential axonal lengths at the level of the bushy cells of the cochlear nucleus allows for a temporal control of the signals relayed to coincidence detectors in the medial superior olive (Yin, 2002).

As implied by Jeffress, in order to detect specific environmental cues, the brain needs 1) to create a delay resulting from the spatial offset of sensors, 2) mechanisms to differentially filter the delayed signals, and 3) mechanisms to compare these signals.

1.2.2 Low-pass filtering

Filters are a general means of changing the timing of individual circuit elements. A way to differentially filter signals is to use **low-pass** filters. A low-pass filter is a filter which passes signals with a lower frequency than its cut-off frequency. It attenuates signals with a higher frequency than its cut-off frequency. In electronic circuits, a simple way to low-pass filter a signal is to make use of resistors and of capacitors. Since the phospholipid membrane of the neuron acts as an RC circuit (Hodgkin and Huxley, 1952a), it is equipped with the tools necessary to build a low-pass filter (Koch, 1999). Theoretically, if all non-linearities such as voltage-gated or ionotropic

channels are taken out, what is left is a neuron with a **passive membrane** with capacitor-like and with resistor-like properties. This passive cell membrane can then be simplified as a core-conductor cable (Rall, 1959). The description of the evolution of electrical potentials along the cell membrane can thereafter be modelled with *cable theory* (Koch, 1999; Rall, 1959).

One way to increase the low-pass filtering properties of a passive dendrite is to increase its cable length and thereby increase propagation delays between the centroid (the center of gravity) of a transient current input at a point on the membrane and the centroid of the resulting transient voltage response at another point along the membrane (Agmon-snir and Segev, 1993). Hence, by reducing the diameter of its projections or by spatially segregating its non-linear conductances, a neuron can low-pass filter the signals it is receiving. In summary, a neuron's passive membrane itself is already the equivalent of a linear low-pass filter and the choice of its physical properties, such as its length or its nonlinear conductances, can allow to tune its time constant.

1.2.3 Band-pass filtering

The implementation of differential low-pass filtering strategies by neural circuits could allow for the coincidental detection of signals. However, the use of frequency-domain techniques to study the brain (Puil et al., 1986) has highlighted the existence of stereotypical **frequencies** underlying the rhythmic activation of neuronal populations (Steriade et al., 1990). The presence of these rhythms (Buzsáki, 2006) is a hint to the existence of different modes of dynamical organization in the brain. In other words, the existence of these rhythms implies that neurons or populations of neurons possess frequencies at which they are preferentially activated. This indicates the implementation of **band-pass** filtering strategies in the brain. A band-pass filter passes signals within a specific range of frequencies (band). It attenuates signals with frequencies outside this band. Two explanations for these rhythms exist. Either 1) rhythms arise from the pattern of connections between neurons in re-entrant or in recurrent neural circuits (Traub and Miles, 1991) or 2) neurons behave as oscillatory subunits possessing an intrinsic frequency preference (Llinas, 1988). In both cases, neurons create the equivalent of a band-pass filter.

1) If the rhythms seen in the brain arise from the patterns of connections between neurons, it is the architecture of the circuit itself in conjunction with the dynamic properties of synapses which allow for the differential filtering of neuronal inputs (Traub and Miles, 1991). Here, the connectivity of the network dictates the time

constants assigned to each neuron. How the architecture of a circuit tunes the time constant of neurons can be shown by modelling neuronal responses in a simple network. Let us consider a network containing three neurons each acting as a low-pass filter. If the neurons are all excitatory and connected in a feedforward manner, the time constant of neuron n is larger than the time constants of neuron $n-1$. Each neuron thus responds as a differently tuned low-pass filter to a step input signal (Fig 2a). If one excitatory neuron and one inhibitory neuron with different time constants are connected to a third neuron, the third neuron can respond as a band-pass filter to a step input signal (Fig. 2b) (Cruse, 2009).

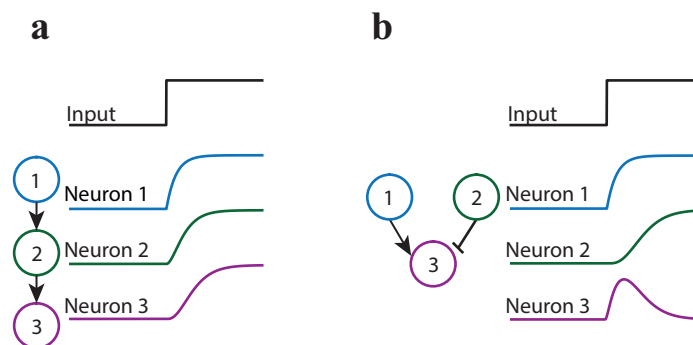


Fig. 2. Network architecture and time constants

(a) Three neurons are connected in a feedforward manner. Each neuron low-pass filters the signals it receives. Neuron 1 receives a step input signal. The time constant of each neuron increases at each new level of the network. **(b)** Neuron 3 receives excitatory inputs from neuron 1 and inhibitory inputs from neuron 2. Both neuron 1 and neuron 2 receive the same step input signal. Neuron 1 and neuron 2 have different time constants. When neuron 1 and neuron 2 are activated by a step input signal, the response of neuron 3 can resemble a band-pass filter.

The use of recurrent neural circuits as filtering strategies in the visual circuit of *Drosophila melanogaster* is explored in **manuscript 2** and is further reviewed in section 3.3.

2) If neurons possess an inherent frequency preference, the source of the differential filtering is to be found in the membrane properties of individual cells. For single neurons to become band-pass filters, two mechanisms are needed (Hutcheon and Yarom, 2000). Neurons need to possess a mechanism creating a **resonance** as well as a mechanism amplifying this resonance into an **oscillation** (Fig. 3). Because oscillations only occur at resonant frequencies, the conjunction of both mechanisms results in the equivalent of a “notch filter” capable of rejecting inputs at frequencies outside the band-pass (Hutcheon and Yarom, 2000).

Resonance

The mechanism responsible for the resonance can be pictured as the simultaneous use of a **low-pass filter**, which attenuates voltage responses to inputs arriving at high frequencies, and of a **high-pass filter**, which attenuates voltage responses to inputs arriving at low frequencies. When the respective cut-off frequencies of both filters are far enough from one-another, this creates a frequency window where resonance occurs. The passive membrane itself already fulfills the role of the low-pass filter (Fig. 3b). However, the high-pass filter which is generally represented as an inductor in electrical circuits (Fig. 3c) is more complicated to reproduce in biological membranes (Fig. 3d). The combination of specific voltage-gated ion channels allows for the creation of the equivalent to a high-pass filter. To create a high-pass filter, the currents elicited by these voltage-gated channels must follow two criteria.

First, these currents must directly **oppose** the voltage changes of the membrane. An example of such currents are the inwardly rectifying *hyperpolarization-activated* I_h currents (Brown et al., 1979; DiFrancesco, 1981; Hauswirth et al., 1968). Indeed, when the reversal potential of a channel allowing these currents falls at the base of its activation curve, this channel can actively oppose changes in the membrane voltage (Hutcheon and Yarom, 2000).

Second, these channels must activate **slowly** in comparison with the membrane time constant. The gap between the low-frequency regions of attenuation established by the opposing currents and the high-frequency regions of attenuation established by membrane time constant defines the width of the resonance **band-pass**. In other word, resonance can only arise at intermediate frequencies where inputs induce voltage changes at frequencies too high to be opposed by the ‘slow’ opposing channels and too low to be counteracted by the passive properties of the membrane (Hutcheon and Yarom, 2000).

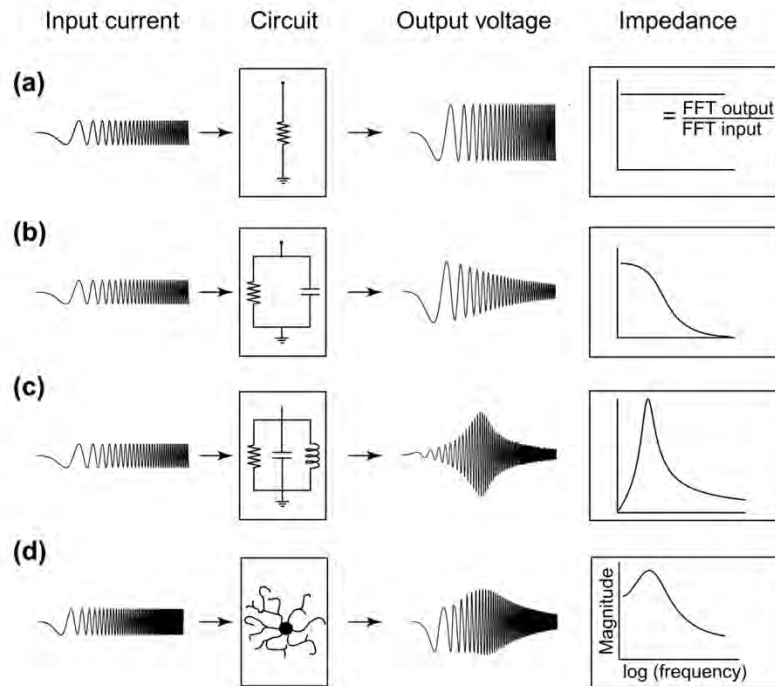


Fig. 3. Frequency-dependent properties of R, RC, RLC circuits and of a neuron

The transformation of a chirp input current (Llinas, 1988) when it is passed through various electrical circuits or through a neuron exhibiting band-pass filtering properties. The quantification of the transformation (impedance) is calculated by dividing the Fourier spectrum (calculated using the Fast Fourier Transform) of the output signal by the Fourier spectrum of the input signal. The resulting magnitude is plotted along a frequency axis (right). **(a)** When the input currents are passed through a circuit containing only a resistor it does not result in a low-pass or in a band-pass filtering. **(b)** When the input current is passed through a circuit containing a resistance and a capacitance (RC model of the membrane) (Hodgkin and Huxley, 1952b), the output is low-pass filtered. **(c)** If the input current is passed through a resistance, capacitance, and inductor (RLC) circuit, the output is band-pass filtered. **(d)** Expectation of the band-pass filtering properties of a neuron from the interaction between the membrane's low-pass filtering property with slow opposing and fast amplifying currents. Image taken with permission from Hutcheon and Yarom, 2000.

Oscillation

The conjunction of both the low-pass filtering properties and the high-pass filtering properties of the membrane creates the equivalent of a resonance band-pass in the neuron (Puil et al., 1986). Yet, the existence of this resonance is of little help if it is not appropriately **amplified**. Such amplification is allowed by the addition of voltage-gated ion channels whose reversal potentials are at the top of their activation curves and which activate quickly in comparison with the membrane time constant. The persistent Na^+ current I_{NaP} (Cummins et al., 1994; Stafstrom, 2007) or the I_{NMDA} (Nowak et al., 1984) current fulfill these criteria. A summary of the prerequisites for resonance and amplification is shown in (Fig. 4)

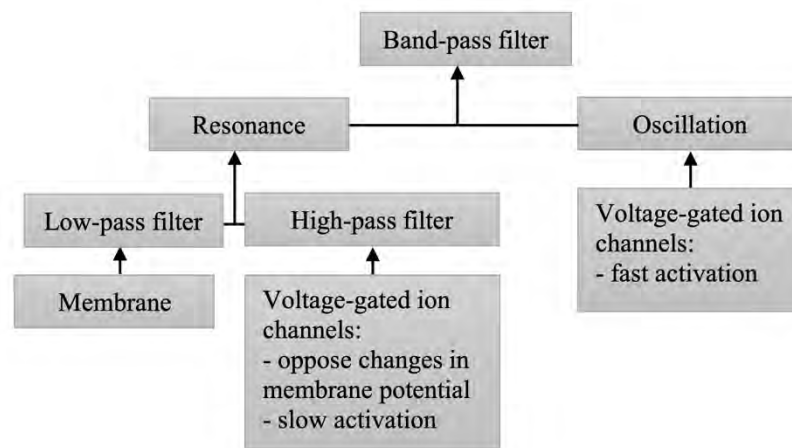


Fig. 4. Prerequisites for neurons with intrinsic band-pass filter properties

A band-pass neuron needs mechanisms to create both a resonance and an oscillation. The resonance comes from the low-pass filtering property of the membrane and from the high-pass filtering property of opposing and slow activating voltage-gated ion channels. The oscillation is a product of fast activating voltage-gated ion channels (Hutcheon and Yarom, 2000).

1.3 Biological arithmetic

Filters are a general means of changing the timing of individual circuit elements. They can be used to adjust the timing of two synaptic input signals onto a cell so as to make them coincide. Following this coincidence, mechanisms to compare these inputs are needed.

1.3.1 Addition

The comparison between two synaptic inputs can be modelled as a basic arithmetic operation. What operation is used and the extent of its nonlinearity are fundamental parameters to the models created to acquire a mechanistic understanding of the brain. The **addition** of two excitatory synaptic inputs by a cell is an intuitive operation as one can simply linearly add the various synaptic inputs a neuron receives. In models of neuronal networks, addition is comparable to the use of the Boolean logical inclusive **OR** operator (ref. Schnupp and King, 2001; Fig. 5). If a neuron receives two inputs, A and B, which are either equal to 0 or to 1, it is only when $A = 0$ OR $B = 0$ that the neuron is silent. The rest of time, it is active. Early models of neuronal networks made extensive use of this type of addition. However, linear additive arithmetic alone cannot account for the complexity of brain functions (Koch and Segev, 2000).

Plus	0	1	OR	False	True
0	0	1	False	False	True
1	1	2	True	True	True

Fig. 5. Table comparing addition with the Boolean logical OR operator

In the first three columns, two inputs having values of 0 or 1 are added. If both inputs are 0, the output is 0. If both inputs are 1, the output is 2. In the last three columns, the interaction between the same inputs is represented via the Boolean logic operation OR where a neuron is active when the output is True and silent when the output is False. If both inputs are false, the neuron is silent (Schnupp and King, 2001).

Modeling the complexity of brain computations requires nonlinearities (Koch and Segev, 2000). This requirement can be resolved by adding a spike **threshold** to the model (Srinivasan and Bernard, 1976). Thereafter, the firing of a cell's action potential becomes dependent on the threshold established by the voltage-gated Na^+ channels present in its membrane. The **leaky integrate-and-fire neuron** fires an action potential, if the sum of a neuron's inhibitory and excitatory inputs exceeds the threshold established by the voltage-gated Na^+ channels (Lapicque, 1907; McCulloch and Pitts, 1943). Although the inputs are linearly processed, the core of the computational power of such networks is not the implementation of additive arithmetic itself but the non-linear threshold. One can further question the biological applicability of linear additive arithmetic in neurons. For passive membranes, the postsynaptic potential of two simultaneous excitatory synapses is always lower than the linear sum of their excitatory inputs (Koch and Poggio, 1987; Koch and Segev, 2000). As the membrane potential of the post-synaptic cell increases, the excitatory currents automatically decrease (Koch, 1999).

The inevitable sublinear combination of two simultaneous excitatory inputs can be illustrated by a simple electrical equivalent circuit of a passive neuron. This isopotential neuron receives two excitatory inputs x and y , which respectively control the excitatory conductances g_{e1} and g_{e2} (Borst, 2018). The membrane potential V_m at steady state is given by

$$V_m = \frac{(g_{e1}+g_{e2})E_e+g_L E_L}{g_{e1}+g_{e2}+g_L}, \quad (5)$$

where E_e and E_L are the respective reversal potentials of excitatory and of leak currents. g_L is the leak conductance. When V_m is expressed as the difference between V_m and E_L and all the conductances relative to g_L (Borst, 2018), the response of the passive neuron $R_{1,2}$ to the combined excitatory inputs x and y can be written as

$$V_m = E_e \frac{g_{e1}+g_{e2}}{g_{e1}+g_{e2}+1}. \quad (6)$$

If $g_{e1} = x$ and $g_{e2} = y$, the individual responses R_1 and R_2 to each input presented in isolation are

$$R_1 = E_e \frac{x}{x+1} \text{ and } R_2 = E_e \frac{y}{y+1}. \quad (7)$$

Now we can show that for two excitatory inputs, $R_{1,2}$ is always smaller than the linear expectation $R_1 + R_2$:

$$E_e \frac{x+y}{x+y+1} < E_e \frac{x}{x+1} + E_e \frac{y}{y+1}. \quad (8)$$

Factoring out E_e , we obtain

$$\frac{x+y}{x+y+1} < \frac{x}{x+1} + \frac{y}{y+1}. \quad (9)$$

For positive non-zero values of x and y ,

$$\frac{x}{x+y+1} < \frac{x}{x+1} \text{ and } \frac{y}{x+y+1} < \frac{y}{y+1}. \quad (10)$$

It follows that the response of a passive neuron to two coincident excitatory inputs $R_{1,2}$ is always smaller than the linear expectation $R_1 + R_2$ (Extended Data Fig. 5b of manuscript 1). Further description of this sublinearity can be found in the supplementary equations of **manuscript 1**. Ultimately, it is important to remember that biological membranes can at best implement **arithmetic-like** operations.

1.3.2 Subtraction

While **subtraction** cannot be represented via Boolean arithmetic, its use can be evaluated computationally and biologically. Indeed, if the reversal potential of inhibitory inputs becomes very negative (relative to the resting membrane potential), then the influence of the hyperpolarizing electromotive battery starts to dominate the membrane potential. This type of inhibition approaches a linear subtraction (Koch, 1999). A subtraction-like operation is theoretically sufficient in the subtraction stage of the Hassenstein–Reichardt detector (Egelhaaf et al., 1989) which is reviewed in section 1.4.2.

Subtractive arithmetic can be illustrated by the equation for the membrane potential V_m at steady state for a neuron receiving an excitatory and an inhibitory input as

$$V_m = \frac{g_e E_e + g_i E_i + g_L E_L}{g_e + g_i + g_L}. \quad (11)$$

Here, g_e , g_i and g_L are the respective excitatory, inhibitory, and leak associated conductances. E_e , E_i , and E_L are the respective reversal potentials of excitatory, inhibitory, and of leak currents. If V_m is expressed as the difference between V_m and E_L and all the conductances relative to g_L (Borst, 2018), the membrane potential response is

$$V_m = \frac{g_e E_e + g_i E_i}{g_e + g_i + 1}. \quad (12)$$

As E_i reaches more negative values, the equation governing V_m approaches a linear subtraction. Experimentally, the implementation of subtractive arithmetic was elegantly shown to be mediated by Cl^- channels at the level of H-1 cells in *Calliphora erythrocephala* (Egelhaaf et al., 1990).

1.3.3 Multiplication and division

As complex operations are demanded from neuronal networks, the use of nonlinear multiplicative operations between the synaptic inputs made onto a neuron can be computationally advantageous (Koch and Segev, 2000). Once again, Boolean arithmetic gives a useful simplification of how such arithmetic can be understood. While addition is represented by an OR operator, multiplication is defined by the logical AND operator (ref. Schnupp and King, 2001; Fig. 6). If a neuron receives two inputs, A and B, which are either equal to 0 or to 1, it is only when $A = 1$ AND $B = 1$ that the neuron is active. The rest of time, it is silent.

Times	0	1	AND	False	True
0	0	0	False	False	False
1	0	1	True	False	True

Fig. 6. Table comparing multiplication with the Boolean logical AND operator

In the first three columns, two inputs with values of 0 or 1 are multiplied. If both inputs are 0, the output is 0. If both inputs are 1, the output is 1. In the last three columns, the interaction between the same inputs is represented via the Boolean logic AND operation where a neuron is active only when both inputs are True, and silent the rest of the time (Schnupp and King, 2001).

The biological implementation of multiplicative arithmetic can take different forms. It can be achieved via the use of 1) N-methyl-D-aspartate (NMDA) receptors which intrinsically act as AND gates, or via the use of 2) a so-called AND-NOT operator (Barlow and Levick, 1965). AND-NOT operators have the ability to approximate either divisive or multiplicative arithmetic.

1) NMDA receptors are glutamate-gated. They allow the flow of currents mainly composed of Na^+ , K^+ , and of a small fraction of Ca^{2+} ions. Importantly, NMDA-elicited currents also require a local depolarization of the membrane. At resting membrane potential, external Mg^{2+} ions enter the NMDA channel and effectively block it. Local depolarization of the membrane relieves the Mg^{2+} block and thus frees the open pore after binding of glutamate (Nowak et al., 1984). Therefore, a synapse containing NMDA receptors, in conjunction with other depolarizing receptors, acts

as an AND gate since NMDA receptors are only open when presynaptic release of glutamate coincides with membrane depolarization.

2) The biological use of an AND-NOT gate can approximate divisive arithmetic. AND-NOT operations are allowed by the combination of inhibitory and of excitatory inputs onto a cell. The inhibitory input needs to be tonic in some fashion and must additionally exert a so-called “silent inhibition”. Such inhibition occurs when the reversal potential of the inhibitory channels E_i lies close to the leak reversal potential E_L . The opening of “shunting” channels leads to an increase in conductance while no effect on the membrane potential can be distinguished. This type of shunting inhibition can be illustrated using eq. (12).

In cases where $E_i = E_L = 0$ but $0 < g_i \leq 1$, the effect of increases of the inhibitory conductance is **divisive**. The higher the inhibitory conductance is, the more it controls the equation (McKenna et al., 1992):

$$V_m = \frac{g_e E_e}{g_e + g_i + 1}. \quad (13)$$

Shunting inhibition can thus be equivalent to a **division**. Thereafter, in cases where both excitation and silent inhibition coincide, the AND-NOT operator acts as a **veto** (Fig. 7). A theoretical application of AND-NOT veto is found in theories of motion vision (Barlow and Levick, 1965). As exemplified by eq. (13), if both the shunting input and the excitatory input coincide, this results in a sublinearity. The larger g_i is, the larger the extent of the sublinearity becomes.

An AND-NOT operator can also approximate a **multiplication**. In cases where a tonic shunting inhibitory input and its associated Cl^- conductance cease in conjunction with the start of excitatory inputs, the post-synaptic cell is **disinhibited** and its depolarization is **facilitated** (McKenna et al., 1992). This type of facilitation can easily be explained in cases where the inhibitory and the excitatory conductances are temporally shifted so as to follow three distinct steps. First, inhibition is followed by disinhibition. Second, following the disinhibitory step there is a period where the cell does not receive any input (note that this step is not necessary but helps to describe multiplicative facilitation). Third, the lack of input is followed by an excitatory input. Starting from eq. (13) where a tonic silent inhibition is present, during disinhibition g_i approaches 0 while g_e is still 0. This results in an increase of the input resistance I_R (as it is the reverse of the sum of all conductances). For the extreme case where $g_e = g_i = 0$,

$$I_R = \frac{1}{g_e + g_i + 1} = 1. \quad (14)$$

If following (or coinciding with) this increase in I_R , excitatory conductances are opened so that $0 < g_e \leq 1$, then

$$V_m = \frac{g_e E_e}{g_{e+1}}. \quad (15)$$

Consequently, the coincidence of high I_R and of excitatory inputs leads to a multiplicative nonlinearity as it is predicted by Ohm's law:

$$V = I * R. \quad (16)$$

Here, V is the voltage, I is the current, and R is the resistance. I is defined as

$$I = g * E, \quad (17)$$

where g is the conductance. R is defined as

$$R = \frac{1}{g}. \quad (18)$$

V can then be expressed as

$$V = g * E * \frac{1}{g}. \quad (19)$$

In eq. (19), in cases where $E = 0$, changes in R scale I multiplicatively. Using eq. (14), the larger g_i is, the more nonlinear the facilitation resulting from disinhibition becomes. These examples illustrate the importance of the temporal processing of excitatory and of inhibitory input signals to a cell. For an AND-NOT operator, the achievement of multiplicative or of divisive arithmetic depends on the **timing** and on the **polarity** of the respective inputs. The coincidence of disinhibition and of excitation leads to a multiplication-like operation (Fig. 7). A simultaneous shunting and excitation leads to a division-like operation (Fig. 7). Biological evidence for multiplication-like arithmetic is further described in **manuscript 1**.

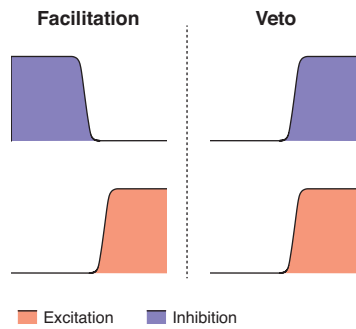


Fig. 7. AND-NOT applications

Input conductances permitting AND-NOT facilitation and veto. Facilitation (left) results from the coincidence of the release from inhibitory conductances (purple) with increase in the excitatory conductances (red). Veto (right) results from the coincidence of inhibitory and excitatory conductances.

Neurons have the ability to compare filtered signals using arithmetic. When coincidence of signals occurs, the conjunction of shunting inhibition and of

excitation results in a division-like operation (veto). The coincidence of the release of shunting inhibition with excitation results in multiplication-like arithmetic (facilitation).

1.4 Motion vision and correlation-type motion detectors

1.4.1 Optomotor response

Armed with the knowledge about signal processing and about the mechanisms to biologically implement arithmetic operations, one might be tempted to try to acquire a complete understanding of how the human brain computes information. However, at present, the complexity of the organ renders it impossible to fully fathom. To overcome this shortcoming, scientists seek insights from the study of innate **behaviors** and **reflexes** in various animal models. The neuronal operations underlying these behaviors and reflexes can then be modelled using signal filtering and arithmetic operations (Götz, 1964; Hassenstein and Reichardt, 1956; Orger et al., 2000). In such a constellation, it is interesting to consider the capacity to sense visual motion, that is the displacement in space of a visual object through time. This ability known as motion perception is a major theme of systems neuroscience. Naturally, the importance of **motion vision** to any animal relying on sight cannot be emphasized enough. Yet, what gives the study of the neuronal computations underlying the ability to detect moving objects an exhilarating incentive, is that it might be simple enough to be fully understood. In zebra fish, in the snout beetle, or in the fruit fly the ability these animals have to distinguish the directionality of a visual stimulus is reflected by their **optomotor** response (Borst et al., 2010; Hassenstein, 1951). For instance, when a walking *Chlorophanus viridis* or a walking *Drosophila melanogaster* is presented with a horizontally moving edge, the animal reflexively turns in the direction of the moving stimulus to counteract the perceived rotation (Fig. 8). Such a behavior which can be reproduced in a controlled environment is a useful window into the perception of the animal.



Fig. 8. The optomotor response

Tethered *Drosophila* walking on an air-cushioned ball which was tracked by cameras. Arbitrary visual stimuli on screens surrounding the animal can be displayed. This

experimental set-up has been used for behavioral experiments in this thesis. Photo by R. Schorner.

1.4.2 Hassenstein–Reichardt detector

In order to understand the computation underlying the ability to sense visual motion, two main **correlation-type** motion detectors were initially proposed. Using the optomotor response of the snout beetle (Hassenstein, 1951), Hassenstein and Reichardt propose a model consisting of multiple elementary motion detectors (Hassenstein and Reichardt, 1956). This model is purely algorithmic and was designed to explain the minimal amount of computation required in order to discriminate the direction of visual motion. At its periphery, the “half-detector” receives signals from two light detectors physically separated in space (Fig. 9). Both photoreceptors give input to a direction-selective cell which multiplies the input signals. The signal of one photoreceptor is delayed relative to the other. This delay is created so that the sequential stimulation of both receptors, in the sequence that would occur during visual motion in the detector’s **preferred direction** (PD), results in the coincidence of the two signals (Fig. 9a). The output signals of two mirrored half-detectors are subtracted at a third stage (Fig. 9c). The “full correlator model” outputs a positive signal for visual motion in PD. It outputs a negative signal for visual motion in the **null direction** (ND). A variation to this model is proposed in the F model where instead of a delay, low-pass filters are used (Thorson, 1966). In the F-H model, the low-pass filter is complemented by the use of a high-pass filter on the opposing arm (Poggio and Reichardt, 1976).

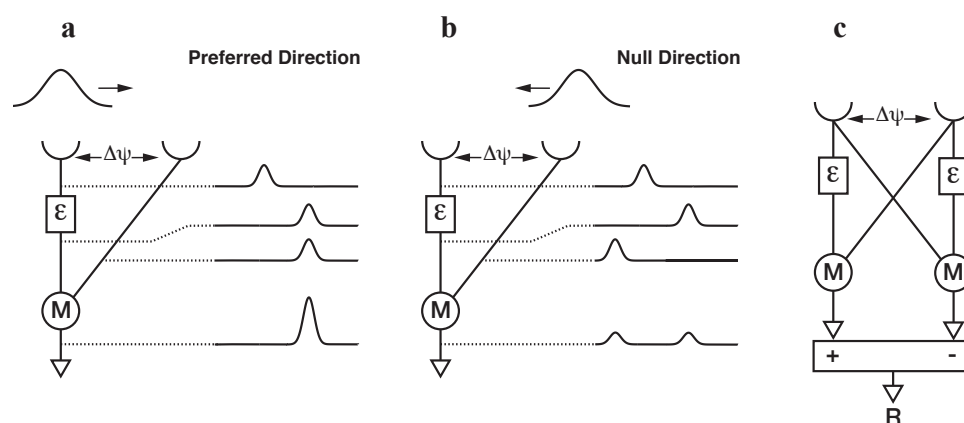


Fig. 9. Hassenstein–Reichardt detector

The input to the correlation-type motion detector is given by the light intensities measured at two points in space by two channels. In each half-detector, signals are multiplied (M) after one of them is delayed by a time interval ϵ (a) When the sequential input signal moves in the preferred direction, the temporal separation of the signal in both channels is compensated in the left arm by ϵ . This allows for a coincidental input of both arms which results in a larger response after the multiplication stage (b) When the sequential input signal moves in the null direction, ϵ increases the delay between both input signals. This results in two separated peaks after the multiplication stage. (c) The full correlation-type motion detector is composed

of mirrored half-detectors where the respective outputs from each multiplication stage are subtracted. Image taken and adapted with permission from Borst and Egelhaaf, 1989.

1.4.3 Barlow–Levick detector

In their study of direction-selective retinal ganglion cells in the rabbit’s retina, Barlow and Levick find evidence for a different mechanism of motion detection (Barlow and Levick, 1965). Similarly to the Hassenstein–Reichardt detector, the **Barlow–Levick** detector relies on the coincidence of two inputs. The half-detector consists of two light detectors one of which is delayed. Here, a nonlinear operation is created by a veto stage. Visual stimulation in the ND allows for the coincidence of an inhibitory input with an excitatory input. The inhibition vetoes the excitation (Fig. 10). By contrast, visual stimulation in the PD creates an inhibition and an excitation that do not coincide. This in turn leads to an excitation of the direction selective unit. In the Barlow–Levick detector, the non-linear inhibitory stage can be represented by a divisive AND-NOT operation or by a subtraction. Noticeably, the Barlow–Levick model does not require a delay of the inhibitory arm in cases where “inhibition simply persists longer than excitation and can thus continue[s] to be effective after a lapse of time” (Barlow and Levick, 1965).

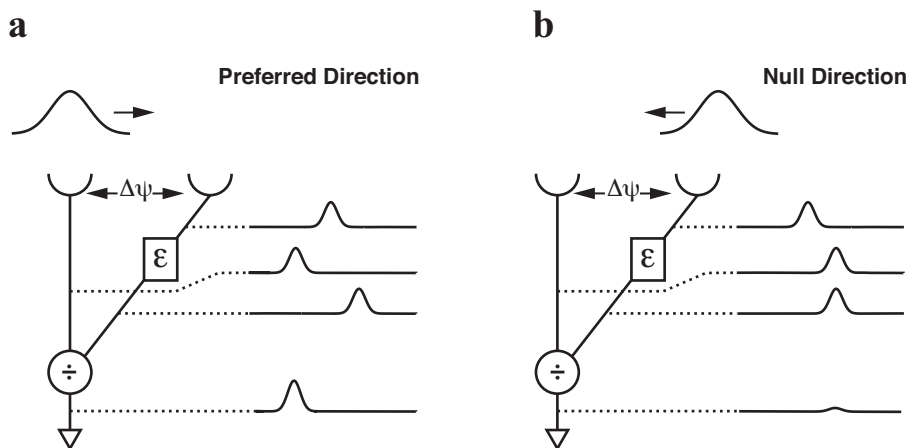


Fig. 10. Barlow–Levick detector

The input to the correlation-type motion detector is given by the light intensities measured at two points in space by two channels. In the half-detector, signals are divided after one of them is delayed by a time interval ϵ . (a) When the sequential input signal moves in PD, ϵ increases the delay between both input signals. This hinders the right arm from vetoing the input from the left arm. The result is a larger response after the division stage. (b) When the sequential input signal moves in the ND, ϵ allows for a coincidental input of both arms. This allows the right arm to veto the input from the left arm and leads to a smaller peak after the division stage (Barlow and Levick, 1965).

1.5 *Drosophila* and the insights it brings

1.5.1 The genetic toolbox of *Drosophila*

In most animal models, the exploration and characterization of the operations performed by neuronal networks are limited by the large number of cells involved in each circuit as well as by the impracticability for systematic recording of the electrical properties of all neurons *in vivo* (Lerner et al., 2016). In *Drosophila melanogaster*, these limitations do not apply. *Drosophila*'s brain contains $199,380 \pm 3,400$ neurons (Raji and Potter, 2021). This is a large enough number of cells in order to support complex computations and behaviors. Yet, it is small enough to attempt to understand the structure and function of the microcircuits it contains. Being one of the most studied animal models since the early 20th century, a great ease in rearing comes with the fruit fly. Furthermore, almost a century of research in diverse fields has given the *Drosophila* scientific community a substantial number of tools. The creative use of these tools has the potential to answer many of the important questions asked within the field of systems neuroscience.

Short life cycles and ease of husbandry are considerable advantages of the fruit fly. Furthermore, the genetic toolbox developed in *Drosophila* makes it a very interesting animal model. Notably, the repurposing of the **UAS-Gal4** yeast binary expression system allows for cell type specific expression of a given transgene. This tool endows the researcher with the ability to target any neuron, cell type, or assembly of cells belonging to a circuit of interest and for which a Gal4 line has been developed (Brand and Perrimon, 1993). At its core, the transcription factor Gal4 (originally derived from yeast) binds to the Upstream Activation Sequence (UAS). This, in turn, activates the transcription of transgenes present downstream of the UAS. Importantly, to express a UAS-transgene in cells of interest, it suffices to cross a fly containing a Gal4 transgene under the control of regulatory sequences (such as promoters or enhancers) with another fly containing the UAS-transgene. The offspring from this cross will possess both the UAS and the Gal4 transgenes (Fig. 11).

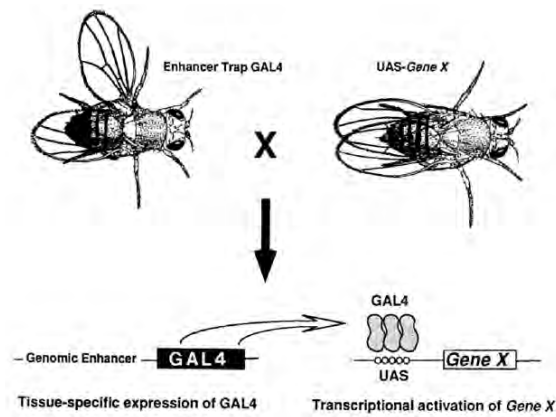


Fig. 11. Gal4-UAS system crossing scheme

A fly with the enhancer trap Gal4 is crossed to a fly with the UAS-*Gene X* to obtain directed gene expression. The enhancer trap Gal4 fly has a genomic enhancer fused to a Gal4 sequence while the UAS-reporter fly has a UAS sequence followed by a *Gene X* of interest (Brand and Perrimon, 1993). The tissue-specific Gal4 binds to the UAS sequence which allows for the expression of *Gene X* in a cell-type-specific manner. Image taken with permission from Brand and Perrimon, 1993.

A common use of the UAS-Gal4 system is the expression of structural markers in cells of interest. It is possible to express cytosolic or membrane-bound fluorescent proteins in targeted cells. The discovery and development of these fluorescent proteins is on its own a leap in scientific accomplishment which cannot be overrated. The *green fluorescent protein (GFP)* is now used across biological sciences to explore the anatomical properties of cells (Chalfie et al., 1994).

The UAS-Gal4 system can also be used in order to shed light into the specific role of genes in *Drosophila*. This is accomplished by means of so-called loss-of-function experiments. Here, the UAS-Gal4 system is not used to explore anatomical properties of targeted cells but to knock down specific genes using RNA interference (**RNAi**). This interference is accomplished via the degradation of mRNA which in turn prevents the translation of proteins of interest (Dietzl et al., 2007; Perkins et al., 2015). It is thus possible to target a cell type via the use of Gal4 constructs so as to deplete it of specific proteins. A major drawback of this approach is the possible developmental repercussion or the unspecific gene targeting resulting from the use of RNAi tools. The use of RNAi might thus create off-target effects and lead to a misinterpretation of experimental results. Its use should therefore be adequately controlled.

1.5.2 Functional imaging

Taking advantage of the ease with which the UAS-Gal4 system permits the expression of any UAS-transgene, systems neuroscience in *Drosophila* has been revolutionized by the ability to perform **functional imaging** experiments. The non-invasive imaging of targeted cell populations *in vivo* is permitted by the use of *genetically encoded calcium indicators (GECI)*. GECI give a readout of the electrical activity of cells in which they are expressed (Miyawaki et al., 1997). Depolarization of the membrane can lead to the opening of voltage-gated ion channels. This, in turn, allows the influx of Ca^{2+} ions into the cell (Hille, 1991). Ca^{2+} conductance is generally linked to the start of cascading signals such as the ones used in exocytosis (Hille, 1991). Because of the small concentration of Ca^{2+} present in the ‘resting’ cell, any influx of Ca^{2+} can readily be detected by GECI. The Ca^{2+} indicator **GCaMP** (Chen et al., 2013; Nakai et al., 2001) consists of a GFP protein which has been fused to the M13 domain of the myosin light-chain Kinase protein which is activated by the calcium-binding protein calmodulin. Calmodulin is an endogenous Ca^{2+} detector present in neurons. With GFP fused to the myosin Kinase, the conformational change of calmodulin upon binding of Ca^{2+} leads to a deprotonation of the GFP chromophore. This results in an increase in fluorescence. The use of GCaMP and of other GECI has clear advantages. Armed with these tools, the simultaneous structural and functional exploration of a vast array of neurons is possible. Nevertheless, GECI only give an approximation of a cell’s electrical activity. The Ca^{2+} signal is itself filtered by the limited forward and backward rate constants of the indicator proteins (Chen et al., 2013). Furthermore, GECI bind to free cytosolic Ca^{2+} which in itself buffers it and might lead to a significant alteration of Ca^{2+} dynamics in the cell and thus to nonlinearities which could perturb the circuit (Borst and Abarbanel, 2007). Finally, because GECI are bound to the non-linear activity of the voltage-gated Ca^{2+} channels, their inactivation via the hyperpolarization of the membrane leads to at least a half-wave rectification of the voltage-to-calcium transformation.

1.5.3 Anatomical reconstructions of neural circuits

The understanding of neuronal networks implies the need for a mapping of each node (neuron) and edge (connection) of the network. The small size of *Drosophila*’s brain renders this tantalizing task achievable. The gold standard of neuronal reconstruction is the use of **electron microscopy (EM)**. EM has a spatial resolution of less than 35 nm (Harris et al., 2006). Because of the high spatial accuracy which comes with it, EM enables the morphological reconstruction of very fine neural processes and

the distinction of single synapses. This does not only allow for the building of connectivity matrices. It can also reveal a neurite's length and diameter. These are both values coveted by biophysicists. They make it possible to model and predict the evolution of electrical potentials across the membrane of traced neurons (Meier and Borst, 2019; Rall, 1959). There exist two main methods to perform circuit reconstructions with EM (Briggman and Bock, 2012). **Serial-section transmission electron microscopy** (ssTEM) involves the small sectioning of a sample followed by the scanning of each section with a transmission electron beam. The process is ended with a manual and time intensive tracing of single neurons and with the determination of their connectivity patterns (Harris et al., 2006). Tracing can however be accelerated with the help of deep neural nets (Dorkenwald et al., 2017). In **serial block-face scanning electron microscopy** (SBF-SEM), the most superficial layer of an embedded sample is imaged. Subsequently, either a diamond knife or a focused ion beam is used to shave off the most superficial and already imaged layer of the sample. This process is repeated until the whole sample has been chiseled off. Both methods come with their own advantages. While the process of the SBF-SEM can be highly automated (Denk and Horstmann, 2004; Xu et al., 2017), the ssTEM method allows to collect and save the samples. In *Drosophila*, recent large-scale projects have allowed the imaging and tracing of important structures in the optic lobe (Rivera-alba et al., 2011; Shinomiya et al., 2019; Takemura et al., 2017).

1.5.4 Electrophysiology

Since the “heroic time of what can be called classical biophysics (1935-1952)” (Hille, 1991), electrophysiology has been the tool of choice to study the electrical properties of neurons. Electroencephalogram, multi-electrode array (Tochitsky et al., 2016), sharp electrode, or inside-out recording are only a few of the many techniques used in order to record the electrical activity of single or of multiple neurons. In *Drosophila*, **whole-cell patch clamp** is the prevailing technique to measure the electrical activity of single neurons *in vivo* (Wilson et al., 2004). Whole-cell patch clamp permits to study the electrical properties of excitable cells and of their ion channels. Towards this, a micropipette filled with an electrolyte solution is attached to the cell membrane so as to form a seal. The breaking through the membrane within this seal allows for the solution in the pipette and the cytosol to mix. Clamping of the membrane is thus made possible. In the **voltage-clamp** recording configuration (Cole and Moore, 1960; Hodgkin et al., 1952), the characterization of the ion flow across a cell's membrane is made possible by measuring the electrical current while

controlling the membrane potential via the use of a feedback amplifier. In the **current-clamp** recording configuration, it is the changes in membrane potential occurring as a consequence of the changes in ion channel activity which are measured. The relatively small size of *Drosophila*'s brain in comparison with mammalian brains renders the performance of whole-cell patch clamp the gold standard of electrophysiology in the fly. However, it is important to keep in mind that even if the somata of many neurons in the optic lobe of the fly are relatively easily accessed, the diameter of most of these somata is much smaller when compared to mammalian neuronal somata. While the soma of a stereotypical pyramidal neuron has a diameter of about 20µm (Wang et al., 2018), the soma of a direction-selective T4 neuron in *Drosophila* is less than 5 µm wide (Fischbach and Dittrich, 1989). Until recently, it was thought that the extremely small size of many neurons in the optic lobe made whole-cell recordings impossible (Gruntman et al., 2018).

1.6 Motion vision in *Drosophila*

Section 1.5 highlights some of the advantages *Drosophila melanogaster* brings to the study of neuronal microcircuits. Notably, the brain of the fruit fly has revealed itself to be auspicious to the study of the biological implementation of textbook models of motion vision (Barlow and Levick, 1965; Hassenstein and Reichardt, 1956). In part, that is because of a stereotypical and repetitive direction-selective circuit where the computation of the direction of motion was found to reside in the dendrites of T4 and T5 neurons (Maisak et al., 2013).

1.6.1 Columnar system

Ommatidia and retina

In the fly, visual information is first processed in the **retina** upstream of the **optic lobes**. *Drosophila* possesses compound eyes divided into 700 to 800 facets where highly precise hexagonal structures called **ommatidia** sequester light input (Kumar, 2012; Zeleny, 1922). In each ommatidium, light is focused with the help of a lens onto **photoreceptors** present in the **retina**. The photoreceptors, in turn, allow for the phototransduction of electromagnetic information into biochemical signals (Montell, 2012). In the retina, increase of light intensity correlates with the increase of photoreceptor activity (Pak and Pinto, 1976). As each ommatidium focuses light onto seven or eight photoreceptors, six of these photoreceptors (R1-R6) are devoted

to detecting changes in light intensity. They cover a spectrum between 360 nm and 475 nm (Heisenberg and Buchner, 1977; Pak and Pinto, 1976). Two photoreceptor types (R7 and R8) are mainly devoted to color vision. They specialize in discriminating changes in the intensity of electromagnetic signals of 375 nm and of 508 nm, respectively (Yamaguchi et al., 2010).

Lamina

The retina and its photoreceptors relay visual information to the optic lobe. Each optic lobe is divided into discrete neuropils: the **lamina**, the **medulla**, the **lobula**, and the **lobula plate** (Fig. 12). Photoreceptors release histamine onto cells of the lamina (the first optic neuropil). Lamina monopolar neurons (L) are hyperpolarized by the histamine released by photoreceptors via the histamine-gated chloride channel HisCl (Hardie, 1989). Lamina monopolar cells L1, L2, L3, and L4 increase their activity with decreasing light intensity. L5 increases its activity with increasing light intensity (Arenz et al., 2017; Drews et al., 2020). Importantly, each lamina cell receives light information in a columnar, **retinotopic** fashion (Fischbach and Dittrich, 1989). There is one exemplar of each lamina monopolar cell per neuro-ommatidium. While photoreceptors mainly release histamine, L2 to L5 are cholinergic and L1 is glutamatergic.

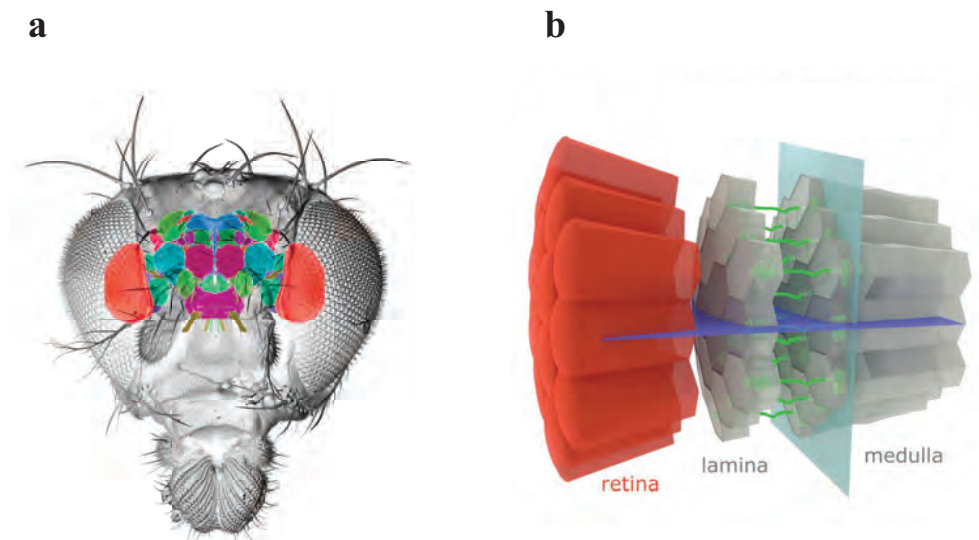


Fig. 12. *Drosophila's* optic lobe

(a) *Drosophila's* head with anatomical representation of the brain. The optic lobes are shown in red. Adapted from illustration courtesy of Kei Ito, Sheena Brown and Nicholas J. Strausfeld. **(b)** Early optic lobe representation where the retina, the lamina, and the medulla can be seen. Lamina projections to the medulla are represented in green. Image taken and adapted with permission from Schützenberger and Borst, 2020.

Medulla

Light information processed in the lamina is relayed to the **medulla** (the second optic neuropil) where transmedullary (Tm), medulla intrinsic (Mi), and centrifugal (C) neurons further process, transform, and relay these signals (Fig. 12 and 13). Once again, spatial information received by the array of Mi, Tm, and C cells is preserved in a columnar fashion. The increasing complexity of the wiring between cells in the medulla contributes to the signal processing. However, the exact contribution of individual connections remains elusive. Lamina, medulla, transmedullary, and centrifugal cells belong to the **ON pathway**, in which neurons respond preferentially to light increments, or to the **OFF pathway**, in which neurons respond preferentially to light decrements (Joesch et al., 2010). This thesis focuses on the implementation of motion vision in the **ON pathway**. The **ON motion pathway** includes Mi9, Tm3, Mi1, and Mi4 neurons (Arenz et al., 2017; Takemura et al., 2017). Noticeably, most of the medulla cells involved in the motion detection circuit possess center-surround antagonistic receptive fields. While Mi1, Tm3, and Mi4 neurons each possess an ON center with some degree of OFF surround, Mi9 has an OFF center and an ON surround (Arenz et al., 2017). Each columnar cell in the lamina and in the medulla preferentially receives inputs from a single neuro-ommatidium. While Tm3 is also a columnar neuron, its receptive field encompasses two neuro-ommatidia.

EM studies have highlighted the recurrent property of the neuronal network in the ON motion pathway (Shinomiya et al., 2019; Takemura et al., 2017). The increasing wiring complexity in the medulla is further complemented by the use of a variety of neurotransmitters. The columnar neuron Mi9 releases glutamate. Columnar Mi1 and Tm3 cells release acetylcholine while columnar Mi4 and C3 neurons release GABA (Davis et al., 2020; Shinomiya et al., 2019; Takemura et al., 2017). In the tenth layer of the medulla, inputs from seven to eight columns are funneled to the dendrites of a single T4 neuron (Fig. 13). Since there is only one Mi9, Tm3, Mi1, Mi4, or C3 neuron per column, the columnar system can be said to dictate the **retinotopy** of the inputs to T4 cells.

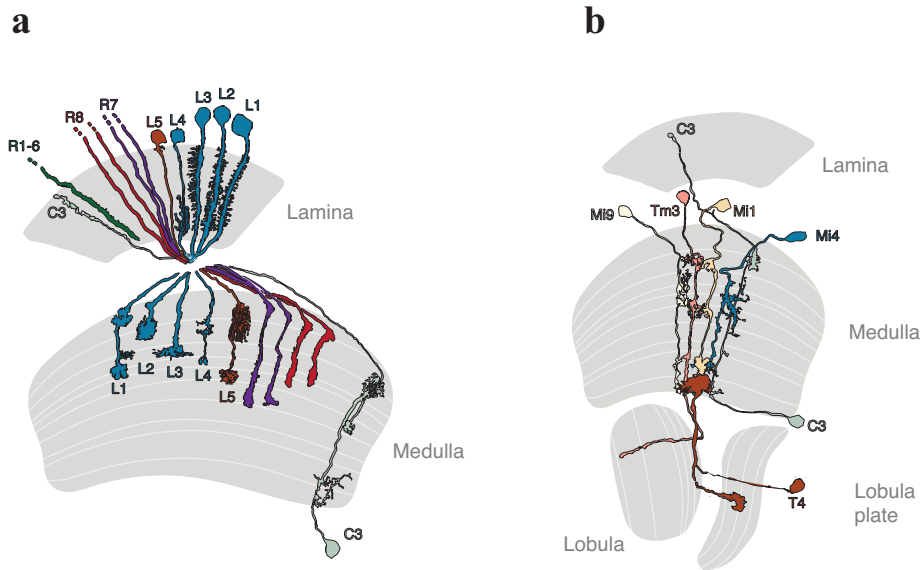


Fig. 13. Inputs to the ON motion circuit

(a) Signals coming from the retina are relayed to the lamina by photoreceptors R1 to R6 (green) and photoreceptors R8 and R7 (red and purple). OFF lamina neurons L1-L4 (blue) relay signals from the lamina to the medulla. ON lamina L5 (burnt sienna) also relays signals from the lamina to the medulla. The chiasm between the lamina and the medulla spatially inverts anterior and posterior signals. (b) Mi9, Tm3, C3, Mi1, and Mi4 are the main columnar inputs to T4 direction-selective neurons.

1.6.2 T4 neurons and their inputs

In the optic lobe, the direction of motion is first computed at the level of the dendrites of T4 neurons (ON pathway) and at the level of the dendrites of T5 neurons (OFF pathway) (Fisher et al., 2015; Maisak et al., 2013). T4 cells are divided into four subtypes, each selective for light increments moving in one of the four cardinal directions (Fig.14a). The use of calcium imaging revealed the presence of both a supralinear and a sublinear response of T4 neurons to PD and ND stimuli, respectively (Haag et al., 2017). Such supralinearity is predicted by the Hassenstein–Reichardt half-detector and could be achieved via a multiplicative operation (Hassenstein and Reichardt, 1956). The sublinearity could result from ND suppression. It would then be achieved via the divisive (or subtractive) stage of the Barlow–Levick detector (Barlow and Levick, 1965). In such a constellation, a detailed characterization of direction-selective T4 cells is facilitated by 1) knowledge about the identity of the neuronal inputs to T4 neurons, 2) knowledge about ionotropic receptors present on T4 dendrites (Fendl *et al.*, 2020), 3) the responses of T4 neurons to the sequential activation of its inputs, and 4) the characterization of the nonlinear operations happening at the level of T4 dendrites.

1) Direction selectivity has been observed in T4 dendrites but not in its inputs (Maisak et al., 2013). Therefore, the nonlinear stage of the detector is likely to reside

at the level of T4 dendrites. As mentioned in 1.6.1, EM studies have allowed to map the majority of the synaptic inputs to T4 neurons (Shinomiya et al., 2019; Takemura et al., 2017). Mi9, Tm3, Mi1, Mi4, C3, TmY15, and CT1 are the major input neurons to a T4 cell. Furthermore, the interaction between T4 and its pre-synaptic partners is spatially stereotyped (Fig. 14b). One T4 neuron gathers inputs from seven to eight columns. Its dendrite is divided in three regions based on intrinsic coordinates: distal (tips), central, and proximal. Inputs to the tips of a single T4 dendrite correspond to the glutamatergic Mi9 cells residing in the concerned columns. On the other hand, the central inputs are mostly mediated by the cholinergic Tm3 and Mi1 neurons contained in different columns than those where Mi9 reside. Finally, inhibitory GABAergic Mi4 and C3 inputs come from yet other columns at the proximal region (Shinomiya et al., 2019; Takemura et al., 2017) (Fig. 14b and c).

2) An advantage of the spatial segregation of T4 inputs is that chemical synapses and thus receptors between T4 and its pre-synaptic partners are also spatially segregated. Using single cell FlpTag (Fendl et al., 2020) as well as UAS-Neurotransmitter-Receptor::GFP transgenes, it was found that the post-synaptic receptor to T4's glutamatergic Mi9 input is the glutamate-gated Cl^- channel $\text{GluCl}\alpha$ (Fendl et al., 2020) (Fig. 14d). Hence, the input Mi9 makes onto T4 is inhibitory (Cully et al., 1996; Liu and Wilson, 2013). Tm3 and Mi1 make cholinergic inputs onto excitatory $\text{D}\alpha 7$ receptors present at the center of the T4 dendrite. GABAergic Mi4 and C3 inputs are localized on the distal side of the dendrite where *Resistant to dieldrin* (Rdl) chloride channels reside (Fendl et al., 2020; Harrison et al., 1996) (Fig. 14d).

3) Because of the columnar retinotopic nature of their input cells, T4 neurons receive light inputs from different points in space. This allows for the creation of a delay in response to moving visual stimuli and is in fact a prerequisite of the correlation-type motion detectors (Fig. 9 and 10). The anatomy of the T4 dendrites reveals its subtype. The distal tips of the dendrites reach in the cell's PD (Fig. 14b). It follows that for a single T4 neuron, the sequential light stimulation of the ommatidium containing its inputs from Mi9, followed by the stimulation of the ommatidium containing its Tm3 and Mi1 inputs, and finally a stimulation of the ommatidium containing its Mi4 and C3 inputs results in an enhanced response (Haag et al., 2016, 2017). Sequential stimulation in the reverse order leads to a suppressed response of the T4 neuron (Gruntman et al., 2018; Haag et al., 2016, 2017). The order in which a T4 cell receives inputs from its pre-synaptic partners is thus of utmost importance to the computations it is performing.

4) At this point, a reconsideration of the underlying implementation of a motion detector by T4 neurons is necessary. Both supralinearities as well as sublinearities have been measured in T4 (Haag et al., 2016, 2017). The connectivity between Mi9, Mi1, Tm3, and T4 neurons hints to the implementation of a Hassenstein–Reichardt detector. However, the connectivity between Mi4, C3, Mi1, Tm3, and T4 neurons hints to the implementation of a Barlow-Levick detector. A so-called three-arm model containing both the Hassenstein–Reichardt supralinearity and the Barlow–Levick sublinearity (named HRBL detector) can be conceived (Arenz et al., 2017; Haag et al., 2016) (Fig. 14c). The importance of TmY15 neurons to the computation performed by T4 neurons is limited by the fact that they spread multiple columns (Shinomiya et al., 2019). Because of this lack of spatial acuity, they are not expected to play a major role in the computation of direction selectivity.

Implementation of biological multiplication by T4 neurons

Calcium imaging studies of the presynaptic partners to T4 have revealed some of their response kinetics (Arenz et al., 2017). Mi9 has an OFF center. It has thus a different polarity than the other inputs to T4 neurons which have ON centers and which increase their activity in response to ON visual stimuli (Arenz et al., 2017; Richter et al., 2018). The succession of an OFF inhibitory input followed by an ON excitatory input would indeed be the optimal application of the AND-NOT logical operator described in 1.3.3. The multiplication of coincidental inputs is predicted by the Hassenstein-Reichardt detector. In **manuscript 1**, we investigate the biophysical implementation of multiplicative arithmetic by T4 neurons and by its inputs.

Implementation of differential filtering of the inputs to T4 neurons

Various correlator models predict the necessity for the differential filtering of the input signals to nonlinear operators. This need for filtering is a natural consequence of the physical delays established by spatially separated sensors (Jeffress, 1948). Thereafter, the inputs to T4 should show signs of differential filtering. Some evidence to that effect can be found in previous calcium imaging studies (Arenz et al., 2017). The temporal kernels – resulting from the reverse-correlation of a noisy stimulus – of Mi4 and Mi9 neurons show low-pass filter properties while temporal kernels of Tm3 and Mi1 neurons show band-pass filter properties (Arenz et al., 2017). However, knowledge about the origin of this differential filtering is scant. In **manuscript 2**, we investigate the biological strategies leading to the emergence of the differential filtering of the inputs to T4 neurons.

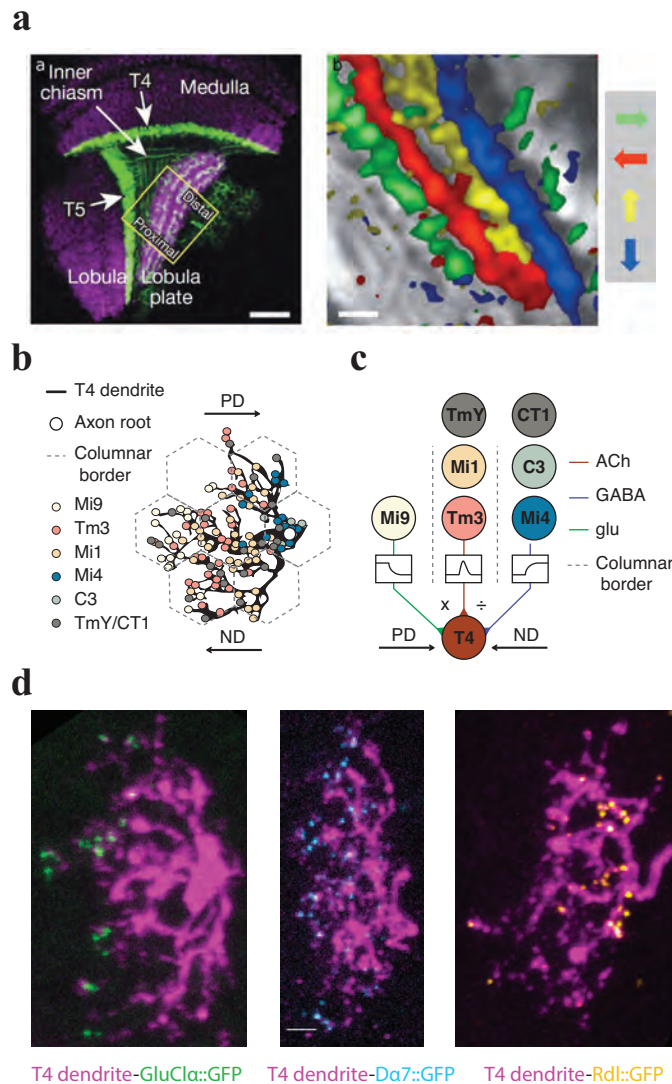


Fig. 14. Direction-selective T4 neurons

(a) The dendrites of ON direction-selective T4 neurons are found in the medulla while the dendrites of OFF direction-selective T5 neurons are situated in the lobula (left). T4 and T5 neurons are separated in four sub-types each selective for light increments in one of the cardinal directions (right). Images taken with permission from Maisak *et al.*, 2013. (b) From electron microscopy studies, the position of input synapses onto the dendrites of a T4 are known. Each color represents an input from Mi9, Tm3, Mi1, Mi4, C3, CT1, and TmY15 (TmY) neurons. (c) A three-arm model combining the Hassenstein–Reichardt and the Barlow–Levick half-detectors. Here Mi9, Mi4, and C3 inputs act as slow low-pass filtering lines while Tm3 and Mi1 act as the fast-central input line. The AND-NOT facilitation operator happening between the left and the central arms is represented by a multiplication. The AND-NOT veto happening between the right and the central arms is represented as a division. (d) Mi9 glutamatergic inputs at the tips of T4 dendrites are made onto GluCl α receptors (left). Mi1 and Tm3 cholinergic inputs to T4 dendrites are made onto D α 7 receptors (middle). Mi4 and C3 GABAergic inputs to T4 dendrites are made onto Rdl receptors (right). Images taken with permission from Fendl *et al.*, 2020.

1.7 Concluding words

Motion vision has been the subject of intense research for the best part of the last seventy years. From differential filtering to nonlinear multiplication, the motion vision circuit in *Drosophila* contains most of the operations intrinsic to computational theories of the brain and has the advantage of being tightly packed in a relatively small and stereotypical neuronal circuit. As I started my doctoral work, the electron microscopic mapping of *Drosophila*'s direction-selective circuit had already been exhaustively accomplished (Takemura et al., 2013, 2017). Functional imaging studies had uncovered the direction-selective properties of T4 neurons (Haag et al., 2017; Maisak et al., 2013) as well as the differential temporal filtering of its inputs (Arenz et al., 2017). Multiple correlation-type models of direction selectivity from the Hassenstein–Reichardt detector (Hassenstein and Reichardt, 1956) to the F-H model (Poggio and Reichardt, 1976) ending with the three arms detector (Arenz et al., 2017) had been proposed. It seemed clear that the inputs from Mi9, Tm3, and Mi1 cells onto T4 neurons had to be the components of a supralinear multiplicative operation. On the other hand, the inputs from Mi4, C3, Mi1, and Tm3 cells onto T4 neurons had to be components of a sublinear divisive (or subtractive) operation. Furthermore, it had to be the temporal filtering properties of the inputs to T4 which allowed for the coincidental detection of light signals and thus for the possibility of operational nonlinearities. In this constellation, my first project was to artificially reconstruct the multiplicative stage of the Hassenstein–Reichardt detector via the use of GCaMP, optogenetic tools, and of pharmacological tools. Although the use of GCaMP had made the recent scientific advancements possible, it quickly became clear that the limitations of this tool rendered the functional knowledge about T4 neurons and about its columnar inputs too unprecise for a reconstitution task. What was needed was an intimate knowledge of the electrical properties of T4 neurons and of its inputs at a high temporal resolution. This could only be achieved via whole-cell patch clamp recordings *in vivo*. This technique would grant access to the biophysical relevance of targeted ion channel types as well as access to the signature current composition of each cell type. Finally, with whole-cell patch clamp recordings, the data missing in order to build a conductance-based model where each cell's activity is measured would be within the reach of a few borosilicate glass capillaries. In this context, the main focus of my thesis became the investigation of the cellular and biophysical substrates of 1) the nonlinear, multiplication-like operation happening at the level of the dendrites of the primary motion sensing T4 neurons and 2) the biological strategies leading to the differential filtering of the presynaptic partners of T4 neurons.

In **manuscript 1**, my co-authors and I describe how the multiplication stage of a Hassenstein–Reichardt detector is biophysically implemented at the dendrite of T4 neurons. In **manuscript 2**, we further describe how the differential filtering of the inputs to T4 neurons emerges from the connectivity of the direction-selective network in the ON pathway.

MANUSCRIPTS

2.1 Manuscript 1: A biophysical account of multiplication by a single neuron

Abstract

Nonlinear, multiplication-like operations carried out by individual nerve cells greatly enhance the computational power of a neural system, but our understanding of their biophysical implementation is scant. Here we pursue this problem in the *Drosophila melanogaster* ON motion vision circuit, in which we record the membrane potentials of direction-selective T4 neurons and of their columnar input elements in response to visual and pharmacological stimuli in vivo. Our electrophysiological measurements and conductance-based simulations provide evidence for a passive supralinear interaction between two distinct types of synapse on T4 dendrites. We show that this multiplication-like nonlinearity arises from the coincidence of cholinergic excitation and release from glutamatergic inhibition. The latter depends on the expression of the glutamate-gated chloride channel GluCl α in T4 neurons, which sharpens the directional tuning of the cells and shapes the optomotor behaviour of the animals. Interacting pairs of shunting inhibitory and excitatory synapses have long been postulated as an analogue approximation of a multiplication, which is integral to theories of motion detection, sound localization and sensorimotor control.

Authors

Lukas N. Groschner^{1,2}, **Jonatan G. Malis**^{1,2,3}, Birte Zuidinga² & Alexander Borst²

¹These authors contributed equally: **Jonatan G. Malis**, Lukas N. Groschner.

² Max Planck Institute of Neurobiology, Martinsried, Germany.

³ Graduate School of Systemic Neurosciences, LMU Munich, Martinsried, Germany.

This article will be published in *Nature* in March 2022 (Groschner, Malis et al., 2022).

Contributions

L.N.G., **J.G.M.**, and A.B. conceived the study, designed experiments, and ran model simulations. L.N.G. and **J.G.M.** performed and analysed electrophysiological recordings. L.N.G., **J.G.M.**, and B.Z. performed histological analyses and B.Z. conducted and analysed behavioural experiments. The manuscript was written by L.N.G and edited by all authors, chiefly by B.Z.

A biophysical account of multiplication by a single neuron

<https://doi.org/10.1038/s41586-022-04428-3>

Lukas N. Groschner^{1,2}✉, Jonatan G. Malis^{1,2}, Birte Zuidinga¹ & Alexander Borst¹✉

Received: 21 June 2021

Accepted: 14 January 2022

Open access

 Check for updates

Nonlinear, multiplication-like operations carried out by individual nerve cells greatly enhance the computational power of a neural system^{1–3}, but our understanding of their biophysical implementation is scant. Here we pursue this problem in the *Drosophila melanogaster* ON motion vision circuit^{4,5}, in which we record the membrane potentials of direction-selective T4 neurons and of their columnar input elements^{6,7} in response to visual and pharmacological stimuli in vivo. Our electrophysiological measurements and conductance-based simulations provide evidence for a passive supralinear interaction between two distinct types of synapse on T4 dendrites. We show that this multiplication-like nonlinearity arises from the coincidence of cholinergic excitation and release from glutamatergic inhibition. The latter depends on the expression of the glutamate-gated chloride channel GluCl α ^{8,9} in T4 neurons, which sharpens the directional tuning of the cells and shapes the optomotor behaviour of the animals. Interacting pairs of shunting inhibitory and excitatory synapses have long been postulated as an analogue approximation of a multiplication, which is integral to theories of motion detection^{10,11}, sound localization¹² and sensorimotor control¹³.

Motion vision in insects represents a textbook example¹⁴ of nonlinear signal processing by a single neuron. Each photoreceptor of the compound eye captures changes in light intensity, but it is blind to the direction of motion. To compute visual motion, the signals of at least two neighbouring photoreceptors must be processed nonlinearly by a downstream local motion detector (Fig. 1a). In the Hassenstein–Reichardt model¹⁰, multiplication ensures detector output only if the two signals coincide. The coincidence results from asymmetric temporal filtering of the input signals and the sequence of photoreceptor activation, one after the other, as it unfolds during visual motion in the detector's preferred direction (PD). The Barlow–Levick model of motion vision, which was first proposed for the rabbit retina¹⁵, uses a divisive nonlinearity to cancel responses to motion in the detector's null direction (ND).

The visual system of *Drosophila* is compatible with both models (Fig. 1a). T4 neurons, which are functionally equivalent to the nonlinear stages of both models, respond selectively to luminance increments moving in one out of four cardinal directions⁵. Their direction selectivity arises in the second optic neuropil^{5,16,17}, where spatial information is preserved in a retinotopic columnar organization¹⁸. Each T4 dendrite innervates approximately seven columns—at least three in a row along the neuron's PD⁶ (Fig. 1b)—and, therefore, samples from multiple adjacent points in visual space. Recent studies^{6,7} identified most—if not all—columnar medulla intrinsic (Mi), transmedullary (Tm) and centrifugal (C) neurons that form synapses at distinct locations along a T4 neuron's dendrite: glutamatergic Mi9 neurons at the distal branches (where stimuli moving in the T4 cell's PD first affect its membrane potential), cholinergic Tm3 and Mi1 neurons at the centre, and GABAergic Mi4 and C3 neurons at the proximal segment (Fig. 1b).

The emerging three-legged circuit motif involves a divisive interaction between cholinergic and GABAergic synapses and a multiplicative interaction between glutamatergic and cholinergic synapses^{17,19–22} (Fig. 1a, b). However, crucial assumptions concerning the multiplicative term of this model²¹ remain untested: (1) the multiplication-like synaptic interaction involves disinhibition; (2) the supralinearity arises from the T4 cells' passive membrane properties; and (3) it sharpens the directional tuning of the neurons and the optomotor acuity of the animal.

The first assumption, that multiplication requires release from inhibition, hinges on the conditions that the signals carried by glutamatergic Mi9 neurons are of opposite polarity to those of the other input elements and that glutamate controls the input resistance of T4 neurons through shunting inhibition²³. Direct measurements of input resistance and membrane voltage are possible only through patch-clamp experiments, which we conducted in vivo in tethered flies, guided by cell-type-specific expression of green fluorescent protein (GFP; Extended Data Fig. 1a). We recorded the membrane potentials of T4 cells and of their presynaptic partners while projecting a 60 Hz spatiotemporal binary white-noise stimulus with a pixel size of 2.8° onto the fly's eye. To characterize the receptive fields of the neurons, we cross-correlated the luminance of each pixel with the recorded voltage (Fig. 1c–e and Extended Data Fig. 1b). We found that the membrane potentials of Tm3, Mi1, Mi4 and C3 neurons were positively correlated with luminance, whereas those of Mi9 neurons were anticorrelated (Fig. 1d). The negative correlation was due to a rapid hyperpolarization following increments in luminance, as opposed to a possible depolarization in response to luminance decrements (Extended Data Fig. 2). Thus, the Mi9 neuron maintains a degree of continuous activity in darkness that ceases abruptly when the centre of its receptive field

¹Max Planck Institute of Neurobiology, Martinsried, Germany. ²These authors contributed equally: Lukas N. Groschner, Jonatan G. Malis. ✉e-mail: groschner@neuro.mpg.de; borst@neuro.mpg.de

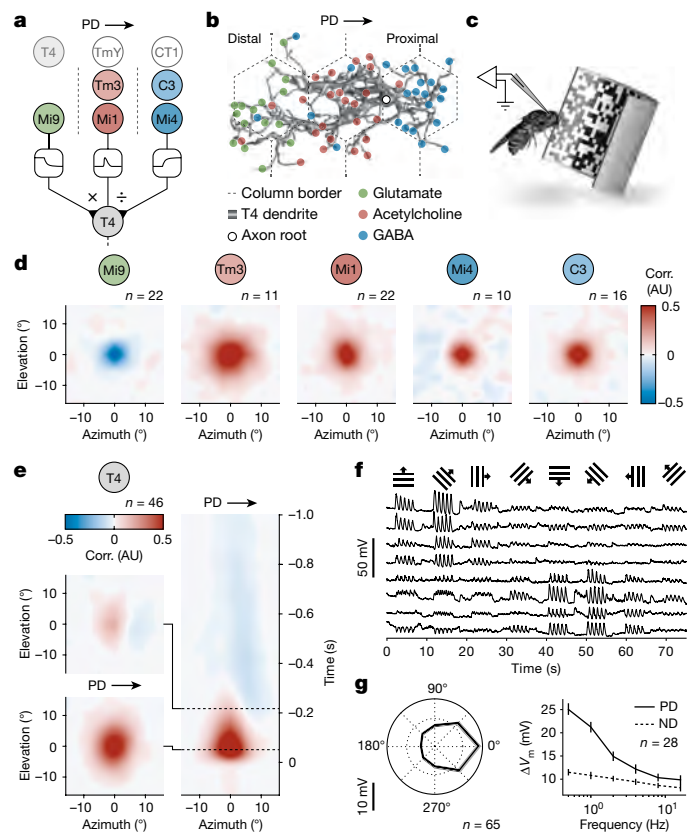


Fig. 1 | Receptive fields of direction-selective T4 neurons and their presynaptic partners. **a**, The circuit architecture for visual ON motion detection involving a multiplicative interaction (×) between synapses of glutamatergic Mi9 and synapses of cholinergic Mi1/Tm3 neurons and a divisive interaction (÷) between synapses of Mi1/Tm3 and synapses of GABAergic C3/Mi4 neurons. Non-columnar inputs from T4, TmY15 and CT1 neurons are shaded. The dashed lines show the column borders. **b**, A T4 dendrite with subcellular segregation of glutamatergic (green), cholinergic (red) and GABAergic synapses (blue). Data from ref. ⁷. **c**, Targeted patch-clamp recording in vivo during visual stimulation. **d**, Average spatial receptive fields of input neuron classes obtained by reverse correlation (corr.) of membrane potentials and white-noise stimuli. AU, arbitrary units. **e**, The average spatial receptive fields of T4 neurons (left) representing cross-sections of the spatiotemporal receptive field (right) at two time points (dashed lines). **f**, Exemplary membrane potential recordings of T4 neurons in response to visual stimulation with square-wave gratings moving in the directions indicated on top. **g**, Directional (left) and frequency tuning (right) of T4 neurons based on the change in membrane potential (ΔV_m) in response to visual stimulation with square-wave gratings. Data are mean \pm s.e.m. *n* values indicate the number of cells.

is stimulated by light. Yet, while the delayed inhibition mediated by GABAergic inputs²⁴ was clearly discernible in the spatiotemporal receptive fields of direction-selective T4 neurons (Fig. 1e–g), the contribution of Mi9 neurons was not immediately apparent.

To test the effect of glutamate—and, indirectly, that of Mi9—on T4 neurons, we applied the neurotransmitter directly to T4 dendrites (Fig. 2a). Pneumatic ejection of glutamate transiently hyperpolarized T4 cells by 3.72 ± 0.61 mV (mean \pm s.e.m.; Fig. 2b, c). The mild hyperpolarization was paralleled by a 25.27% decrease in input resistance, which was fully reversible. Repeated applications of glutamate enabled us to toggle T4 cells between states of high and low resistance (Fig. 2d, e). Targeted RNA interference (RNAi) with transcripts of *GluCl α* ⁸, the most highly expressed glutamate receptor gene in T4 neurons^{25–28}, blocked glutamate-gated whole-cell currents (Fig. 2f) and abolished the effects of glutamate on membrane potential and input resistance (Fig. 2b, c, e), while leaving the morphology of T4 cells intact (Extended Data Fig. 3).

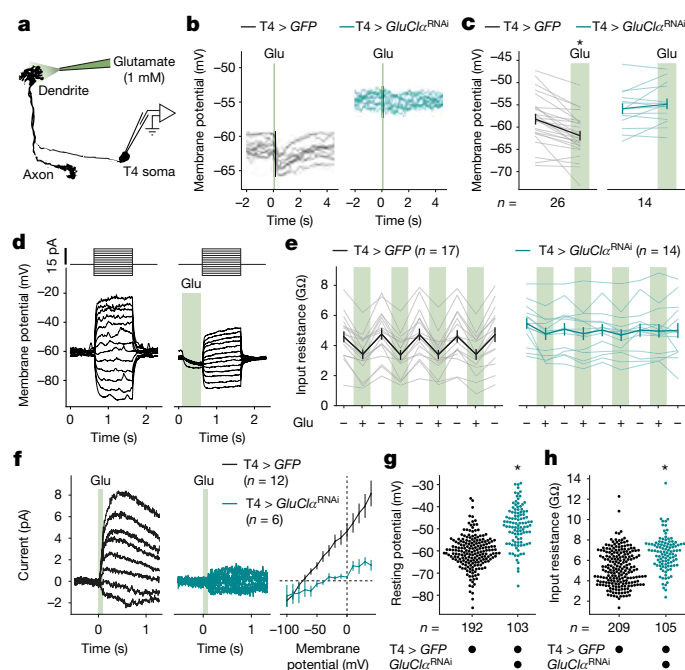


Fig. 2 | Glutamate controls T4 neuron excitability through *GluCl α* . **a**, Glutamate application during whole-cell recording. **b**, Membrane potential traces of exemplary T4 neurons in response to 100 ms glutamate pulses (Glu) in flies expressing *GFP* (black; T4 > *GFP*, full genotypes are provided in the Methods) or *GFP* + *GluCl α* ^{RNAi} (teal; T4 > *GluCl α* ^{RNAi}) under T4-cell-specific GAL4 control. Ten technical replicates per genotype are shown. **c**, The average membrane potentials of T4 neurons expressing *GFP* (black) or *GFP* + *GluCl α* ^{RNAi} (teal) before and after glutamate application (green). A significant effect of glutamate, determined using a two-tailed paired Student’s *t*-test, is indicated; $*P = 2.1 \times 10^{-6}$. The light lines represent individual cells. The dark lines represent the mean \pm s.e.m. **d**, Voltage responses of one exemplary T4 neuron to current steps (top) without (left) and with (right) prior glutamate application. **e**, Input resistances of T4 neurons expressing *GFP* (black) or *GFP* + *GluCl α* ^{RNAi} (teal) during (+) and in between (–) repeated glutamate applications. The light lines represent individual cells. The dark lines represent the mean \pm s.e.m. Two-way repeated-measures analysis of variance (ANOVA) detected a significant effect of glutamate ($P = 3.5 \times 10^{-12}$) and a significant glutamate \times genotype interaction ($P = 1.6 \times 10^{-11}$). **f**, Average whole-cell currents in response to 100 ms glutamate pulses at different voltages (left and middle) and current–voltage relationships (right) of T4 neurons expressing *GFP* (black) or *GFP* + *GluCl α* ^{RNAi} (teal). Data are mean \pm s.e.m. **g**, **h**, Resting membrane potentials (**g**) and input resistances (**h**) of T4 neurons expressing *GFP* (black) or *GFP* + *GluCl α* ^{RNAi} (teal) measured under dark conditions. Significant differences between genotypes, determined using two-tailed Mann–Whitney *U*-tests, are indicated; $*P = 3.4 \times 10^{-23}$ (**g**), $*P = 4.8 \times 10^{-11}$ (**h**). *n* values indicate the number of cells.

Importantly, post-transcriptional silencing of *GluCl α* caused an average 11.94 mV depolarization of the resting membrane potential (Fig. 2g) and an increase in input resistance from 5.28 ± 0.12 to 6.70 ± 0.16 G Ω (mean \pm s.e.m.; Fig. 2h), measured under dark conditions. This speaks for a persistent release of glutamate in the dark that keeps *GluCl α* channels open and clamps the membrane potential of T4 neurons close to the equilibrium potential of chloride—a *GluCl α* -mediated short circuit that curtails any excitation, unless glutamatergic Mi9 neurons are switched off first.

To break down the precise temporal sequences of synaptic signals evoked by visual stimulation, we obtained membrane potential recordings while moving contrast edges through the T4 neuron’s receptive field in its PD and ND (Fig. 3). Bright ON and dark OFF edges travelling at a velocity of 30° s^{-1} revealed distinct, fingerprint-like signatures of electrical activity. To explain these signatures in terms of their underlying synaptic conductances, we subjected the five columnar input

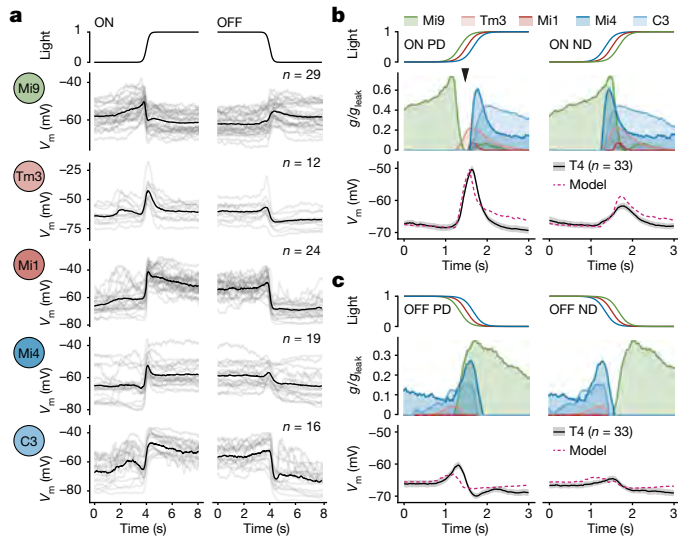


Fig. 3 | Conductance-based T4 neuron model. **a**, Aligned membrane voltage (V_m) responses of columnar T4 input neurons to ON and OFF edges moving at 30° s^{-1} . Time course of normalized light intensity at the receptive field centre is shown at the top. The light lines represent individual cells. The dark lines represent the mean. **b, c**, Conductance-based biophysical simulations of the membrane potential (V_m) of a T4 neuron in response to ON (**b**) and OFF (**c**) edge motion. Input signals were time-shifted, as evident from light intensities at receptive field centres (top), to simulate visual motion in the T4 neuron's PD and ND, respectively. The voltage signals of presynaptic neurons were converted into normalized postsynaptic conductances (g/g_{leak} , centre) using a threshold and gain obtained by fitting the model (dashed pink) to measured T4 voltage responses (solid black, bottom). Conductance values are mean and area under curves. Voltage values are mean \pm s.e.m. The arrowhead in **b** marks the window of opportunity when a minimum of shunting inhibition (green/blue) coincides with excitation (red). n values indicate the number of cells.

elements of T4 cells to an identical set of stimuli (Fig. 3a). Our reconstructions of the receptive fields of the cells (Extended Data Fig. 1b) enabled a post hoc alignment of their responses, which we used to recreate the direction-dependent input sequences that are expected to shape the voltage responses of a T4 cell (Fig. 3b, c). With all input signals and the respective reversal potentials at hand (Extended Data Fig. 4a–d), we simulated the electrical equivalent circuit of a passive single-compartment T4 neuron (Fig. 3b, c and Extended Data Fig. 5a). Measured membrane voltages of presynaptic neurons were transformed into postsynaptic conductance values using two free parameters per neuron: a gain (that is, synaptic weight) and a threshold below which no transmission occurred. The T4 neurons' electrically compact morphology (Extended Data Fig. 4e, f) led us to neglect the membrane capacitance. After estimating the model parameters on the basis of a least-squares fit to the average voltage responses of T4 neurons, we quantified parameter uncertainty using an artificial neural network²⁹. Examination of the full range of parameter combinations compatible with our measurements confirmed the estimated values, which fell within regions of high conditional probability (Extended Data Fig. 6). In agreement with our second assumption, the voltage responses of T4 neurons to all four stimuli were captured by our passive conductance-based model (Fig. 3b, c), which naturally joins an excitatory and an inhibitory signal in a supralinear manner. While, in a passive membrane, two excitatory inputs are bound to combine sublinearly (Extended Data Fig. 5b), the coincidence of an excitatory input with the release from an inhibitory one will almost invariably yield a supralinear response^{1,21} (Extended Data Fig. 5c). Exceptions are rare and can occur only under conditions in which the reversal potential of the excitatory current is closer to the leak reversal potential than that of the inhibitory current (Extended Data Fig. 5d, e and Supplementary Equations).

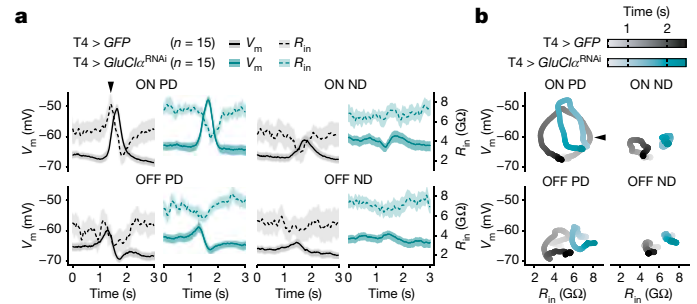


Fig. 4 | A *GluCl α* -dependent input resistance peak. **a**, Simultaneously measured membrane potentials (V_m , solid lines) and input resistances (R_{in} , dashed lines) of T4 neurons expressing *GFP* (black) or *GFP + GluCl α ^{RNAi}* (teal) in response to ON (top) and OFF (bottom) edges moving at 30° s^{-1} in the neurons' PD and ND. Data are mean \pm s.e.m. n values indicate the number of cells. **b**, The average membrane potential (V_m) as a function of input resistance (R_{in}) of T4 neurons shown in **a** in response to ON (top) and OFF (bottom) edges moving in the PD (left) and ND (right). The arrowheads mark the input resistance peak.

For ON edge motion in the PD, a brief interval of minimal inhibitory conductance—a window of opportunity³⁰—opened up (Fig. 3b). The transient lack of inhibition led to the amplification of excitatory inputs from Mi1 and Tm3 neurons during the upstroke of the T4 cell's voltage trajectory (Fig. 3b and Extended Data Fig. 7). Intuitively, this can be explained by the coincident drop in overall conductance or, in other words, the increase in input resistance.

Direct evidence for the predicted increase in resistance (Extended Data Fig. 8) was obtained using current-clamp experiments. We took advantage of each T4 neuron's stereotyped responses to moving edges and presented the fly with repeated episodes of identical visual stimulation. Varying the holding current in between episodes enabled us to obtain time-locked measurements of membrane potential and resistance (Fig. 4 and Extended Data Fig. 9). For ON edges moving in the neuron's PD, the input resistance revealed a distinct peak that preceded the depolarizing voltage excursion and amounted to approximately 147% of the initial resistance (Fig. 4). Under all other conditions, the T4 cell experienced, if anything, a dip in excitability (Fig. 4). RNAi-mediated silencing of *GluCl α* pre-empted the increase in that the resistance of *GluCl α* -deficient T4 neurons at the baseline was already equivalent to the peak values reached by wild-type neurons (Fig. 4). Owing to the shift in resting potential towards the reversal potential of acetylcholine-induced currents, depletion of *GluCl α* also reduced the membrane potential response amplitude from 18.10 ± 0.77 mV in wild-type T4 neurons to 13.63 ± 1.05 mV in *GluCl α ^{RNAi}*-expressing T4 neurons (mean \pm s.e.m.; $n = 53$ and $n = 30$ cells, respectively; $P = 0.0008$, two-tailed Mann–Whitney U -test).

The ability to restrict the arithmetic repertoire of T4 neurons by interfering with the abundance of *GluCl α* enabled us to test the prediction that multiplication sharpens directional tuning. We moved bright edges at a speed of 30° s^{-1} in 36 evenly spaced directions while recording the membrane potentials of GFP-labelled wild-type and *GluCl α ^{RNAi}*-expressing T4 neurons (Fig. 5a–c). RNAi targeting transcripts of *Nmdar1*, which encodes a glutamate-gated cation channel with negligible expression in T4 cells^{25–28}, was used as an additional control. Silencing *GluCl α* in T4 cells in vivo replicated the effect of silencing Mi9 neurons in silico—it broadened the directional tuning curve (Fig. 5a). Response amplitudes of wild-type and *Nmdar1^{RNAi}*-expressing neurons declined steeply with increasing angular distance from PD, to 72.97% and 72.74% at a deviation of 60° , respectively. The decline was much shallower in *GluCl α ^{RNAi}*-expressing T4 neurons of which the response amplitudes at PD $\pm 60^\circ$ still averaged 89.62% of the corresponding PD responses (Fig. 5a). Rather than enhancing voltage responses to

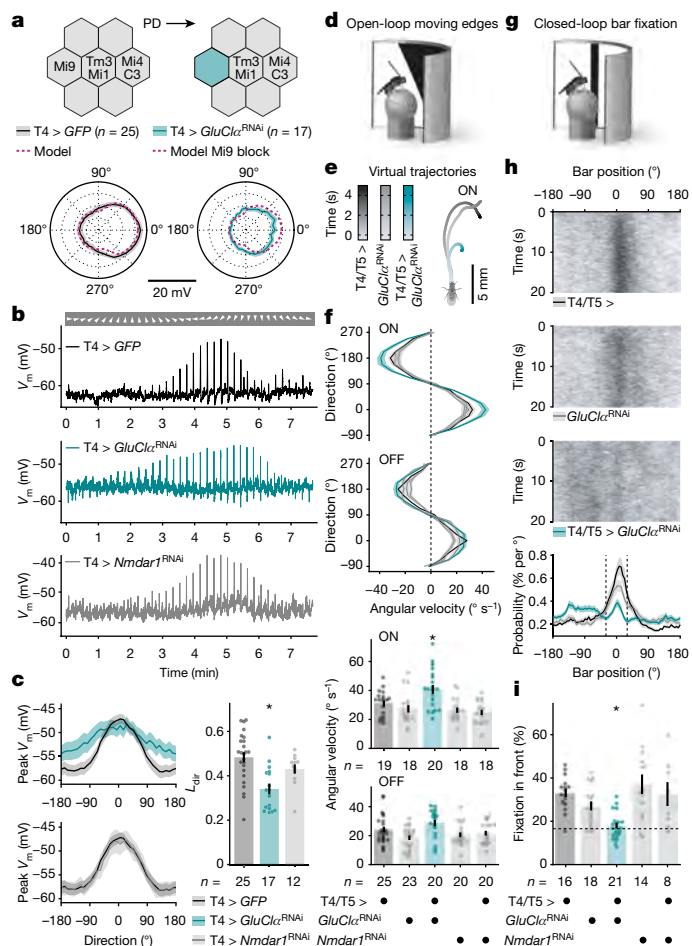


Fig. 5 | *GluCl α* sharpens directional tuning of T4 neurons and optomotor behaviour. **a**, T4 input organization in the presence (top left) and absence of Mi9 neurons (top right). Bottom, directional tuning of T4 neurons expressing *GFP* (black) or *GFP + GluCl α ^{RNAi}* (teal) on the basis of membrane potential responses to ON edges moving at 30° s⁻¹. Data are mean \pm s.e.m. *n* values indicate the number of cells. The pink dashed lines show model predictions. **b**, Exemplary membrane voltage (*V_m*) recordings from T4 neurons in **c** in response to ON edges moving in the indicated directions (arrowheads). **c**, Peak membrane voltages of T4 neurons expressing *GFP* (black), *GFP + GluCl α ^{RNAi}* (T4 > *GluCl α ^{RNAi}*, teal) or *GFP + Nmdar1^{RNAi}* (T4 > *Nmdar1^{RNAi}*, grey) as a function of the direction of ON edge motion (left). Data are mean \pm s.e.m. Right, directional tuning (*L_{dir}*) for all genotypes. Welch's ANOVA test followed by Dunn's multiple-comparisons test detected a significant difference of T4 > *GluCl α ^{RNAi}* from T4 > *GFP*; **P* = 0.0002. The circles show individual cells. The bars show the mean \pm s.e.m. *n* values indicate the number of cells. **d**, Open-loop optomotor behaviour. **e**, Average virtual walking trajectories of flies expressing *GluCl α ^{RNAi}* in T4/T5 cells (teal, *n* = 20) and of their parental controls (back and grey, *n* = 19 and *n* = 18, respectively) in response to ON edge motion at a 22.5° angle. **f**, The angular velocities of flies expressing *GluCl α ^{RNAi}* (teal) or *Nmdar1^{RNAi}* (grey) in T4/T5 neurons, and of their parental controls (black/grey), as a function of stimulus direction and polarity (top). Data are mean \pm s.e.m. Bottom, absolute angular velocities scaled by horizontal stimulus components. For moving ON edges, one-way ANOVA followed by Holm–Šidák's multiple comparisons test detected a significant difference of flies expressing *GluCl α ^{RNAi}* in T4/T5 cells from both parental controls; **P* = 0.0105. The circles represent individual flies. The bars show the mean \pm s.e.m. *n* values indicate the number of flies. **g**, Closed-loop bar fixation behaviour. **h**, Exemplary bar trajectories (832 trials and 16 flies per genotype, top) and the overall bar position probabilities (bottom) for flies expressing *GluCl α ^{RNAi}* in T4/T5 cells (teal) and their parental controls (back/grey). Probabilities are mean \pm s.e.m. of flies in **i**. **i**, The percentage of the time that the bar occupied a 60° central window (fixation in front, dashed lines in **h**). Welch's ANOVA followed by Dunnett's T3 multiple comparisons test detected a significant difference of flies expressing *GluCl α ^{RNAi}* in T4/T5 cells from both parental controls; **P* = 0.0042. The dashed line indicates the chance level. The circles represent individual flies. The bars show mean \pm s.e.m. *n* values indicate the number of flies.

visual motion in the PD, the presence of *GluCl α* attenuated responses to motion in all other directions, an effect that was especially obvious at those directions not affected by inhibition from Mi4 and C3 neurons (Fig. 5a–c). This was reflected in a significant reduction of the T4 neurons' directional tuning indices (*L_{dir}*) in the absence of *GluCl α* compared with the wild-type controls (*P* = 0.0002, Kruskal–Wallis test followed by Dunn's multiple-comparisons test; Fig. 5c).

The impact of this intervention on the flies' optomotor responses offered an opportunity to link a molecular mechanism to behavioural performance. Walking on a spherical treadmill (Fig. 5d), flies expressing *GluCl α ^{RNAi}* in T4 neurons and their OFF-responsive T5 twins under control of *R39H12-GAL4* (Extended Data Fig. 10a) overestimated the velocity of bright, but not of dark, edges moving in different directions. In their attempt to compensate for the perceived egomotion, animals that carried both the *GAL4* and the *UAS-GluCl α ^{RNAi}* transgene rotated the treadmill excessively about the vertical axis and strayed off the virtual paths of their parental controls (Fig. 5e, f). The angular velocities of animals of all other genotypes, including those expressing *Nmdar1^{RNAi}* in T4/T5 neurons, were indistinguishable (Fig. 5f). In contrast to ON-responsive T4 neurons, which are speckled with *GluCl α* receptors at both dendritic and axonal compartments, T5 neurons feature the receptor exclusively at their axon terminals³¹. It follows that the impairment of optomotor acuity specific to moving ON edges can, in all likelihood, be attributed to a process that is localized to the dendrites of T4 neurons.

To test the ability of animals with a T4/T5-cell-restricted *GluCl α* deficiency to hold a steady course under closed-loop conditions, we took advantage of the flies' tendency to approach a dark vertical bar, a behaviour that depends on T4/T5 neurons^{32,33}. When given the opportunity to control the bar position through their walking behaviour (Fig. 5g), control animals had a clear preference for holding the bar in front of them at 0 \pm 30°. By contrast, flies expressing *GluCl α ^{RNAi}* in T4/T5 neurons failed to maintain a stable bearing relative to the bar (Fig. 5h) despite moving at a comparable pace (Extended Data Fig. 10b). We corroborated this discovery using another, more specific split *GAL4* line (Extended Data Fig. 10c–e). Independent of the driver line used, animals with a T4/T5-cell-restricted *GluCl α* -deficiency performed at chance level (Fig. 5i and Extended Data Fig. 10f). In accordance with our third assumption, locking T4 neurons in a state of high gain (Figs. 2h and 4) resulted in exaggerated optomotor responses (Fig. 5d–f) and impaired performance as the animals navigated a virtual environment (Fig. 5g–i). These observations reveal the behavioural significance of a multiplication-like operation in a specific type of neuron.

Discussion

Nervous systems rely on nonlinearities to process information¹. A multiplication-like operation—possibly the simplest form of non-linearity—is implicated in the transformation of eye-centric into head-centric coordinates¹³, the localization of sound¹², the combination of multisensory signals^{34,35} and the detection of visual motion¹⁰. The biophysical underpinnings of such an operation in a single neuron are by and large unclear. One exception is the looming detector of locusts, in which—just like on a slide rule—the sum of two logarithmically scaled signals is exponentially transformed into spike rates³⁶. Other multiplicative synaptic interactions involve NMDA receptors^{37,38}. Both mechanisms are contingent on threshold-like nonlinearities in the current–voltage relationships of ion channels: the gating of tetrodotoxin-sensitive sodium channels in the former and the magnesium block of NMDA receptors in the latter case. Here, we describe a multiplication-like nonlinearity that is independent of thresholds.

Using the visual circuit of the fruit fly as an example⁵, we took advantage of the neurons' compact sizes, their known connectivity⁶ and our ability to manipulate them genetically to study the biophysical basis of the multiplication step in a Hassenstein–Reichardt detector¹⁰.

We recorded the membrane potentials of ON motion-sensitive T4 neurons and of their columnar input elements in response to a defined set of visual stimuli. Our measurements of both pre- and postsynaptic voltages obviated the need for assumptions regarding the temporal dynamics of input signals when modelling the detector's output. The voltage responses of T4 neurons were reproduced rather faithfully by our passive conductance-based model (Figs. 3b, c and 5a). Discrepancies between simulation and reality could be due to selective synaptic delays or the 15% of dendritic inputs from wide-field TmY15 and CT1 neurons^{6,7,39}, which were not taken into account. In the model, as in our data, the supralinearity arises from the coincidence of excitation and release from shunting inhibition²³. Such 'multiplicative disinhibition' constitutes the inverse operation of divisive inhibition. It is free from the voltage dependence that often limits threshold-based systems⁴⁰ and less sensitive to changing signal amplitudes²¹ (Extended Data Fig. 5c). More broadly, theory invokes multiplication as a strategy to gate information flow^{41,42}. The passive biophysical mechanism that we propose could lend itself to other systems, such as the logical conjunction of chemosensory signals⁴³ or the gating of cortical afferents⁴⁴. Motion vision in flies may provide one of many cases of multiplicative disinhibition.

Online content

Any methods, additional references, Nature Research reporting summaries, source data, extended data, supplementary information, acknowledgements, peer review information; details of author contributions and competing interests; and statements of data and code availability are available at <https://doi.org/10.1038/s41586-022-04428-3>.

- Koch, C. & Poggio, T. Multiplying with Synapses and Neurons. In *Single Neuron Computation* (eds Mckenna T. et al.) 315–345 (Academic Press, 1992).
- Koch, C. & Segev, I. The role of single neurons in information processing. *Nat. Neurosci.* **3**, 1171–1177 (2000).
- London, M. & Häusser, M. Dendritic computation. *Annu. Rev. Neurosci.* **28**, 503–532 (2005).
- Joesch, M., Schnell, B., Raghu, S. V., Reiff, D. F. & Borst, A. ON and OFF pathways in *Drosophila* motion vision. *Nature* **468**, 300–304 (2010).
- Maisak, M. S. et al. A directional tuning map of *Drosophila* elementary motion detectors. *Nature* **500**, 212–216 (2013).
- Takemura, S.-Y. et al. The comprehensive connectome of a neural substrate for 'ON' motion detection in *Drosophila*. *eLife* **6**, e24394 (2017).
- Shinomiya, K. et al. Comparisons between the ON- and OFF-edge motion pathways in the *Drosophila* brain. *eLife* **8**, e40025 (2019).
- Cully, D. F., Pareiss, P. S., Liu, K. K., Schaeffer, J. M. & Arena, J. P. Identification of a *Drosophila melanogaster* glutamate-gated chloride channel sensitive to the antiparasitic agent avermectin. *J. Biol. Chem.* **271**, 20187–20191 (1996).
- Liu, W. W. & Wilson, R. I. Glutamate is an inhibitory neurotransmitter in the *Drosophila* olfactory system. *Proc. Natl Acad. Sci. USA* **110**, 10294–10299 (2013).
- Hassenstein, B. & Reichardt, W. Systemtheoretische Analyse der Zeit-, Reihenfolgen- und Vorzeichenauswertung bei der Bewegungsperzeption des Rüsselkäfers *Chlorophanus*. *Z. Naturforsch. B* **11**, 513–524 (1956).
- Borst, A., Haag, J. & Reiff, D. F. Fly motion vision. *Annu. Rev. Neurosci.* **33**, 49–70 (2010).
- Peña, J. L. & Konishi, M. Auditory spatial receptive fields created by multiplication. *Science* **292**, 249–252 (2001).
- Andersen, R. A., Essick, G. K. & Siegel, R. M. Encoding of spatial location by posterior parietal neurons. *Science* **230**, 456–458 (1985).
- Luo, L. *Principles of Neurobiology* (Garland Science, 2020).
- Barlow, H. B. & Levick, W. R. The mechanism of directionally selective units in rabbit's retina. *J. Physiol.* **178**, 477–504 (1965).
- Fisher, Y. E., Silies, M. & Clandinin, T. R. Orientation selectivity sharpens motion detection in *Drosophila*. *Neuron* **88**, 390–402 (2015).
- Strother, J. A. et al. The emergence of directional selectivity in the visual motion pathway of *Drosophila*. *Neuron* **94**, 168–182 (2017).
- Fischbach, K.-F. & Dittrich, A. P. M. The optic lobe of *Drosophila melanogaster*. I. A Golgi analysis of wild-type structure. *Cell Tissue Res.* **258**, 441–475 (1989).
- Haag, J., Arenz, A., Serbe, E., Gabbiani, F. & Borst, A. Complementary mechanisms create direction selectivity in the fly. *eLife* **5**, e17421 (2016).
- Arenz, A., Drews, M. S., Richter, F. G., Ammer, G. & Borst, A. The temporal tuning of the *Drosophila* motion detectors is determined by the dynamics of their input elements. *Curr. Biol.* **27**, 929–944 (2017).
- Borst, A. A biophysical mechanism for preferred direction enhancement in fly motion vision. *PLoS Comput. Biol.* **14**, e1006240 (2018).
- Zavatone-Veth, J. A., Badwan, B. A. & Clark, D. A. A minimal synaptic model for direction selective neurons in *Drosophila*. *J. Vis.* **20**, 1–22 (2020).
- Torre, V. & Poggio, T. A synaptic mechanism possibly underlying directional selectivity to motion. *Proc. R. Soc. Lond. B* **202**, 409–416 (1978).
- Gruntman, E., Romani, S. & Reiser, M. B. Simple integration of fast excitation and offset, delayed inhibition computes directional selectivity in *Drosophila*. *Nat. Neurosci.* **21**, 250–257 (2018).
- Pankova, K. & Borst, A. RNA-seq transcriptome analysis of direction-selective T4/T5 neurons in *Drosophila*. *PLoS ONE* **11**, e0163986 (2016).
- Davis, F. P. et al. A genetic, genomic, and computational resource for exploring neural circuit function. *eLife* **9**, e50901 (2020).
- Hörmann, N. et al. A combinatorial code of transcription factors specifies subtypes of visual motion-sensing neurons in *Drosophila*. *Development* **147**, dev186296 (2020).
- Özel, M. N. et al. Neuronal diversity and convergence in a visual system developmental atlas. *Nature* **589**, 88–95 (2021).
- Gonçalves, P. J. et al. Training deep neural density estimators to identify mechanistic models of neural dynamics. *eLife* **9**, e56261 (2020).
- Denève, S. & Machens, C. K. Efficient codes and balanced networks. *Nat. Neurosci.* **19**, 375–382 (2016).
- Fendl, S., Vieira, R. M. & Borst, A. Conditional protein tagging methods reveal highly specific subcellular distribution of ion channels in motion-sensing neurons. *eLife* **9**, e62953 (2020).
- Bahl, A., Ammer, G., Schilling, T. & Borst, A. Object tracking in motion-blind flies. *Nat. Neurosci.* **16**, 730–738 (2013).
- Fenk, L. M., Poehlmann, A. & Straw, A. D. Asymmetric processing of visual motion for simultaneous object and background responses. *Curr. Biol.* **24**, 2913–2919 (2014).
- Huston, S. J. & Krapp, H. G. Nonlinear integration of visual and haltere inputs in fly neck motor neurons. *J. Neurosci.* **29**, 13097–13105 (2009).
- Haag, J., Wertz, A. & Borst, A. Central gating of fly optomotor response. *Proc. Natl Acad. Sci. USA* **107**, 20104–20109 (2010).
- Gabbiani, F., Krapp, H. G., Koch, C. & Laurent, G. Multiplicative computation in a visual neuron sensitive to looming. *Nature* **420**, 320–324 (2002).
- Lavzin, M., Rapoport, S., Polsky, A., Garion, L. & Schiller, J. Nonlinear dendritic processing determines angular tuning of barrel cortex neurons *in vivo*. *Nature* **490**, 397–401 (2012).
- Poleg-Polsky, A. & Diamond, J. S. NMDA receptors multiplicatively scale visual signals and enhance directional motion discrimination in retinal ganglion cells. *Neuron* **89**, 1277–1290 (2016).
- Meier, M. & Borst, A. Extreme compartmentalization in a *Drosophila* amacrine cell. *Curr. Biol.* **29**, 1545–1550 (2019).
- Srinivasan, M. V. & Bernard, G. D. A proposed mechanism for multiplication of neural signals. *Biol. Cybern.* **21**, 227–236 (1976).
- Abbott, L. F. Where Are the Switches on This Thing? In *23 Problems in Systems Neuroscience* (eds van Hemmen, J. L. & Sejnowski, T. J.) 423–431 (Oxford University Press, 2006).
- Schnupp, J. W. & King, A. J. Neural processing: the logic of multiplication in single neurons. *Curr. Biol.* **11**, R640–R642 (2001).
- Dobosiewicz, M., Liu, Q. & Bargmann, C. I. Reliability of an interneuron response depends on an integrated sensory state. *eLife* **8**, e50566 (2019).
- Pi, H.-J. et al. Cortical interneurons that specialize in disinhibitory control. *Nature* **503**, 521–524 (2013).

Publisher's note Springer Nature remains neutral with regard to jurisdictional claims in published maps and institutional affiliations.



Open Access This article is licensed under a Creative Commons Attribution 4.0 International License, which permits use, sharing, adaptation, distribution and reproduction in any medium or format, as long as you give appropriate credit to the original author(s) and the source, provide a link to the Creative Commons license, and indicate if changes were made. The images or other third party material in this article are included in the article's Creative Commons license, unless indicated otherwise in a credit line to the material. If material is not included in the article's Creative Commons license and your intended use is not permitted by statutory regulation or exceeds the permitted use, you will need to obtain permission directly from the copyright holder. To view a copy of this license, visit <http://creativecommons.org/licenses/by/4.0/>.

© The Author(s) 2022

Methods

Fly husbandry and genotypes

Flies were cultivated on a cornmeal, molasses and yeast medium under a 12 h–12 h light–dark cycle at 25 °C and 60% humidity. All of the experiments were carried out on female flies bearing at least one wild-type allele of the *white* gene. The experimenters were not blinded.

Drosophila melanogaster of the following genotypes were used to target transgene expression to the respective types of neuron: *P{R48A07-p65.AD}attP40*, *P{10XUAS-IVS-mCD8::GFP}su(Hw)attP5*; *P{VTO46779-GAL4.DBD}attP2* was used to label Mi9 neurons, *P{R13E12-p65.AD}attP40/+*; *P{R59C10-GAL4.DBD}attP2*; *P{40XUAS-IVS-mCD8::GFP}attP2* was used to label Tm3 neurons, *P{R19F01-p65.AD}attP40/+*; *P{R71D01-GAL4.DBD}attP2*; *P{40XUAS-IVS-mCD8::GFP}attP2* was used to label Mi1 neurons, *P{R48A07-p65.AD}attP40*, *P{10XUAS-IVS-mCD8::GFP}su(Hw)attP5*; *P{R13F11-GAL4.DBD}attP2* was used to label Mi4 neurons, *P{R26H02-p65.AD}attP40/+*; *P{R29G11-GAL4.DBD}attP2*; *P{40XUAS-IVS-mCD8::GFP}attP2* was used to label C3 neurons and *P{R42F06-p65.AD}attP40*, *P{10XUAS-IVS-mCD8::GFP}su(Hw)attP5*; *P{VTO37588-GAL4.DBD}attP2* (abbreviated T4 > GFP) was used to label T4 neurons, with a preference for subtypes T4c and T4d^{17,27,45,46}. In electrophysiological experiments, *P{TRiP.HMCO3585}attP40*; *P{R42F06-p65.AD}attP40*, *P{10XUAS-IVS-mCD8::GFP}su(Hw)attP5*; *P{VTO37588-GAL4.DBD}attP2/+* (abbreviated T4 > *GluClα^{RNAi}*) and *P{TRiP.HMSO2199}attP2*; *P{R42F06-p65.AD}attP40*, *P{10XUAS-IVS-mCD8::GFP}su(Hw)attP5*; *P{VTO37588-GAL4.DBD}attP2/+* (abbreviated T4 > *Nmdar1^{RNAi}*) were used to silence the expression of *GluClα* and *Nmdar1*, respectively⁴⁷.

In behavioural experiments, *P{UAS-Dcr-2.D}2*; *P{R39H12-GAL4}attP2* (abbreviated T4/T5 >), which yields strong and comprehensive expression in T4 and T5 neurons, was used to drive either *P{TRiP.HMCO3585}attP40* (abbreviated *GluClα^{RNAi}*) or *P{TRiP.HMSO2199}attP2* (abbreviated *Nmdar1^{RNAi}*). For the experiments in Extended Data Fig. 10c–f, *P{R59E08-p65.AD}attP40*; *P{R42F06-GAL4.DBD}attP2* was used as the driver line. All flies, including the parental controls, were heterozygous for the respective transgenes. *P{UAS-Dcr-2.D}2*; *P{10XUAS-IVS-mCD8::GFP}su(Hw)attP5*; *P{R39H12-GAL4}attP2/+* and *P{R59E08-p65.AD}attP40*; *P{10XUAS-IVS-mCD8::GFP}su(Hw)attP5*; *P{R42F06-GAL4.DBD}attP2/+* were used to visualize the expression pattern of the respective driver lines immunohistochemically.

With the exception of the strain used to label C3 (a gift from A. Nern and M. Reiser), all of the flies were obtained from the Bloomington *Drosophila* Stock Center.

Histology

Brains of female flies (aged 1–3 days) were dissected in phosphate-buffered saline (PBS; 137 mM NaCl, 3 mM KCl, 8 mM Na₂HPO₄, 1.5 mM KH₂PO₄, pH 7.3) and fixed in 4% (w/v) paraformaldehyde in PBS overnight at 4 °C, followed by four 30 min washes in PBS containing 0.2% (v/v) Triton X-100 (PBT). To label biocytin-filled neurons, the samples were incubated with DyLight 633-conjugated streptavidin (21844, Invitrogen, 1:200) for 48 h at 4 °C, followed by four 30 min washes in PBT. To visualize GFP expression patterns driven by *R39H12-GAL4* and *R59E08-AD*; *R42F06-DBD*, brains were fixed for 25 min at room temperature and blocked in PBT containing 10% normal goat serum (NGS) overnight at 4 °C. Synaptic structures and GFP were labelled, first with mouse anti-bruchpilot antibodies (nc82, AB2314866, Developmental Studies Hybridoma Bank, 1:20) and chicken anti-GFP antibodies (600-901-215S, Rockland, 1:400), respectively, for 48 h and then with Atto 647N-conjugated goat anti-mouse IgG antibodies (610-156-040, Rockland, 1:300) and Alexa 488-conjugated goat anti-chicken IgY antibodies (A-11039, Invitrogen, 1:500), respectively, for 72 h, both diluted in PBT containing 5% NGS, at 4 °C. Immunodecorated samples were mounted in Vectashield antifade mounting medium (Vector Laboratories) and imaged on a Leica TCS SP8 confocal microscope equipped with an HCX PL APO ×63/1.30 NA glycerol-immersion objective (506353,

Leica). Micrographs were acquired using the Leica Application Suite X (Leica) and processed using the Fiji distribution of ImageJ (v.2.0)⁴⁸.

Patch-clamp recordings

For whole-cell recordings *in vivo*^{49,50}, female flies aged 2–24 h post-eclosion were cold-anaesthetized and fixed to a custom, laser-cut polyoxymethylene mount with soft thermoplastic wax (Agar Scientific). The preparation was submerged in extracellular solution (pH 7.3) containing 5 mM TES, 103 mM NaCl, 3 mM KCl, 26 mM NaHCO₃, 1 mM NaH₂PO₄, 1.5 mM CaCl₂, 4 mM MgCl₂, 10 mM trehalose, 10 mM glucose and 7 mM sucrose (280 mOsm, equilibrated with 5% CO₂ and 95% O₂). Cuticle, adipose tissue and trachea were surgically removed in a window large enough to expose the left dorsal optic lobe. Patch pipettes (15–20 MΩ) were fabricated from borosilicate glass capillaries with outer and inner diameters of 1.5 mm and 1.17 mm or 0.86 mm, respectively, using a P-97 (Sutter Instruments) or a PC-10 (Narishige) micropipette puller. Pipettes were polished using a microforge (MF-830, Narishige) and filled with solution (pH 7.3) containing 10 mM HEPES, 140 mM potassium aspartate, 1 mM KCl, 4 mM MgATP, 0.5 mM Na₃GTP, 1 mM EGTA and 10 mM biocytin (265 mOsm). Green fluorescent somata were targeted visually using a combination of bright-field and epifluorescence microscopy on an InVivo SliceScope (Scientifica) or an Axio Scope.A1 microscope (Zeiss), each equipped with a ×60/1.0 NA water-immersion objective (LUMPLFLN60XW, Olympus) and an LQ-HXP 120 light source (Leistungselektronik Jena). Transillumination was achieved by butt-coupling a white LED (MCWHD5, Thorlabs) to a liquid light guide, the far end of which was positioned caudally at a distance of 1 cm to the fly allowing for an unobstructed field of view. To gain access to cell membranes, a micropipette was used to make a small incision in the perineural sheath. Signals were recorded at room temperature (21–23 °C) with a MultiClamp 700B amplifier, low-pass-filtered and sampled at 10 kHz using a Digidata 1550B digitizer controlled through pCLAMP 11 software (all from Molecular Devices). Data were corrected for the liquid junction potential and analysed using custom-written software in Python v.3.7 (Python Software Foundation) using NumPy v.1.15, Pandas v.0.25, SciPy v.1.3, Matplotlib v.3.0 and pyABF v.2.1 (<https://pypi.org/project/pyabf/>). After temporal alignment, current-clamp data were analysed at a sampling rate of 1 kHz. The most negative membrane potential recorded within 2 min after break-in, in darkness and in the absence of a holding current was taken to represent the resting potential. Only cells with a measured resting potential that was more negative than –25 mV were characterized further. Input resistances, as plotted in Fig. 2, were calculated on the basis of linear fits to the steady-state voltage changes elicited by 1 s steps of hyperpolarizing currents (2 pA increments, starting at –10 pA). In voltage-clamp recordings, voltage steps were applied 2 s in advance of pharmacological applications and linear leak currents were subtracted.

Visual stimulation in electrophysiological experiments

Visual stimuli were projected with two mirrors onto a cylindrical screen using two DLP Lightcrafter 3000 pico projectors (Texas Instruments) as previously described²⁰. The screen covered 180° in azimuth and 105° in elevation of the fly's left frontal visual field and doubled as a Faraday shield. Restricting the projectors to the green channel (500–600 nm) allowed for a refresh rate of 180 Hz at 8-bit colour depth and a maximal luminance of 1,274 cd m⁻². The average luminance of stimuli, which were presented in full contrast, was set to an 8-bit greyscale value of 128 corresponding to an average luminance of –637 cd m⁻². Stimuli were created and pre-distorted to account for the curvature of the screen using the Panda3D game engine in Python v.2.7.

Receptive fields were located and characterized using a binary white-noise stimulus with a pixel size of 2.8° × 2.8°. Samples were drawn at a rate of 60 Hz and projected onto the screen for durations ranging from 3 min to 20 min. Stimuli and simultaneously recorded membrane potentials were time-locked using a continuously recorded trigger

signal on the screen. Stimulus files were exported after lossless compression and cross-correlated to each neuron's recorded membrane voltage using standard techniques for reverse correlation in Python (v.3.7)²⁰. Slow voltage drifts were corrected post hoc by subtracting a low-pass-filtered version of the signal obtained using a Gaussian blur with a standard deviation of 60 s. The reverse correlation was calculated as

$$K(x, \tau) = \int_0^T dt S(x, t - \tau) \times V_m(t),$$

where V_m denotes the neuron's baseline-subtracted membrane voltage at time point t and S denotes the stimulus at position x and time point $t - \tau$ for values of τ ranging from -0.5 to $+3.0$ s. The resulting spatiotemporal receptive fields were converted into standard scores. Only neurons with clear standard score peaks (typically >4 s.d. from the mean) and with receptive field centres >8 px (22.48°) from the bezel of the screen were included in the analysis to guarantee full coverage of the surround. Receptive fields were normalized and aligned in space using the extremum (that is, the maximum or minimum with the highest absolute value) of the standard score as a point of reference, which was placed at 0°. After cropping the individual spatial receptive fields to the largest common region holding data from all neurons, scores were averaged across neurons of one class. For Fig. 1, averages were upsampled by a factor of 10 by linear interpolation and smoothed with a Gaussian filter (1.8 px s.d.). For direction-selective T4 neurons, individual receptive fields were rotated in space to align along the neurons' PDs; therefore, in Fig. 1e, azimuth and elevation do not necessarily correspond to horizontal and vertical coordinates on the screen, but to coordinates parallel and orthogonal to the T4 cell's PD.

To determine a neuron's PD, square-wave gratings with a spatial wavelength of 30° spanning the full extent of the screen were moved at a temporal frequency of 1 Hz in eight different directions separated by 45°. The neuron's peak membrane voltage during motion, after subtracting a 1 s prestimulus baseline, was taken to represent the magnitude of a Euclidean vector $\mathbf{v}(\varphi)$ pointing in the direction given by the angle of rotation φ of the associated stimulus. PD was defined as the direction of the resultant of all individual vectors. Temporal frequency tuning curves were measured using gratings of the above properties that were moved alternately in PD and ND (that is, PD + 180°) at temporal frequencies ranging from 0.5 Hz to 16.0 Hz. ΔV_m was defined as the absolute difference between the maximal and minimal membrane potential.

The fine-grained directional tuning curves in Fig. 5 were assessed using ON edges moving at 30° s⁻¹ in 36 evenly spaced directions. Membrane potentials were recorded in the presence of a constant holding current of -1 pA, which enabled stable recordings over extended periods of time. In Fig. 5c, $|\mathbf{v}(\varphi)|$ was defined as the maximum of a Voigt profile fit to the membrane potential in a 700 ms time window surrounding the peak response during motion in the respective direction using the VoigtModel function of the lmfit.models module in Python v.3.7. Thus the readout incorporated more data points than just the maxima of the raw traces. To make directional tuning curves comparable between experiments and genotypes, each neuron's PD was aligned post hoc to 0° and its tuning curve was minimum-maximum normalized. Directional tuning was quantified as the magnitude of the resultant vector divided by the sum of the individual vectors' magnitudes:

$$L_{\text{dir}} = \frac{\left| \sum_{\varphi} \mathbf{v}(\varphi) \right|}{\sum_{\varphi} |\mathbf{v}(\varphi)|}$$

For the experiments in Fig. 3, bright (ON) and dark (OFF) edges were moved across the screen at a velocity of 30° s⁻¹. The responses of individual neurons of one type were temporally aligned based on the cross-correlation maximum between the time derivative of the

low-pass-filtered membrane potential of each neuron and that of one hand-picked template neuron in response to ON edges (moving in PD for T4 cells). The responses of different input neuron classes were aligned based on the relative distances of the template neurons' receptive field centres on the screen. Correct alignment was verified by recording light intensities from a 5°-wide area of the screen located at the respective template neuron's receptive field centre using a custom-built photodiode under identical stimulus conditions.

Time-locked measurements of a T4 neuron's membrane potential and input resistance (Fig. 4 and Extended Data Fig. 9) were achieved through repeated presentations of identical stimuli with varying holding current amplitudes ranging from -5 to 0 pA. The slope of a linear regression of voltages onto holding currents provided a measure of the neuron's input resistance at each time point. For experiments with only two different holding current amplitudes, the slope of the regression is equivalent to the input resistance calculated as $\Delta V_m / \Delta I$, where ΔV_m denotes the change in membrane potential and ΔI denotes the change in holding current in between repetitions. Resistances shown in Fig. 4 were smoothed with a Gaussian filter (13 ms s.d.). Input resistances did not change significantly throughout recording sessions. The difference in input resistance between the start and the end of recording sessions averaged at 0.28 ± 0.56 G Ω (mean \pm s.e.m., $n = 30$ cells; $P = 0.6143$, two-tailed paired Student's t -test).

Pharmacology

For applications of glutamate, acetylcholine and GABA, a micropipette with a bore diameter of 5 μm was filled with 1 mM of neurotransmitter (dissolved in extracellular solution) and aimed at the GFP-labelled T4 dendrites in layer 10 of the medulla. To elicit transient neurotransmitter responses in patch-clamped T4 neurons, pressure (50 kPa) was applied in 100 ms pulses using a PDES-02DX pneumatic drug ejection system (NPI Electronic). For long-lasting responses during input resistance measurements, pulse times were increased to 500 ms. Two wild-type neurons were lost after the third glutamate application during patch-clamp recordings for Fig. 2e and were excluded from the repeated-measures analysis.

Multi-compartment model

We built a passive compartmental model of a T4 neuron (Extended Data Fig. 4c, d) in Python v.3.7 to account for possible space-clamp problems due to neuronal morphology in voltage-clamp experiments and to assess signal propagation between dendrite and soma (Extended Data Fig. 4e, f). The model was based on an electron microscopic reconstruction⁷ (http://neuromorpho.org/neuron_info.jsp?neuron_name=T4a-25_85) and comprised 2,012 compartments. A connectivity matrix, which held values of 1 where two compartments were connected and values of 0 otherwise, was used as a template to calculate a conductance matrix M . The latter was based on the three-dimensional coordinates and the length as well as the diameter of each compartment assuming, unless stated otherwise, an axial resistivity (R_a) of 150 Ω cm, a membrane resistance (R_m) of 28 k Ω cm², and a specific membrane capacitance (C_m) of 1 μF cm⁻². All parameters were on the same scale as those commonly used to model *Drosophila* neurons⁵¹ and were considered to be uniform across the entire cell. Varying R_a and R_m over a biophysically plausible range had negligible effects on model output (Extended Data Fig. 4f, g).

The voltage vector $\mathbf{V}_m(t)$ indicating the membrane potential of each compartment and at each time point t was determined by using the sparse.linalg.spsolve function of the SciPy v.1.3 module to iteratively solve the matrix equation $M \times \mathbf{V}_m(t) = \mathbf{V}_m(t-1) \times \mathbf{c}_m / \Delta t + E_{\text{leak}} \times \mathbf{g}_{\text{leak}} + \mathbf{I}(t)$, where $\mathbf{V}_m(t-1)$ denotes the voltage vector at the previous time point, \mathbf{c}_m is the vector holding the specific capacitances of all compartments, Δt denotes the time step, E_{leak} denotes the leak reversal potential, \mathbf{g}_{leak} denotes the vector holding the specific transmembrane leak conductances of all compartments and $\mathbf{I}(t)$ is the vector indicating the current

injected at time point t into each compartment. Simulations were performed with a fixed Δt of 0.1 ms. If only steady-state was considered, the diagonal of the conductance matrix M held no capacitive conductances and the right side of the equation simplified to $E_{\text{leak}} \times \mathbf{g}_{\text{leak}} + \mathbf{I}(t)$. At the time of transmitter application, synaptic conductances were added both to the diagonal of the conductance matrix and, multiplied by the reversal potential of the current, to the right side of the equation.

To simulate voltage clamp, the current injected at the soma was calculated on the basis of the difference between the chosen command voltage V_{cmd} and the actual potential at the soma $V_{\text{m,soma}}$ using a proportional-integral control loop that served to emulate a voltage-clamp amplifier in Python v.3.7. The current to be injected at time point t was calculated as $I(t) = K_p \times (V_{\text{cmd}}(t) - V_{\text{m,soma}}(t)) + K_i \times I(t-1)$; where K_p denotes the proportional gain and K_i the integral gain. With values of 2×10^9 and 1 for K_p and K_i , respectively, $V_{\text{m,soma}}$ could be clamped reliably at the desired V_{cmd} under all conditions and synaptic inputs.

Single-compartment model

Recorded membrane voltages of input neurons were averaged, minimum–maximum normalized (retaining the signal ratios across stimuli) and converted into relative conductances using a rectilinear transfer function with two free parameters per neuron: a threshold below which all conductances were set to 0 and a gain (that is, a scaling factor). Taking into account an average inter-ommatidial angle θ of 4.8° (refs. ^{52,53}) and the edge velocity v of 30° s^{-1} , conductances of Mi9 neurons and those of Mi4 and C3 neurons were advanced or delayed in time, respectively, by Δt relative to those of Mi1 and Tm3 neurons, depending on the angle φ of the virtual edge: $\Delta t = \theta \cos \varphi / v$.

For each stimulus condition, the membrane potential of the T4 neuron was calculated as

$$V_m = \frac{E_{\text{Glu}} g_{\text{Mi9}} + E_{\text{Ach}} (g_{\text{Tm3}} + g_{\text{Mi1}}) + E_{\text{GABA}} (g_{\text{Mi4}} + g_{\text{C3}}) + E_{\text{leak}} g_{\text{leak}}}{g_{\text{Mi9}} + g_{\text{Tm3}} + g_{\text{Mi1}} + g_{\text{Mi4}} + g_{\text{C3}} + g_{\text{leak}}},$$

where g denotes the relative conductance associated with each input neuron and E denotes the reversal potential of the respective synaptic current with $E_{\text{Glu}} = -71 \text{ mV}$, $E_{\text{Ach}} = -21 \text{ mV}$ and $E_{\text{GABA}} = -68 \text{ mV}$ as measured/ modelled in voltage-clamp experiments (Extended Data Fig. 4a–d). Owing to the compact size of a T4 neuron, the small amplitudes of capacitive currents (in relation to the steady-state amplitudes) and their short time constants (in relation to those of synaptic currents) eliminated the need for a differential equation to calculate V_m . Free parameters (thresholds, gains, E_{leak} and g_{leak}) were estimated from a least-squares fit to measured membrane voltage traces of T4 neurons, computed with the help of the optimize.minimize function of the SciPy v.1.3 module and hand-tuned using a FaderPort 16-channel mix production controller (Presonus). Upper and lower bounds for parameter values were set to 0 and 1 for thresholds, 0 and 2 for gains, -80 mV and -45 mV for E_{leak} , and 0 and 3 for g_{leak} , respectively. The parameters used for the simulations shown in Figs. 3b, c and 5a and Extended Data Figs. 7b, c and 8 were as follows: $\text{Mi9}_{\text{gain}} = 0.92$, $\text{Tm3}_{\text{gain}} = 0.35$, $\text{Mi1}_{\text{gain}} = 0.65$, $\text{Mi4}_{\text{gain}} = 1.10$, $\text{C3}_{\text{gain}} = 1.49$, $\text{Mi9}_{\text{thld}} = 0.20$, $\text{Tm3}_{\text{thld}} = 0.35$, $\text{Mi1}_{\text{thld}} = 0.88$, $\text{Mi4}_{\text{thld}} = 0.44$, $\text{C3}_{\text{thld}} = 0.70$, $E_{\text{leak}} = -65.0 \text{ mV}$ and $g_{\text{leak}} = 0.50$, where ‘thld’ refers to the respective threshold values.

To validate our choice of parameters and to quantify the sensitivity, robustness and uniqueness of parameter sets, we resorted to simulation-based inference²⁹, which enabled us to examine the full range of possible parameter combinations. We used 20,000 model simulations, drawing parameters from uniform distributions within the above bounds, to train the artificial neural network implemented in the sequential neural posterior estimation (SNPE) algorithm of the software package sbi (v.0.8)⁵⁴. On the basis of Bayesian inference, SNPE provided a conditional probability distribution $P(\alpha|V_{\text{data}})$, which is high for parameter sets α that are consistent with the experimentally measured voltage traces V_{data} , but close to zero otherwise.

To visualize $P(\alpha|V_{\text{data}})$ we drew 10,000 sample parameter sets that are compatible with V_{data} and compared them to our chosen parameters (Extended Data Fig. 6). All of the simulations were written in Python v.3.7.

Behaviour

Female flies (aged 1–5 days) were cold-immobilized and attached to a pin with light-curing composite glue (Sinfony Opaque Dentin, 3M) using dental curing light (440 nm, New Woodpecker). Five independent locomotion recorders³² were operated in parallel. In each recorder, a tethered fly was positioned on top of an air-suspended polyurethane sphere with a diameter of 6 mm and a weight of around 40 mg. The sphere floated freely on an air stream supplied by a rotary vane pump (G6/01-K-EB9L, Gardner Denver Thomas) through an inlet at the bottom of a concave holder, allowing the walking fly to rotate the sphere about any axis through its centre. The rotation of the spherical treadmill, lit by an infrared LED (JET-800-10, Roithner Electronics), was tracked at 4 kHz and digitized at 200 Hz using a custom-designed system based on two optical computer mouse sensors focused on two 1 mm^2 equatorial squares at $\pm 30^\circ$ from the centre of the sphere⁵⁵. A camera (GRAS-20S4M-C, Point Grey Research) was used to facilitate proper positioning of the fly on the ball. To encourage prolonged walking, the air temperature surrounding the fly was maintained at $34 \pm 0.1^\circ \text{ C}$ using a custom-built air conditioning system with a Peltier heater (QC-127-1.4-6.0MS, Quick-Cool) and a thermometer positioned below the sphere.

Visual stimuli were presented with a refresh rate of 120 Hz on three liquid crystal displays (2233RZ, Samsung) arranged vertically to form a U-shaped visual arena surrounding the fly, which spanned approximately 270° in azimuth and 120° in elevation of the fly’s visual field at a resolution of $< 0.1^\circ$. The maximal luminance of the displays was 131 cd m^{-2} ; the average intensity of stimuli, which were presented at a Michelson contrast of 50%, was set to an 8-bit greyscale value of 100. Stimuli were created, and predistorted to mimic a cylindrical panorama, using the Panda3D game engine in Python v.2.7.

In open-loop experiments, ON and OFF edges were moved at a velocity of 60° s^{-1} in 16 evenly spaced directions. Owing to the geometry of the visual arena, full translation of edges at different angles required variable amounts of time. Thus, to limit stimulus durations to 5 s, an edge of which the direction of motion deviated from the cardinal directions was initialized with a small segment of the edge already present in one of the outer corners (never covering any part of the central display). Edges started moving 0.5 s after stimulus initialization and crossed the arena within 5 s. In a single experiment ($\sim 80 \text{ min}$), flies experienced 50 trials of either ON or OFF edges moving in all 16 directions in a pseudorandom order. The first 15 trials were used to equilibrate the temperature and to accustom the fly to the treadmill and were excluded from analyses. As inclusion criteria, we used a forward walking speed of $\geq 0.15 \text{ cm s}^{-1}$ on a trial-by-trial basis and a minimum of ten trials per fly. To correct for a possible constant turning bias, the time-averaged rotational velocity of each full trial (comprising all 16 directions) was subtracted from all measurements of the corresponding trial. The optomotor response was quantified as the average rotational velocity during 5 s of edge motion in the corresponding direction. The slope of a linear regression of optomotor responses onto the absolute horizontal stimulus components $|\cos \varphi|$ served as a single measure of an animal’s angular velocity across different edge angles φ .

In closed-loop experiments, bar-fixation was assessed using a 10° -wide dark vertical bar, the position of which along the azimuth was controlled in real time by the rotation of the spherical treadmill ($\Delta \text{bar position} = -\text{rotation about z axis}$, updated every $\sim 9 \text{ ms}$). The bar appeared at a random position between -180° and 180° at the start of each 20 s trial, during which the fly could control the bar’s position through its walking behaviour. One experiment ($\sim 60 \text{ min}$) consisted of 180 trials, the first 40 of which were not analysed, as they served to equilibrate the temperature and to accustom the fly to the virtual

environment. For the results presented in Extended Data Fig. 10d–f, each experiment consisted of 80 longer multi-stimulus trials, the first 10 of which were excluded. Only trials with a forward walking velocity of $\geq 0.40 \text{ cm s}^{-1}$ and flies with at least 50 (20 for Extended Data Fig. 10d–f) of such trials were included in the analysis. To avoid possible turning bias (for example, due to skewed mounting), flies whose average turning deviated from zero by $>10^\circ \text{ s}^{-1}$ were excluded. Probability density functions of bar positions were calculated for each 20 s trial using a bin width of 5° before averaging over trials. The measure ‘fixation in front’ was obtained by summing the probabilities of finding the bar in a 60° window in front of the fly and averaging these probabilities over trials.

Statistics and reproducibility

Statistical tests were performed in Prism v.9.2 (GraphPad). Details, including test statistics, degrees of freedom and exact P values for statistical analyses of data shown in Figs. 2 and 5 and Extended Data Fig. 10 are reported in Supplementary Tables 1 and 2.

Data were assessed for normality and equality of variances using Shapiro–Wilk and Brown–Forsythe tests, respectively. Two groups of normally distributed data were compared using two-tailed Student’s t -tests (paired if applicable). Two groups of nonparametric data were compared using two-tailed Mann–Whitney U -tests for independent datasets and using Wilcoxon matched-pairs signed-ranks test for paired datasets. Differences between the means of multiple independent groups of data that met the assumptions of normality and equality of variances were compared using one-way ANOVA followed by Holm–Šidák’s multiple-comparisons test. Where the assumptions of normality or of equality of variances were violated, group means were compared using Kruskal–Wallis tests followed by Dunn’s multiple-comparisons test or by Welch’s ANOVA followed by Dunnett’s T3 multiple-comparisons test, respectively. Reported P values were corrected for multiple comparisons. Data shown in Fig. 2e were analysed using two-way repeated measures ANOVA with Geisser–Greenhouse correction. For multiple comparisons with parental controls, the highest of two P values was reported in the figure legend.

No sample size calculations were performed before experimentation. Sample sizes were chosen to match or exceed standard sample sizes in the field. Sample sizes in electrophysiological experiments correspond to the number of cells, each of which was recorded in a different animal. Sample sizes in behavioural experiments correspond to the number of flies. The investigators were not blinded. Randomization was not applicable, because flies were grouped on the basis of genotype. In open-loop behavioural experiments (Fig. 5d–f) and all experiments involving two directions of visual stimuli, stimulus directions were alternated randomly; all of the remaining visual stimuli were presented in a strict sequence to enable quick, intuitive interpretation (Figs. 1f and 5b). Two wild-type neurons were lost after the third glutamate application during patch-clamp recordings for Fig. 2e and were excluded from the repeated-measures analysis. Six cells were lost during voltage-clamp experiments shown in Fig. 2f and Extended Data Fig. 4b due to pneumatic ejection. The current–voltage relationships of those cells do not include all, but at least six, data points per cell.

Reporting summary

Further information on research design is available in the Nature Research Reporting Summary linked to this paper.

Data availability

Data are available at the Edmond Open Research Data Repository of the Max Planck Society (<https://doi.org/10.17617/3.8g>). Source data are provided with this paper.

Code availability

Custom-written code is available at the Edmond Open Research Data Repository of the Max Planck Society (<https://doi.org/10.17617/3.8g>).

45. Tuthill, J. C., Nern, A., Holtz, S. L., Rubin, G. M. & Reiser, M. B. Contributions of the 12 neuron classes in the fly lamina to motion vision. *Neuron* **79**, 128–140 (2013).
46. Schilling, T., Ali, A. H., Leonhardt, A., Borst, A. & Pujol-Martí, J. Transcriptional control of morphological properties of direction-selective T4/T5 neurons in *Drosophila*. *Development* **146**, dev169763 (2019).
47. Ni, J.-Q. et al. A genome-scale shRNA resource for transgenic RNAi in *Drosophila*. *Nat. Methods* **8**, 405–407 (2011).
48. Schindelin, J. et al. Fiji: an open-source platform for biological-image analysis. *Nat. Methods* **9**, 676–682 (2012).
49. Wilson, R. I., Turner, G. C. & Laurent, G. Transformation of olfactory representations in the *Drosophila* antennal lobe. *Science* **303**, 366–370 (2004).
50. Groschner, L. N., Chan Wah Hak, L., Bogacz, R., DasGupta, S. & Miesenböck, G. Dendritic integration of sensory evidence in perceptual decision-making. *Cell* **173**, 894–905 (2018).
51. Gouwens, N. W. & Wilson, R. I. Signal propagation in *Drosophila* central neurons. *J. Neurosci.* **29**, 6239–6249 (2009).
52. Götz, K. G. Optomotorische Untersuchung des visuellen Systems einiger Augenmutanten der Fruchtfliege *Drosophila*. *Kybernetik* **2**, 77–92 (1964).
53. Land, M. F. Visual acuity in insects. *Annu. Rev. Entomol.* **42**, 147–177 (1997).
54. Tejero-Cantero, A. et al. sbi: A toolkit for simulation-based inference. *J. Open Source Softw.* **5**, 2505 (2020).
55. Seelig, J. D. et al. Two-photon calcium imaging from head-fixed *Drosophila* during optomotor walking behavior. *Nat. Methods* **7**, 535–540 (2010).

Acknowledgements We thank A. Nern, M. Reiser, G. Rubin, L. Luo and T. Schilling for flies; M. Drews and A. Leonhardt for software; S. Prech for technical assistance; and G. Ammer, N. Hörmann and J. Pujol-Martí for discussions. This work was supported by the Max Planck Society, an EMBO Long-Term Fellowship ALTF 365-2019 to L.N.G. and by the European Union’s Horizon 2020 programme under the Marie Skłodowska-Curie Action MOVIS grant agreement no. 896143 to L.N.G. Flies obtained from the Bloomington *Drosophila* Stock Center (NIH P40OD018537) were used in this study.

Author contributions L.N.G., J.G.M. and A.B. conceived the study, designed experiments and ran model simulations. L.N.G. and J.G.M. performed and analysed electrophysiological recordings. L.N.G., J.G.M. and B.Z. performed histological analyses and B.Z. conducted and analysed behavioural experiments. The manuscript was written by L.N.G. and edited by all of the authors, chiefly by B.Z.

Funding Open access funding provided by the Max Planck Society.

Competing interests The authors declare no competing interests.

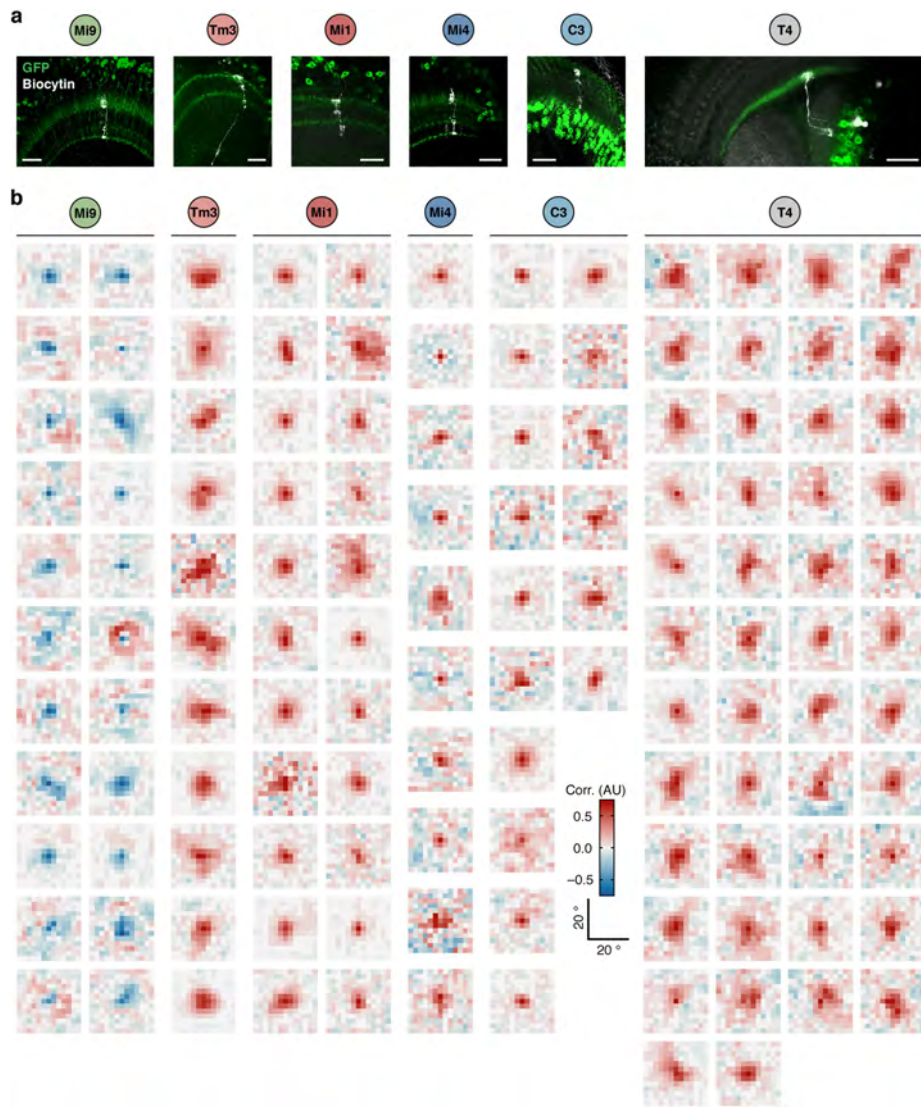
Additional information

Supplementary information The online version contains supplementary material available at <https://doi.org/10.1038/s41586-022-04428-3>.

Correspondence and requests for materials should be addressed to Lukas N. Groschner or Alexander Borst.

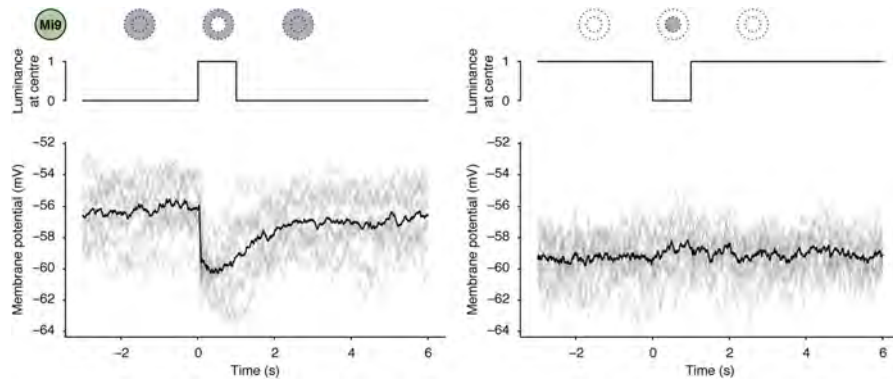
Peer review information Nature thanks Holger Krapp and Botond Roska for their contribution to the peer review of this work.

Reprints and permissions information is available at <http://www.nature.com/reprints>.



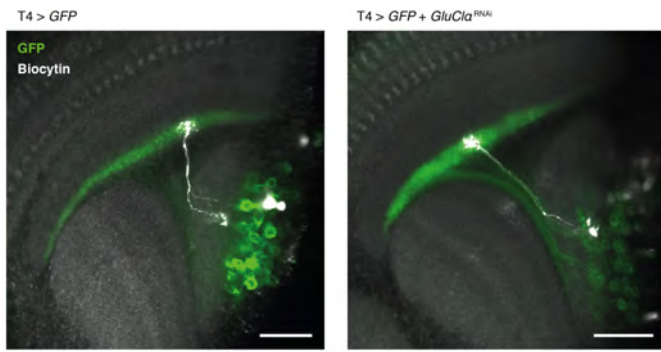
Extended Data Fig. 1 | Neuronal morphologies and receptive fields of the ON motion detection circuit. **a**, Maximum intensity projections of confocal stacks with GFP expression in the respective neuronal population (green) and single biocytin-filled neurons (white) recovered after patch-clamp recordings. Scale bars, 20 μ m. Micrographs are representative of independent

experiments in different flies (Mi9: $n = 5$, Tm3: $n = 3$, Mi1: $n = 3$, Mi4: $n = 4$, C3: $n = 3$, T4: $n = 7$). **b**, Individual spatial receptive fields of T4 and their columnar input neurons obtained by reverse correlation (corr.) of membrane potentials and white noise stimuli. AU, arbitrary units. Filtered averages are shown in Fig. 1d, e.

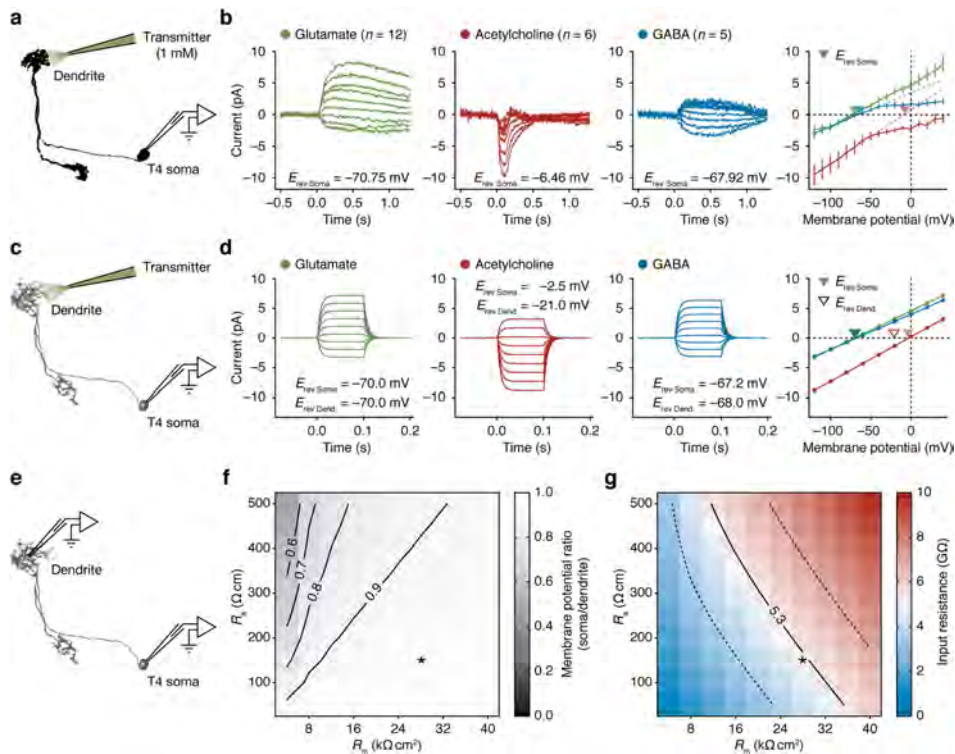


Extended Data Fig. 2 | Mi9 neurons hyperpolarize in response to luminance increments. Membrane potential responses of the same Mi9 neurons to increments (left) and decrements in luminance (right) presented in a 5° circle at the centre of the neurons' receptive fields on a dark or bright background,

respectively. Traces on top are normalized light intensities at the respective receptive field centre. The light lines represent technical replicates; the dark lines represent the mean; $n = 14$ technical replicates/2 cells/2 flies. Note the difference in membrane potential depending on the baseline luminance.

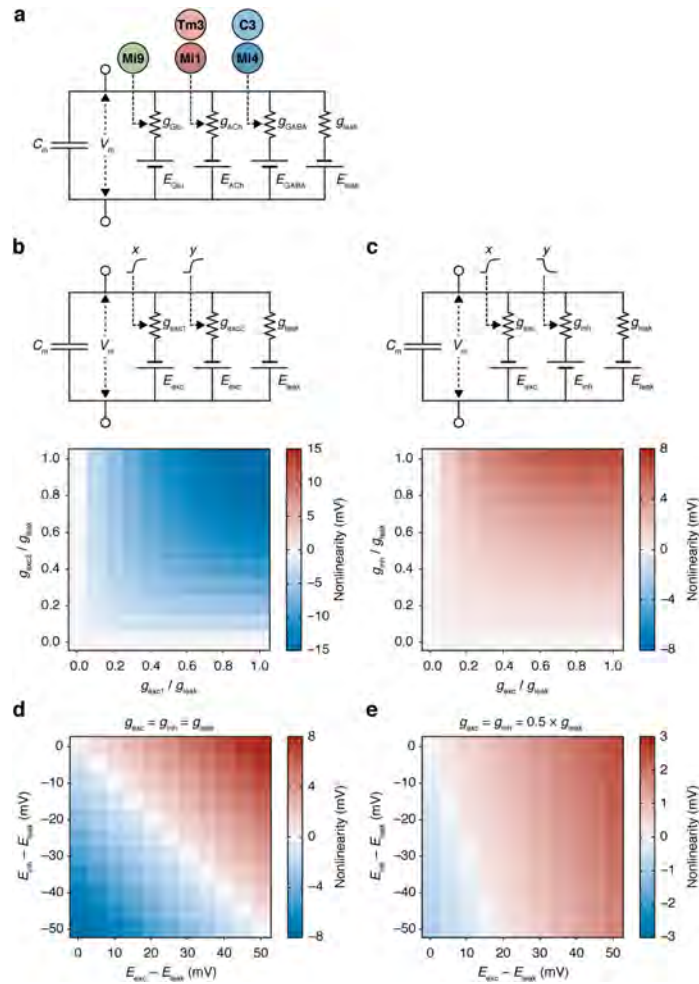


Extended Data Fig. 3 | Morphology of wild-type and *GluCl α* -deficient T4 neurons. Maximum intensity projections of representative confocal stacks of T4 neurons expressing *GFP* (left) or *GFP* and *GluCl α ^{RNAi}* (right), each containing an individual biocytin-filled neuron (white) recovered after patch-clamp recording. The soma of the *GluCl α ^{RNAi}*-expressing neuron was lost during pipette removal. Scale bars, 20 μ m. Micrographs are representative of independent experiments in different flies (*T4 > GFP*: $n = 7$ and *T4 > GFP + GluCl α ^{RNAi}*: $n = 3$). At the light microscopic level, no obvious genotype-specific morphological differences were detectable.



Extended Data Fig. 4 | Measured and modelled T4 whole-cell currents in response to three types of neurotransmitter. **a**, Placement of pipettes for neurotransmitter application during whole-cell recording. **b**, Average whole-cell currents of T4 neurons in response to 100 ms applications of neurotransmitter to the dendrite at different holding potentials (left) and full current-voltage relationships (right). Coloured dashed lines are linear fits to measurements taken at membrane potentials in the physiologically observed range between -100 and -40 mV. Filled triangles denote reversal potentials obtained by linear fits to currents measured at the soma ($E_{rev,Soma}$). Data are mean \pm s.e.m. n values indicate the number of cells. The inward rectification of GABA-induced currents could be due to coupling of GABA_B receptors to inwardly-rectifying potassium channels. **c**, Electron microscopical reconstruction of a T4 neuron⁷ used for compartmental modelling. Pipettes indicate approximate locations of conductances and the recording site for simulations in **d**. **d**, Somatic currents at different holding potentials simulated during 100 ms openings of conductances at the electron microscopically-determined synaptic sites corresponding to the respective transmitter (left) and

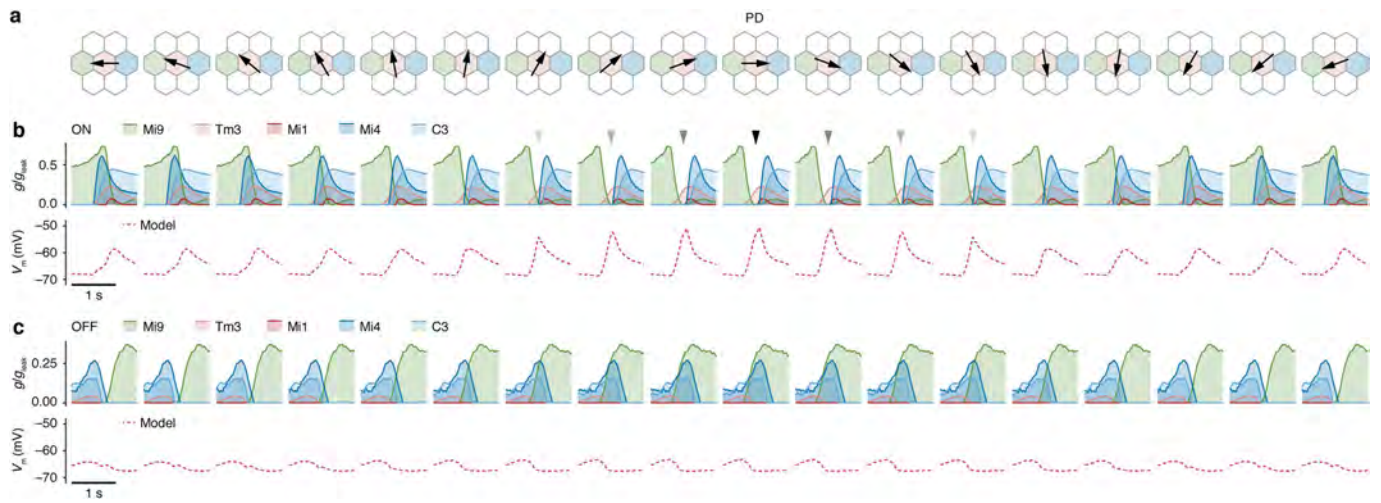
current-voltage relationships (right). Conductances were adjusted in order to approximate measured reversal potentials at the soma. Filled triangles denote modelled reversal potentials at the soma ($E_{rev,Soma}$); open triangles denote corresponding reversal potentials at the dendritic root ($E_{rev,Dend}$). Note the predicted deviation of $E_{rev,Soma}$ from $E_{rev,Dend}$, for currents induced by acetylcholine, but not for currents induced by glutamate or GABA. **e**, Pipettes indicate locations of recording sites on the compartmental model (**c**) for simulations in **f**. **f**, Ratio of somatic to dendritic membrane potential in response to dendritic injection of 10 pA of depolarizing current as a function of membrane resistance (R_m) and axial resistivity (R_a) in the model. Note that soma and dendrite were quasi-isopotential (ratio > 0.9) across a wide range of parameters. Asterisk indicates parameter set used for simulations in **d**. **g**, Modelled somatic input resistance as a function of R_m and R_a . Solid and dashed lines correspond to the measured mean input resistance \pm s.d. for wild-type T4 neurons (as shown in Fig. 2h). Asterisk indicates parameter set used for simulations in **d**.



Extended Data Fig. 5 | Nonlinear response properties of model circuits.

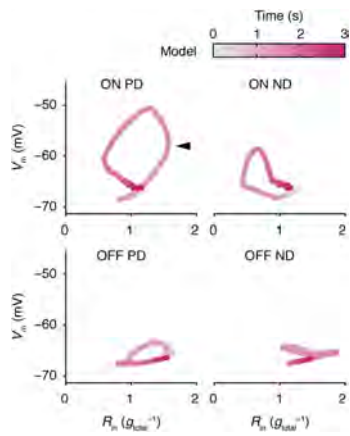
a, Resistor-capacitor equivalent circuit of a passive T4 neuron used for simulations in Fig. 3b, c, and 5a and Extended Data Figs. 6, 7, and 8. E_{Glu} , E_{ACh} , and E_{GABA} denote the equilibrium potentials and g_{Glu} , g_{ACh} , and g_{GABA} denote the conductances associated with glutamate, acetylcholine and GABA, respectively. The signals of Mi9 neurons control g_{Glu} , the signals of Tm3 and Mi1 neurons control g_{ACh} , and those of C3 and Mi4 neurons act on g_{GABA} . V_m , membrane potential; C_m , membrane capacitance; g_{leak} , leak conductance. **b, c**, Top: Equivalent circuits of two passive isopotential neurons. One neuron (**b**) receives two input signals x and y , which control the excitatory conductances g_{exc1} and g_{exc2} , respectively. The other neuron (**c**) receives one input signal x controlling the excitatory conductance g_{exc} and another input

signal y of opposite polarity that controls the inhibitory conductance g_{inh} . E_{exc} , E_{inh} , and E_{leak} are the equilibrium potentials of excitatory, inhibitory, and leak currents, respectively. Bottom: Nonlinearity as a function of signal amplitude for two excitatory conductances (**b**) and for one excitatory and the release from an inhibitory conductance (**c**). Nonlinearity was defined as the difference between the voltage response to both coincident inputs and the sum of the responses to each individual input. Equilibrium potentials were set to $E_{exc} - E_{leak} = 50$ mV and $E_{inh} - E_{leak} = -10$ mV. **d, e**, Nonlinearity of the circuit in **c** as a function of E_{exc} and E_{inh} . Conductances were set to $g_{exc} = g_{inh} = g_{leak}$ (**d**) or $g_{exc} = g_{inh} = 0.5 \times g_{leak}$ (**e**). Disinhibition supports supralinear responses over a wide range of equilibrium potentials and input signal amplitudes.

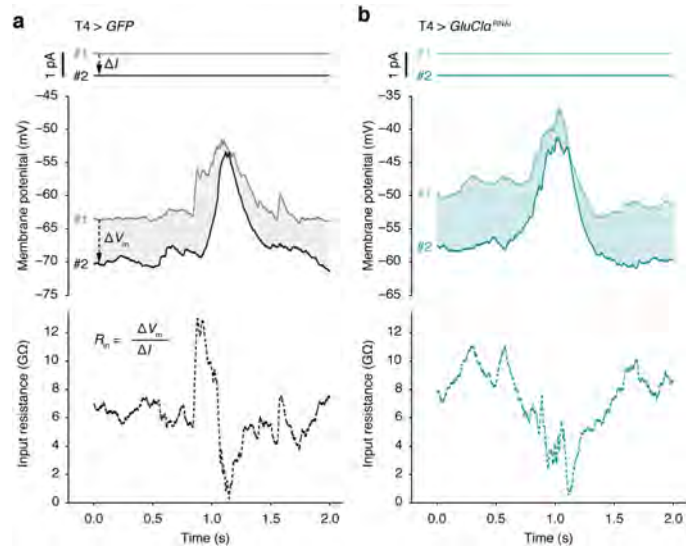


Extended Data Fig. 7 | A direction-selective ‘window of opportunity’.
a, Schematic columnar organization of T4 neuron inputs. Synapses from Mi9 neurons (green), Tm3/Mi1 neurons (red), and Mi4/C3 neurons (blue) are each separated by one column (hexagons) resulting in direction-dependent time differences during visual motion. Arrows indicate the directions of edge motion in corresponding panels in **b** and **c**. **b, c**, Top: Normalized T4 cell

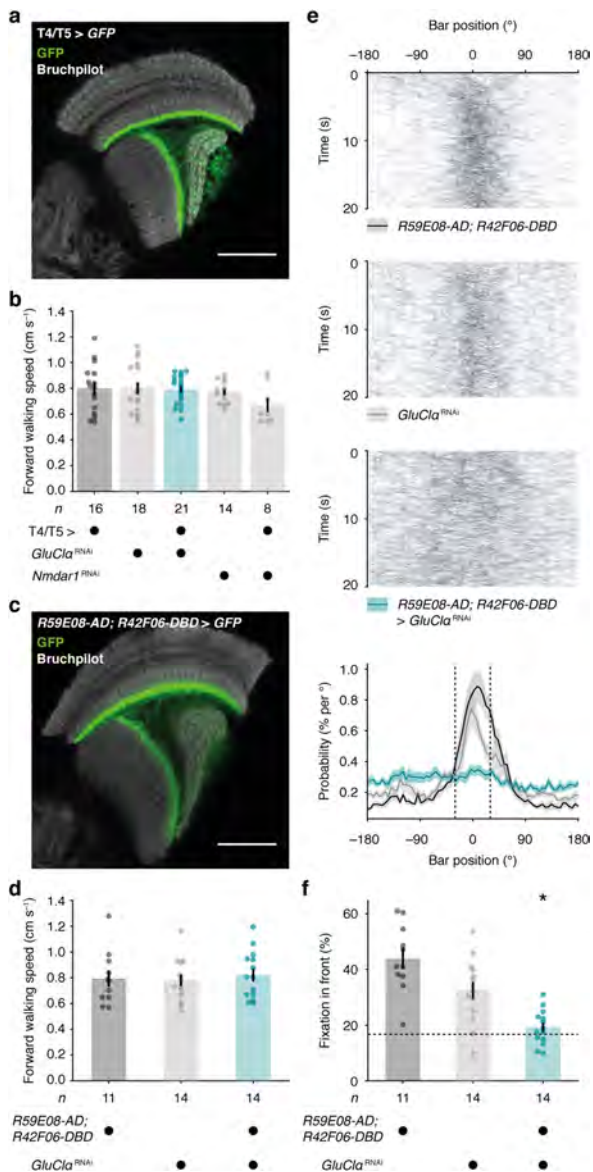
conductances (g/g_{leak}) of respective input synapses during ON (**b**) and OFF edge motion (**c**) at a velocity of 30° s^{-1} in the directions indicated in **a** using the same model parameters as in Figs. 3b, c, and 5a and Extended Data Fig. 8. Data are mean and area under curve. Arrowheads in **b** mark the coincidence of increased excitability and cholinergic excitatory input (red). Bottom: T4 cell membrane voltage (V_m) responses predicted by the model.



Extended Data Fig. 8 | Predicted relationship between membrane potential and input resistance during edge motion. Simulated T4 cell membrane potential (V_m) as a function of input resistance (R_{in}) in response to ON (top) and OFF edges (bottom) moving at 30° s^{-1} in the preferred (PD, left) and the null direction (ND, right) of the model. The arrowhead marks the peak in input resistance.



Extended Data Fig. 9 | Input resistance measurements during visual stimulation. Holding currents (solid lines, top), membrane potentials (solid lines, centre), and input resistances (dashed lines, bottom) of exemplary T4 neurons expressing either *GFP* (**a**) or *GFP + GluCl α ^{RNAi}* (**b**). To obtain input resistance measurements at high temporal resolution, neurons were subjected to at least two repetitions of identical visual stimulation while recording their membrane potentials. In this case, the stimulus was an ON edge moving at 30° s^{-1} in the neuron's preferred direction. The holding current I was altered in between the first (#1) and the second repetition (#2) by $\Delta I = -1 \text{ pA}$. The input resistance R_{in} at each time point was calculated as $\Delta V_m / \Delta I$, where ΔV_m denotes the difference in membrane potential between repetitions (shaded areas/dashed arrows in **a**).



Extended Data Fig. 10 | GAL4 expression patterns, walking speeds, and bar fixation.

a, Confocal cross section through the optic lobe of a fly expressing *GFP* (green) under control of *R39H12-GAL4* (T4/T5 >) as used in behavioural experiments in Fig. 5d–i. Synaptic structures were counterstained with an antibody against bruchpilot (grey). Scale bar, 40 μ m. The micrograph is representative of 8 biological replicates. **b**, Average forward walking speeds of flies expressing *GluCla*^{RNAi} (teal) or *Nmdar1*^{RNAi} (grey) in T4/T5 neurons and their parental controls (black/grey) during closed-loop bar fixation experiments in Fig. 5h, i. **c**, Confocal cross section through the optic lobe of a fly expressing *GFP* (green) under control of the split GAL4 line *R59E08-AD; R42F06-DBD*. Synaptic structures were counterstained with an antibody against bruchpilot (grey). Scale bar, 40 μ m. The micrograph is representative of 5 biological replicates. **d**, Average forward walking speeds of flies expressing *GluCla*^{RNAi} (teal) under control of *R59E08-AD; R42F06-DBD* and their parental controls (black/grey) during closed-loop bar fixation in **e**, **f**. **e**, Exemplary bar trajectories (242 trials and 11 flies per genotype, top) and the overall bar position probabilities (bottom) for flies expressing *GluCla*^{RNAi} (teal) under control of *R59E08-AD; R42F06-DBD* and their parental controls (black/grey). Data are mean \pm s.e.m. of flies in **f**. **f**, The percentage of time that the bar occupied a central 60° window (fixation in front, dashed lines in **e**). The dashed line indicates the chance level. Circles, individual flies; bars, mean \pm s.e.m. Asterisk denotes a significant difference from both parental controls ($P = 0.0012$, one-way ANOVA followed by Holm–Šidák’s multiple comparisons test). n values indicate the number of flies.

Supplementary information

A biophysical account of multiplication by a single neuron

In the format provided by the authors and unedited

Supplementary information

Supplementary equations

Here, we examine under which conditions a passive membrane can give rise to multiplication-like signal amplification. To extract the nonlinearity, we compare the response to two coincident inputs with the sum of the responses to each individual input presented in temporal isolation ('linear expectation'). We consider the simple case of an electrical equivalent circuit of a passive isopotential neuron that receives two excitatory input signals x and y , which control the excitatory conductances g_{exc1} and g_{exc2} , respectively (Extended Data Fig. 5b). The neuron's membrane potential V_m at steady state is given by

$$V_m = \frac{E_{exc}(g_{exc1} + g_{exc2}) + E_{leak}g_{leak}}{g_{exc1} + g_{exc2} + g_{leak}};$$

where E_{exc} and E_{leak} are the reversal potentials of excitatory and leak currents, respectively, and g_{leak} is the leak conductance. In the absence of input signals (i.e. when $x = y = 0$), the neuron's resting potential $V_{rest} = E_{leak}$.

If we express the membrane potential response ΔV as the difference between V_m and V_{rest} and all conductances relative to g_{leak} , then the membrane potential response to two coincident excitatory inputs is

$$\Delta V = \frac{E_{exc}(g_{exc1} + g_{exc2}) + E_{leak}}{g_{exc1} + g_{exc2} + 1} - V_{rest}.$$

For $g_{exc1} = x$, $g_{exc2} = y$, and $V_{rest} = E_{leak} = 0$ the response to the combined inputs can be written as

$$\Delta V_{1,2} = E_{exc} \frac{x+y}{x+y+1}.$$

The individual responses ΔV_1 and ΔV_2 to each input presented in isolation are

$$\Delta V_1 = E_{exc} \frac{x}{x+1} \quad \text{and} \quad \Delta V_2 = E_{exc} \frac{y}{y+1}.$$

Now we show that, for two excitatory inputs, $\Delta V_{1,2}$ is always smaller than the linear expectation $\Delta V_1 + \Delta V_2$:

$$E_{exc} \frac{x+y}{x+y+1} < E_{exc} \frac{x}{x+1} + E_{exc} \frac{y}{y+1}.$$

Factoring out E_{exc} , we obtain

$$\frac{x+y}{x+y+1} < \frac{x}{x+1} + \frac{y}{y+1}.$$

The left expression can be broken into two components:

$$\frac{x}{x+y+1} + \frac{y}{x+y+1} < \frac{x}{x+1} + \frac{y}{y+1}.$$

If follows that, for positive non-zero values of x and y ,

$$\frac{x}{x+y+1} < \frac{x}{x+1} \quad \text{and} \quad \frac{y}{x+y+1} < \frac{y}{y+1}.$$

If $a < c$ and $b < d$, then $a + b < c + d$. Therefore, the response of a passive neuron to two coincident excitatory inputs $\Delta V_{1,2}$ is always sublinear; i.e. smaller than the linear expectation $\Delta V_1 + \Delta V_2$ (Extended Data Fig. 5b).

Next, we consider the pairing of an excitatory with an inhibitory input (Extended Data Fig. 5c). This neuron's steady-state membrane potential is

$$V_m = \frac{E_{exc}g_{exc} + E_{inh}g_{inh} + E_{leak}g_{leak}}{g_{exc} + g_{inh} + g_{leak}}.$$

As before, we let $g_{exc} = x$, but the inhibitory conductance g_{inh} follows $1 - y$, meaning that it decreases with increasing signal y (just like Mi9 neurons hyperpolarize with increasing light intensity). Again, we express the membrane potential response ΔV as the difference between V_m and V_{rest} and all conductances relative to g_{leak} :

$$V_m = \frac{E_{exc}x + E_{inh}(1-y) + E_{leak}}{x + (1-y) + 1} \quad \text{and}$$

$$\Delta V = V_m - V_{rest}.$$

All reversal potentials are expressed as the difference to E_{leak} , which we set to zero ($E_{leak} = 0$). Note that, unlike before, the neuron's membrane potential at rest (i.e. when $x = y = 0$) is now $V_{rest} = E_{inh}/2$. The response to the combined inputs is

$$\Delta V_{1,2} = \frac{E_{exc}x + E_{inh}(1-y)}{x - y + 2} - \frac{E_{inh}}{2};$$

which can be written as

$$\Delta V_{1,2} = \frac{x(2E_{exc} - E_{inh}) - yE_{inh}}{2(2 + x - y)}.$$

The individual responses are

$$\Delta V_1 = \frac{x(2E_{exc} - E_{inh})}{2(2 + x)} \quad \text{and} \quad \Delta V_2 = \frac{-yE_{inh}}{2(2 - y)}.$$

In the following, we show under which conditions, $\Delta V_{1,2}$ is larger than the linear expectation $\Delta V_1 + \Delta V_2$:

$$\frac{x(2E_{exc} - E_{inh}) - yE_{inh}}{2(2 + x - y)} > \frac{x(2E_{exc} - E_{inh})}{2(2 + x)} - \frac{yE_{inh}}{2(2 - y)}.$$

This simplifies to

$$\frac{x(2E_{exc} - E_{inh}) - yE_{inh}}{2 + x - y} > \frac{x(2E_{exc} - E_{inh})}{2 + x} - \frac{yE_{inh}}{2 - y}.$$

Put over a common denominator, it can be written as

$$(x(2E_{exc} - E_{inh}) - yE_{inh})(2 + x)(2 - y) > x(2E_{exc} - E_{inh})(2 + x - y)(2 - y) - yE_{inh}(2 + x - y)(2 + x).$$

Expansion leads to

$$\begin{aligned} & x(2E_{exc} - E_{inh})(2 + x)(2 - y) - yE_{inh}(2 + x)(2 - y) > \\ & x(2E_{exc} - E_{inh})(2 + x)(2 - y) - xy(2E_{exc} - E_{inh})(2 - y) - yE_{inh}(2 - y)(2 + x) - \\ & xyE_{inh}(2 + x). \end{aligned}$$

Subtraction of the blue and the red expressions on both sides yields

$$0 > -xy(2E_{exc} - E_{inh})(2 - y) - xyE_{inh}(2 + x).$$

Division by $(-xy)$ reverses the inequality sign:

$$(2E_{exc} - E_{inh})(2 - y) + E_{inh}(2 + x) > 0.$$

This simplifies to

$$2E_{exc}(2 - y) + E_{inh}(y + x) > 0;$$

or

$$E_{exc} > -E_{inh} \frac{x+y}{2(2-y)}.$$

Note that E_{exc} and E_{inh} are expressed as the difference to E_{leak} . For $0 \leq x \leq 1$ and $0 \leq y \leq 1$ (i.e. positive conductances smaller or equal to g_{leak}) and $|E_{exc}| > |E_{inh}|$, the above inequality always holds. In the extreme case of $x = y = 1$ the coincidence of an excitatory input with the release from an inhibitory one gives rise to a supralinearity as long as E_{inh} is closer to E_{leak} than E_{exc} (Extended Data Fig. 5d). Other values of x and y yield supralinear responses over much wider ranges of E_{exc} and E_{inh} (Extended Data Fig. 5e).

Supplementary Table 1. Statistical analyses of Figs. 2, 5.

Figure	Statistical test	Measured variable	Experimental groups/comparisons	Test statistic	P
2c	Shapiro–Wilk test Shapiro–Wilk test Two-tailed paired Student's <i>t</i> -test Two-tailed Wilcoxon matched-pairs signed rank test	Membrane potential change Membrane potential change Membrane potential Membrane potential	T4 > <i>GFP</i> T4 > <i>GluCl^aRNAi</i> T4 > <i>GFP</i> before vs. after glutamate T4 > <i>GluCl^aRNAi</i> before vs. after glutamate	$W = 0.9317$ $W = 0.8429$ $t_{25} = 6.124$ $W = 27.00$	0.0849 0.0178 2.111×10^{-6} 0.4263
2e	Two-way repeated-measures ANOVA	Input resistance	Genotype × glutamate Genotype Glutamate Cell	$F_{8, 216} = 9.743$ $F_{1, 27} = 2.263$ $F_{3,515, 94,92} = 22.57$ $F_{27, 216} = 77.93$	1.579×10^{-11} 0.1441 3.458×10^{-12} 4.295×10^{-96}
2g	Shapiro–Wilk test Shapiro–Wilk test Two-tailed Mann–Whitney <i>U</i> test	Resting membrane potential Resting membrane potential Resting membrane potential	T4 > <i>GFP</i> T4 > <i>GFP</i> , <i>GluCl^aRNAi</i> T4 > <i>GFP</i> vs. T4 > <i>GFP</i> , <i>GluCl^aRNAi</i>	$W = 0.9827$ $W = 0.9915$ $U = 2959$	0.0178 0.7673 3.404×10^{-23}
2h	Shapiro–Wilk test Shapiro–Wilk test Two-tailed Mann–Whitney <i>U</i> test	Input resistance Input resistance Input resistance	T4 > <i>GFP</i> T4 > <i>GFP</i> , <i>GluCl^aRNAi</i> T4 > <i>GFP</i> vs. T4 > <i>GFP</i> , <i>GluCl^aRNAi</i>	$W = 0.9708$ $W = 0.9677$ $U = 5979$	0.0002 0.0115 4.751×10^{-11}
5c	Shapiro–Wilk test Shapiro–Wilk test Shapiro–Wilk test Kruskal–Wallis test Dunn's multiple comparisons test	L_{dir} L_{dir} L_{dir} L_{dir} L_{dir}	T4 > <i>GFP</i> T4 > <i>GluCl^aRNAi</i> T4 > <i>Nmdar1^{RNAi}</i> T4 > <i>GFP</i> vs. T4 > <i>GluCl^aRNAi</i> T4 > <i>GFP</i> vs. T4 > <i>Nmdar1^{RNAi}</i>	$W = 0.9626$ $W = 0.8984$ $W = 0.8522$ $H = 15.27$ $Z = 3.906$ $Z = 1.318$	0.4679 0.0640 0.0391 0.0005 0.0002 0.3748
5f, ON	Shapiro–Wilk test Shapiro–Wilk test Shapiro–Wilk test Shapiro–Wilk test Shapiro–Wilk test Brown–Forsythe test One-way ANOVA Holm–Šidák's multiple comparisons test	Angular velocity Angular velocity Angular velocity Angular velocity Angular velocity Angular velocity Angular velocity Angular velocity Angular velocity	T4/T5 > <i>GluCl^aRNAi</i> T4/T5 > <i>GluCl^aRNAi</i> <i>Nmdar1^{RNAi}</i> T4/T5 > <i>Nmdar1^{RNAi}</i> T4/T5 > vs. T4/T5 > <i>GluCl^aRNAi</i> <i>GluCl^aRNAi</i> vs. T4/T5 > <i>GluCl^aRNAi</i> T4/T5 > vs. T4/T5 > <i>Nmdar1^{RNAi}</i> <i>Nmdar1^{RNAi}</i> vs. T4/T5 > <i>Nmdar1^{RNAi}</i>	$W = 0.9418$ $W = 0.9038$ $W = 0.9605$ $W = 0.9478$ $W = 0.9701$ $F_{4, 88} = 1.589$ $F_{4, 88} = 7.715$ $t_{88} = 3.000$ $t_{88} = 4.084$ $t_{88} = 1.857$ $t_{88} = 0.4669$	0.2839 0.0670 0.5536 0.3915 0.8000 0.1843 2.237×10^{-5} 0.0105 0.0004 0.1289 0.6417
5f, OFF	Shapiro–Wilk test Shapiro–Wilk test Shapiro–Wilk test Shapiro–Wilk test Shapiro–Wilk test Kruskal–Wallis test Dunn's multiple comparisons test	Angular velocity Angular velocity Angular velocity Angular velocity Angular velocity Angular velocity Angular velocity	T4/T5 > <i>GluCl^aRNAi</i> T4/T5 > <i>GluCl^aRNAi</i> <i>Nmdar1^{RNAi}</i> T4/T5 > <i>Nmdar1^{RNAi}</i> T4/T5 > vs. T4/T5 > <i>GluCl^aRNAi</i> <i>GluCl^aRNAi</i> vs. T4/T5 > <i>GluCl^aRNAi</i> T4/T5 > vs. T4/T5 > <i>Nmdar1^{RNAi}</i> <i>Nmdar1^{RNAi}</i> vs. T4/T5 > <i>Nmdar1^{RNAi}</i>	$W = 0.9258$ $W = 0.9532$ $W = 0.9039$ $W = 0.9183$ $W = 0.9251$ $H = 14.54$ $Z = 1.796$ $Z = 3.488$ $Z = 0.8056$ $Z = 0.4493$	0.0695 0.3398 0.0488 0.0920 0.1241 0.0058 0.2897 0.0019 > 0.9999 > 0.9999
5i	Shapiro–Wilk test Shapiro–Wilk test Shapiro–Wilk test Shapiro–Wilk test Shapiro–Wilk test Brown–Forsythe test Welch's ANOVA Dunnett's T3 multiple comparisons test	Fixation in front Fixation in front	T4/T5 > <i>GluCl^aRNAi</i> T4/T5 > <i>GluCl^aRNAi</i> <i>Nmdar1^{RNAi}</i> T4/T5 > <i>Nmdar1^{RNAi}</i> T4/T5 > vs. T4/T5 > <i>GluCl^aRNAi</i> <i>GluCl^aRNAi</i> vs. T4/T5 > <i>GluCl^aRNAi</i> T4/T5 > vs. T4/T5 > <i>Nmdar1^{RNAi}</i> <i>Nmdar1^{RNAi}</i> vs. T4/T5 > <i>Nmdar1^{RNAi}</i>	$W = 0.9786$ $W = 0.9274$ $W = 0.9447$ $W = 0.9611$ $W = 0.9216$ $F_{4, 72} = 5.425$ $W_{4,000, 27, 14} = 12.78$ $t_{27, 87} = 6.427$ $t_{29, 42} = 3.641$ $t_{8, 760} = 0.1015$ $t_{15, 65} = 0.6369$	0.9513 0.1751 0.2696 0.7406 0.4427 0.0007 5.645×10^{-6} 2.337×10^{-6} 0.0042 > 0.9999 0.9456

Supplementary Table 2. Statistical analyses of Extended Data Fig. 10.

Extended Data Figure	Statistical test	Measured variable	Experimental groups/comparisons	Test statistic	P
10b	Shapiro–Wilk test	Forward walking speed	T4/T5 >	W = 0.9605	0.6706
	Shapiro–Wilk test	Forward walking speed	<i>GluClα</i> ^{RNAi}	W = 0.9340	0.2280
	Shapiro–Wilk test	Forward walking speed	T4/T5 > <i>GluClα</i> ^{RNAi}	W = 0.9422	0.2403
	Shapiro–Wilk test	Forward walking speed	<i>Nmdar1</i> ^{RNAi}	W = 0.9454	0.4913
	Shapiro–Wilk test	Forward walking speed	T4/T5 > <i>Nmdar1</i> ^{RNAi}	W = 0.8049	0.0323
	Kruskal–Wallis test	Forward walking speed		H = 4.563	0.3352
10d	Shapiro–Wilk test	Forward walking speed	<i>R59E08-AD</i> ; <i>R42F06-DBD</i>	W = 0.8979	0.1743
	Shapiro–Wilk test	Forward walking speed	<i>GluClα</i> ^{RNAi}	W = 0.9520	0.5927
	Shapiro–Wilk test	Forward walking speed	<i>R59E08-AD</i> ; <i>R42F06-DBD</i> > <i>GluClα</i> ^{RNAi}	W = 0.9309	0.3139
	Brown–Forsythe test	Forward walking speed		$F_{2, 36} = 0.2397$	0.7881
	One-way ANOVA	Forward walking speed		$F_{2, 36} = 0.1688$	0.8453
10f	Shapiro–Wilk test	Fixation in front	<i>R59E08-AD</i> ; <i>R42F06-DBD</i>	W = 0.9553	0.7126
	Shapiro–Wilk test	Fixation in front	<i>GluClα</i> ^{RNAi}	W = 0.9909	0.9998
	Shapiro–Wilk test	Fixation in front	<i>R59E08-AD</i> ; <i>R42F06-DBD</i> > <i>GluClα</i> ^{RNAi}	W = 0.9768	0.9517
	Brown–Forsythe test	Fixation in front		$F_{2, 36} = 1.748$	0.1887
	One-way ANOVA	Fixation in front		$F_{2, 36} = 19.00$	2.327×10^{-6}
	Holm–Šidák’s multiple comparisons test	Fixation in front	<i>R59E08-AD</i> ; <i>R42F06-DBD</i> vs. <i>R59E08-AD</i> ; <i>R42F06-DBD</i> > <i>GluClα</i> ^{RNAi}	$t_{36} = 6.120$	9.599×10^{-7}
		<i>GluClα</i> ^{RNAi} vs. <i>R59E08-AD</i> ; <i>R42F06-DBD</i> > <i>GluClα</i> ^{RNAi}	$t_{36} = 3.523$	0.0012	

2.2 Manuscript 2: Differential temporal filtering in a small neuronal network

Abstract

In the brain, the differential temporal filtering of sensory inputs signals by neuronal networks is required for a wide range of neural computations including the detection of visual motion and sound localization. However, our understanding of how temporal filters arise in biological circuits is limited. We study the mechanism underlying signal filtering in the ON motion vision circuit of *Drosophila*, where we record the membrane potentials of the columnar Mi9, Tm3, Mi1, Mi4, and C3 neurons in response to visual stimuli *in vivo*. Together with conductance-based network modelling, these measurements demonstrate that differential filtering is independent of the neurons' intrinsic membrane properties, but emerges from the connectivity of the neuronal network comprising of feedforward and feedback connections. Specifically, we demonstrate that the temporal tuning of Mi1 depends on L1 inhibition and that mutual inhibition between Mi9 and Mi4 neurons allows for the adaptive modulation of filter time constants. This work illustrates how a small passive recurrent network creates a vast bank of temporal filters.

Authors

Jonatan G. Malis^{1,2,3}✉, Lukas N. Groschner^{1,2} & Alexander Borst²✉

¹ These authors contributed equally: **Jonatan G. Malis**, Lukas N. Groschner.

² Max Planck Institute of Neurobiology, Martinsried, Germany.

³ Graduate School of Systemic Neurosciences, LMU Munich, Martinsried, Germany.

Contributions

J.G.M., L.N.G., and A.B. conceived the study, designed experiments, and ran model simulations. **J.G.M.** and L.N.G. performed and analyzed electrophysiological recordings. The manuscript was written by **J.G.M.** and edited by all authors.

Differential temporal filtering in a small neuronal network

Jonatan G. Malis^{1,2,3}, Lukas N. Groschner^{1,2}, & Alexander Borst¹

¹Max Planck Institute of Neurobiology, Martinsried, Germany.

²These authors contributed equally: Jonatan G. Malis, Lukas N. Groschner.

³Graduate School of Systemic Neurosciences, LMU Munich, Martinsried, Germany.

e-mail: malis@neuro.mpg.de; borst@neuro.mpg.de

1 **In the brain, the differential temporal filtering of sensory inputs signals by neuronal**
2 **networks is required for a wide range of neural computations including the detection of**
3 **visual motion¹ and sound localization². However, our understanding of how temporal**
4 **filters arise in biological circuits is limited³. We study the mechanism underlying signal**
5 **filtering in the ON motion vision circuit⁴ of *Drosophila*, where we record the membrane**
6 **potentials of the columnar Mi9, Tm3, Mi1, Mi4, and C3 neurons^{5–8} in response to visual**
7 **stimuli *in vivo*. Together with conductance-based network modelling, these**
8 **measurements demonstrate that differential filtering is independent of the neurons’**
9 **intrinsic membrane properties, but emerges from the connectivity of the neuronal**
10 **network comprising feedforward and feedback connections. Specifically, we**
11 **demonstrate that the temporal tuning of Mi1 depends on L1 inhibition and that mutual**
12 **inhibition between Mi9 and Mi4 neurons allows for the adaptive modulation of filter**
13 **time constants. This work illustrates how a small passive recurrent network creates a**
14 **vast bank of temporal filters⁹.**

15
16 Differential temporal filtering of visual¹⁰, auditory¹¹, or memory-related signals^{12,13} is
17 thought to be a requirement of complex neuronal computations, such as those ascribed to the
18 cerebral cortex. However, in the cortex insights into circuit function are often limited by the
19 large number of neurons that make up each circuit, by the lack of knowledge about their
20 connectivity, and by the impracticability of recording from each node *in vivo*¹⁴. In the optic
21 lobe of *Drosophila*, none of these limitations apply. Theoretical accounts of motion vision
22 and direction selectivity rely on the differential temporal filtering of neuronal signals^{15–19}. The
23 Hassenstein–Reichardt²⁰ and the Barlow–Lewick²¹ detectors are two prominent models of
24 motion vision which define, at an algorithmic level, the computations underlying direction
25 selectivity. Both formalisms rest on a filtering stage which allows for the coincidence of
26 multiple signals measured at different points in space during visual motion²². There are hints

27 to the biological implementation of such a system in the visual system of *Drosophila*
28 *melanogaster*^{8,23}. Following a strict retinotopic organization²⁴, signals received by the retina
29 are relayed to the lamina and the medulla before they reach fourth order neurons such as the
30 direction-selective T4 cells. While each neuro-ommatidium of the compound eye captures
31 changes in light intensity, it does not compute the directionality of these changes. In the ON
32 pathway⁴, it is first in the dendrites of T4 neurons located in the tenth layer of the medulla in
33 the optic lobe, that the direction of moving light increments is computed²⁵. T4 neurons are
34 separated in four subtypes respectively responding to one of the four cardinal directions²⁵. If
35 there is an upstream filtering of the signals reaching T4 dendrites, it should be detectable at
36 the level of the membrane potentials of the input elements of T4 neurons. These inputs to T4
37 cells have been meticulously catalogued in a series of electron microscopic studies^{6,7}. Each
38 input belongs to one out of ten cell types that make for a small and compact direction
39 selective circuit, which recurs for each T4 neuron across the optic lobe (Fig. 1a and 1b) and
40 whose transmitters and receptors have been extensively characterized^{6,26}. Mi9 neurons release
41 glutamate onto the GluCl α receptor present at the distal tips of T4 dendrites²⁷. Tm3 and Mi1
42 neurons release acetylcholine at the central area, and Mi4 and C3 neurons release GABA at
43 the proximal base of T4 dendrites. It has been suggested that the computation of direction
44 selectivity in T4 neurons results from the concerted use of slow inhibitory and fast excitatory
45 inputs^{8,28}. In this constellation, inhibitory Mi9 and Mi4 inputs act as slow delay lines while
46 excitatory Tm3 and Mi1 inputs act as fast central lines (ref. ^{8,28}; Fig. 1b). Mi9 is essential to
47 the preferred direction enhancement and to the tuning of T4 neurons²³. Mi4 is thought to be
48 mediate null direction suppression seen in T4 neurons⁸. Such a model fulfils the theoretical
49 requirements of both the Hassenstein–Reichardt and the Barlow–Levick detectors.
50 Nevertheless, it has yet to be determined whether the differential temporal filtering of the
51 columnar inputs is inherited, inherent, or if it is an emerging property of the network. In the
52 mechanosensory system of *Drosophila*, differential temporal filtering has been shown to rely

53 on the band-pass filtering contingent on the cells' intrinsic membrane properties as well as on
54 the non-linearities of their voltage-gated conductances²⁹. Here, we argue that parallel channels
55 in the visual system of *Drosophila* are differentially filtered and that filter time constants
56 emerge predominantly from the architecture of the neuronal network¹². Thus, a small neural
57 circuit can create an exhaustive bank of different temporal filters necessary for computing the
58 direction of motion.

59 To investigate the temporal dynamics of the presynaptic partners of T4 neurons, we
60 systematically performed *in vivo* whole-cell current clamp recordings of each columnar input
61 to T4 neurons. The membrane potentials of GFP-labeled cells were recorded while showing
62 the fly a random noise, binary stimulus pattern at a refresh rate of at 60 Hz and with a pixel
63 size of 2.8° (Fig. 1c). From the cross-correlation of each pixel's luminance with the recorded
64 membrane potential (Fig. 1d), we determined the linear spatiotemporal receptive fields of
65 Mi9, Tm3, Mi1, Mi4, and C3 neurons (Fig. 1e). We found that temporal kernels extracted
66 from the centers of the receptive fields of Tm3 and of Mi1 neurons exhibited an undershoot
67 indicative for a band-pass filter. In contrary, those of Mi9, Mi4, and C3 neurons revealed a
68 single exponential decay, characteristic of low-pass filters. Noticeably, Mi9 cells had a
69 different polarity than the ON-sensitive Tm3, Mi1, Mi4, and C3 neurons.

70 In order to test if the different temporal kernels correspond to differential temporal filtering in
71 response to moving visual stimuli, we recorded the membrane potential of each of the five
72 columnar cell types while showing the fly gratings moving at various temporal frequencies
73 (Fig. 2a). While Tm3, Mi1, and C3 strongly modulated the amplitude of their response across
74 frequencies, Mi4 and Mi9 responded with only a weak modulation amplitude (Fig. 2a and 2c).
75 Although we categorized both Mi9 and Mi4 as similar to low-pass filters, their respective
76 response properties were different. While the membrane potential of Mi4 neurons tended to
77 exhibit sharp depolarizations followed by slow decays, the membrane potential of Mi9
78 neurons was inclined to slowly depolarize in the lead-up to a sudden, fast hyperpolarization.

79 When comparing the different tuning curves obtained in frequency space, Tm3, Mi1, and to
80 some extent C3 were tuned to frequencies above 2 Hz (Extended Data Fig. 1). Convolution of the
81 stimuli shown to the flies with the temporal kernels measured at the center of the cells'
82 receptive fields (Fig. 1e) precisely predicted the tuning in frequency space of the different cell
83 types (Fig. 2b and 2c). Presentation of 1-s full-field flashes of light to the fly also revealed the
84 differential response kinetics of each cell type (Extended Data Fig. 2a). Notably, C3 neurons
85 exhibited an undershoot at stimulus offset characteristic of band-pass filters and which was
86 not seen in its temporal kernel derived from the 60-Hz noise stimulus. Individual Mi9 cells
87 either responded with a depolarization or with a hyperpolarization to the onset of the stimulus
88 (Extended Data Fig. 2b). We attributed this variability to the strong center-surround
89 antagonism present in Mi9 neurons. A small imbalance between the strength of the center and
90 the surround of the receptive field will tip over the cell's responses towards a preference to
91 either ON or to OFF full-field stimuli. Leaving aside the possible role of the surrounds in
92 tailoring the shape of the cellular response, distinct filtering properties were clear: In response
93 to moving gratings as well as to full-field flashes, Mi4 and Mi9 neurons retained low-pass
94 filtering properties with much lower cutoff frequencies than Tm3, Mi1, and C3 neurons.
95 The specific response dynamic of a neuron is shaped, among others, by its intrinsic membrane
96 properties. The intrinsic temporal properties of individual neurons rests on two main
97 mechanisms. First, intrinsic passive membrane properties impose a low-pass filter³⁰. Second,
98 non-linearities introduced by voltage-gated ion channels can create the high-pass filters
99 necessary to generate phenomenological band-pass filters^{3,29}. In order to test if the different
100 temporal tunings of the cells are due to different intrinsic membrane properties, we recorded
101 for each cell type the input resistance and the passive membrane time constant (Fig. 3a to 3d).
102 If passive membrane properties³¹ are the foundations upon which differential filtering is built,
103 it would be expected that the passive membrane time-constants and the input resistances
104 correlate with the cells' respective temporal tuning. While further exploration of the electrical

105 compact morphology of the columnar presynaptic partners of T4 gave us reassurance to the
106 veracity of our recordings (Extended Data Fig. 3a), no such correlation was present, neither in
107 the input resistance (Fig. 3b) nor in the membrane time-constant (Fig. 3c). Therefore, the
108 temporal tuning of the fast-modulating Mi1, Tm3, and C3 neurons or of the slow-modulating
109 Mi9 and Mi4 neurons cannot be explained by differences in their passive membrane
110 properties. This finding is supported by a correlation coefficient of 0.17 between the passive
111 membrane time-constants and the time constants inferred by the membrane repolarization
112 following full-field visual stimulation of the neurons (Fig. 3d). To see if active properties of
113 the membrane lead to band-pass filtering³², we first searched for frequency bands of
114 amplified responses in each cell type. The application of current pulses of increasing
115 magnitude did not reveal any resonance or oscillation³³ indicative of a band-pass filter (ref.
116³³; Fig. 3a). Additionally, the use of a current chirp stimulus¹ unveiled in all measured cells a
117 purely low-pass filtering response of the membrane (Extended Data Fig. 3b). Further
118 exploring if band-pass filtering emerges from the nonlinearities introduced by voltage-gated
119 ion channels, we recorded currents in voltage clamp mode for each of the columnar inputs to
120 T4 (Fig. 3e to g). The fast modulating Mi1 neuron possessed two fold higher whole-cell
121 currents than the slow Mi4 and Mi9 cells (Fig. 3e and 3f). However, the amplitude of currents
122 measured in the fast Tm3 and C3 neurons were three fold smaller than those measured in Mi4
123 and Mi9 cells (Fig. 3f). Although variability between cell types was demonstrated in the
124 magnitude of whole-cell currents (Fig. 3e and 3f), this could not explain the difference in
125 temporal tuning measured in response to visual stimuli. Indeed, the differential filtering of the
126 columnar inputs to T4 dendrites was only apparent when visual stimuli were employed. In
127 summary, differential filtering of visual input signals in this circuit is not due to intrinsic
128 passive membrane properties nor is it due to nonlinearities introduced by voltage-gated ion
129 channels.

130 We hypothesized that the passive network itself was to be held responsible for a large part of
 131 the differential temporal processing in the system. Supporting the notion that the columnar
 132 inputs to T4 neurons are filtered by the recurrent architecture of the network^{9,12}, we simulated
 133 a passive neuronal circuit containing the ten neuronal classes of the direction selectivity
 134 network (Fig. 4a and 4b). Built on empirical data, our conductance model was simple and
 135 reflected the recurrent aspect of the biological circuit by incorporating all synapses identified
 136 by EM analysis. The network was defined by

$$137 \quad \frac{1}{\tau} \frac{d\bar{y}}{dt} = \mathbf{M} * \bar{y} . \quad (1)$$

138 Here, \mathbf{M} represents the connectivity matrices for histaminergic, GABAergic, cholinergic, and
 139 glutamatergic inputs (Fig. 4b) and \bar{y} is a matrix with the activity of each neuron in the model.
 140 The connection strength between cells was based on the number of synapses measured in
 141 electron microscopic studies. For each cell in the network; the leak conductance [g_{Leak}], the
 142 leak reversal potential [E_{Leak}], and a variable incorporating the cell's intrinsic membrane
 143 properties [C] were left as free parameters. Common to all cells in the network, four
 144 parameters representing the reversal potential of ACh-, histamine-, glutamate-, and GABA-
 145 induced currents were left as free parameters. The membrane potential of each cell type was
 146 calculated as

$$147 \quad \frac{dV_m}{dt} = \frac{E_{hist} * \Sigma g_{hist}(t) + E_{glu} * \Sigma g_{glu}(t) + E_{ACh} * \Sigma g_{ACh}(t) + E_{GABA} * \Sigma g_{GABA}(t) + E_{Leak} * g_{Leak} + C * V_m(t-1) + stim(t)}{\Sigma g_{hist}(t) + \Sigma g_{glu}(t) + \Sigma g_{ACh}(t) + \Sigma g_{GABA}(t) + \Sigma g_{Leak} + C} . \quad (2)$$

148 Here, g denotes the relative conductance associated with all histaminergic, glutamatergic,
 149 cholinergic, or GABAergic inputs to a neuron as well as the leak conductance, and E denotes
 150 the reversal potential of the respective currents. The model was trained using membrane
 151 potential recordings of Mi9, Tm3, Mi1, Mi4, and C3 neurons in response to a full-field visual
 152 chirp stimulus (Fig. 4c).

153 After fitting the model parameters to the measured membrane potential responses of the
 154 neurons, our biophysically realistic simulations reproduced the electrical activity of all

155 network elements (Fig. 4c). Small discrepancies of a few mV in the simulations of Mi9 and
156 Mi4 were attributed to the omission of wide-field neurons³⁴ to the model. In a next step, we
157 used our model to tease apart the individual contributions of specific synaptic connections to
158 the network's activity. *In silico*, transforming the circuit into a pure feedforward network by
159 removing all recurrent connections drastically reduced the voltage responses and unified the
160 formerly distinct filter time constants of medullary neurons (Extended Data Fig. 4). To test, in
161 a more targeted approach, if individual connections in the circuit could determine a cell's
162 response kinetics we severed *in silico* the inhibitory feedforward connection between L1 and
163 Mi1 (Fig. 5a). This slowed down the temporal tuning of Mi1 (Extended Data Fig. 5a).
164 Targeted RNA interference (RNAi) with *GluCl α* , the most highly expressed glutamate
165 receptor^{26,35} in Mi1 neurons allowed us to recreate this intervention *in vivo*. We showed chirp
166 stimuli as well as full-field flashes to the fly while recording the membrane potentials of GFP-
167 labeled and *GluCl α* RNAi-expressing Mi1 neurons (Fig. 5b and 5c). While Mi1 neurons
168 depleted of *GluCl α* retained their preference for ON stimuli, they adopted additional low-pass
169 filtering properties with a decrease in the magnitude of their impedance (ref. ³; Extended Data
170 Fig. 5b).
171 Having shown that network connectivity is necessary to maintain the fast activity of Mi1
172 neurons, we further investigated if the same principles underlie the temporal tunings of the
173 slow Mi9 and Mi4 neurons. In T4, moving visual stimuli create a delay of the signals coming
174 from two adjacent neuro-ommatidia. This delay is physically determined by the inter-
175 ommatidial angle of approximately 4.8° (ref. ^{36,37}; Fig. 6a). Hence, the speed at which visual
176 stimuli move defines the neuro-ommatidial delay. For visual motion in T4's preferred
177 direction (PD), the network-based filtering of Mi9 signals is expected to allow for the
178 coincidence of disinhibitory and of excitatory inputs onto the postsynaptic T4 neurons. For
179 motion in the null direction (ND), filtering of Mi4 signals is expected to allow for the
180 coincidence of inhibitory and of excitatory inputs (Fig. 6a). The filtering of signals in Mi9 and

181 Mi4 neurons is thus anticipated to be titrated to adjust inhibitory inputs onto T4 dendrites to
182 the velocity of the stimuli. To ensure coincidence—and hence DS—over a wide range of
183 temporal frequencies, filter time constants of Mi9 and of Mi4 neurons need to be malleable in
184 order to adjust the timing of their outputs to the velocity of the stimulus. The slow
185 depolarization and fast hyperpolarization of Mi9 membrane potential responses and,
186 conversely, the fast depolarization and slow hyperpolarization of Mi4 responses could be a
187 reflection of such an adaptive mechanism (Fig. 2a). To test if changing stimulus velocities
188 were compensated for by network-based filtering, we recorded membrane potentials of Mi9,
189 Tm3, Mi1, Mi4, and C3 neurons while showing the fly bright and dark edges moving at
190 different velocities (Fig. 6b and Extended Data Fig. 6). As a result, Mi9 was the only neuron
191 which covaried its responses with the changes in interommatidial delay. Mi4 did not adjust its
192 activity to the velocity of moving dark edges (Extended Data Fig. 7a) and retained a decaying
193 τ of 436 ± 28 ms across velocities. Models of direction selectivity predict the modulation seen
194 in Mi9 but not the lack thereof seen in Mi4. Such an uncontrollable and long-lasting inhibition
195 of T4 neurons mediated by Mi4 neurons would be detrimental in cases of the fast succession
196 between bright and dark edges found in moving gratings. Yet, in response to moving gratings,
197 Mi4 covaried the τ of its repolarization with the frequency of the stimulus (Extended Data
198 Fig. 7b). After a dark moving edge, the activity of Mi4 must therefore be differentially
199 regulated at least when the dark edge is promptly followed by a bright edge. Following the
200 notion that the temporal tuning of the neurons in this system is a product of the connectivity
201 of the circuit, we searched for a connection which would allow the modulation of Mi4 by
202 incoming bright edges. A good candidate for this modulator was Mi9 since it is the source of
203 the highest number of columnar inhibitory synapses onto Mi4 neurons, it is stemming from
204 the same column (Fig. 6c), and since it is most responsive to incoming bright edges before
205 they reach the center of its column (Fig. 6b). Conversely, Mi9 receives the majority of its
206 columnar inhibitory synapses from Mi4. This in turn makes Mi4 into an ideal candidate for

207 the sharp inhibition witnessed in Mi9 when an ON edge reaches the center of its receptive
208 field. Examination of the activity of Mi9 and Mi4 neurons aligned post hoc to make them
209 belong to the same column revealed almost perfectly mirrored responses to moving gratings
210 and to moving bright edges (Fig. 6d). *In silico*, removing these inhibitory connections
211 drastically changed Mi9's responses to static full field chirps (Extended Data Fig. 8). It is
212 expected that even if an Mi4 neuron does not adjust its time constants to the speed of moving
213 bright or dark edges, the inhibitory inputs it receives from an Mi9 adjust its responses to
214 incoming bright edges. Conversely, Mi4's inhibitory inputs onto Mi9 contribute to the fast
215 hyperpolarization of Mi9 neurons observed when a bright edge stimulates the center of their
216 receptive field (Fig. 6b). During T4 neurons' 'window of opportunity'²³, Mi9 and Mi4 are
217 thus expected to short-circuit one another thereafter hindering any unwanted inhibition onto
218 T4 neurons.

219

220 **Discussion**

221 In this study, we recorded *in vivo* the membrane potentials of Mi9, Tm3, Mi1, Mi4, and C3
222 neurons. Taking advantage of the high temporal resolution of whole-cell patch clamp
223 experiments and by standardizing the stimuli shown to the fly, we could define a
224 spatiotemporal kernel for each columnar input to T4 neurons (Fig. 1). While the pre-synaptic
225 partners to T4 could be separated based on their respective temporal tuning, each cell type
226 possessed a unique spatial-temporal receptive field identity (Fig. 1 and Fig. 2). This bank of
227 temporal filters is independent of intrinsic membrane properties (Fig. 3). We identified the
228 architecture of the passive network as the source of the measured temporal filters. We built a
229 realistic model of a microcircuit within the optic lobe that reproduced all major characteristics
230 of a direction selectivity network (Fig. 4). This model at hand, we predicted the functional
231 contributions of specific connections *in silico* and tested our predictions by removing the
232 same connections *in vivo* (Fig. 5). We identified the inhibitory connection between L1 and

233 Mi1 neurons and mediated by the GluCl α receptor as essential to the temporal tuning of Mi1.
234 Finally, we identified the mutual inhibition between Mi9 and Mi4 neurons of one column as
235 an essential modulator adjusting their activity to the velocity and to the shape of stimuli (Fig.
236 6). Because this direction selective microcircuit is repeated across the eye in a hardwired
237 fashion, there is a need for mechanisms to expand the range of T4 sensitivity across as many
238 visual inputs as possible. The engineering of a small network which allows for the emergence
239 of a large bank of temporal filters is advantageous in that it can easily be copied.

240

241 **References**

- 242 1. Llinas, R. R. The intrinsic electrophysiological properties of mammalian neurons:
243 Insights into central nervous system function. *Science* **242**, 1654–1664 (1988).
- 244 2. Jeffress, L. A. A place theory of sound localization. *Journal of comparative and*
245 *physiological psychology* **41**, 35–39 (1948).
- 246 3. Hutcheon, B. & Yarom, Y. Resonance, oscillation and the intrinsic frequency
247 preferences of neurons. *Trends Neuroscience* **23**, 216–221 (2000).
- 248 4. Joesch, M., Schnell, B., Raghu, S. V., Reiff, D. F. & Borst, A. ON and OFF pathways
249 in *Drosophila* motion vision. *Nature* **468**, 300–304 (2010).
- 250 5. Takemura, S. *et al.* A visual motion detection circuit suggested by *Drosophila*
251 connectomics. *Nature* **500**, 175–183 (2013).
- 252 6. Takemura, S. *et al.* The comprehensive connectome of a neural substrate for ‘ON’
253 motion detection in *Drosophila*. *eLife* **6**, 1–16 (2017).
- 254 7. Shinomiya, K. *et al.* Comparisons between the ON- and OFF- edge motion pathways in
255 the *Drosophila* brain. *eLife* **8**, 1–19 (2019).
- 256 8. Arenz, A. *et al.* The temporal tuning of the *Drosophila* motion detectors is determined
257 by the dynamics of their input elements. *Current Biology* **27**, 929–944 (2017).
- 258 9. Goldman, M. S. Memory without feedback in a neural network. *Neuron* **61**, 621–634

- 259 (2009).
- 260 10. Euler, T., Haverkamp, S., Schubert, T. & Baden, T. Retinal bipolar cells : elementary
261 building blocks of vision. *Nature Reviews Neuroscience* **15**, 507–519 (2014).
- 262 11. Joris, P. X., Smith, P. H. & Yin, T. C. . Coincidence detection in the auditory system.
263 *Neuron* **21**, 1235–1238 (1998).
- 264 12. Traub, R. D. & Miles, R. *Neuronal networks of the hippocampus*. (Cambridge
265 University Press, 1991).
- 266 13. Issa, J. B., Tocker, G., Hasselmo, M. E., Heys, J. G. & Dombeck, D. A. Navigating
267 through time: A spatial navigation perspective on how the brain may encode time.
268 *Annual Review of Neuroscience* **43**, 73–93 (2020).
- 269 14. Lerner, T. N., Ye, L. & Deisseroth, K. Communication in neural circuits: tools,
270 opportunities, and challenges. *Cell* **164**, 1136–1150 (2016).
- 271 15. Thorson, J. Small-signal analysis of a visual reflex in the locust. *Kybernetik* 41–53
272 (1966).
- 273 16. Poggio, T. & Reichardt, W. Visual control of orientation behaviour in the fly.
274 *Quarterly Reviews of Biophysics* **9**, 377–438 (1976).
- 275 17. Borst, A., Haag, J. & Reiff, D. F. Fly motion vision. *Annual Review of Neuroscience*
276 **33**, 49–70 (2010).
- 277 18. Strother, J. A. *et al.* The emergence of directional selectivity in the visual motion
278 pathway of *Drosophila*. *Neuron* **94**, (2017).
- 279 19. Gruntman, E., Romani, S. & Reiser, M. B. Simple integration of fast excitation and
280 offset, delayed inhibition computes directional selectivity in *Drosophila*. *Nature*
281 *Neuroscience* **21**, 250–257 (2018).
- 282 20. Hassenstein, B. & Reichardt, W. Systemtheoretische Analyse der Zeit-, Reihenfolgen-
283 und Vorzeichenauswertung bei der Bewegungspertzeption des Rüsselkäfers
284 *Chlorophanus*. *Zeitschrift für Naturforschung* **11**, 513–524 (1956).

- 285 21. Barlow, H. B. & Levick, W. R. The mechanism of directionally selective units in
286 rabbit's retina. *The Journal of Physiology* **178**, 477–504 (1965).
- 287 22. Egelhaaf, M., Borst, A., Pils, B., Kybernetik, M. & Tiibingen, E. R. G. The role of
288 GABA in detecting visual motion. *Brain Research* **509**, 156–160 (1990).
- 289 23. Groschner, L. N., Malis, J. G., Zuidinga, B. & Borst, A. A biophysical account of
290 multiplication by a single neuron. *Nature* 1–46 (2022) doi:10.1038/s41586-022-04428-
291 3.
- 292 24. Fischbach, K. F. & Dittrich, A. P. M. The optic lobe of *Drosophila melanogaster*. I. A
293 Golgi analysis of wild-type structure. *Cell and Tissue Research* **258**, 441–475 (1989).
- 294 25. Maisak, M. S. *et al.* A directional tuning map of *Drosophila* elementary motion
295 detectors. *Nature* **500**, 212–216 (2013).
- 296 26. Davis, F. P. *et al.* A genetic, genomic, and computational resource for exploring neural
297 circuit function. *eLife* **9**, (2020).
- 298 27. Fendl, S., Vieira, R. M. & Borst, A. Conditional protein tagging methods reveal highly
299 specific subcellular distribution of ion channels in motion-sensing neurons. *eLife* **9**, 1–
300 26 (2020).
- 301 28. Borst, A. A biophysical mechanism for preferred direction enhancement in fly motion
302 vision. *PLoS Computational Biology* **14**, 1–15 (2018).
- 303 29. Azevedo, A. W., Wilson, R. I., Azevedo, A. W. & Wilson, R. I. Active mechanisms of
304 vibration encoding and frequency filtering in central mechanosensory neurons. *Neuron*
305 **96**, 446–460 (2017).
- 306 30. Koch, C. *Biophysics of computation*. (Oxford University Press, 1999).
- 307 31. Agmon-snir, H. & Segev, I. Signal delay and input synchronization in passive dendritic
308 structures. *Journal of Neurophysiology* **70**, 2066–2085 (1993).
- 309 32. Gür, B., Sporar, K., Lopez-Behling, A. & Silies, M. Distinct expression of potassium
310 channels regulates visual response properties of lamina neurons in *Drosophila*

- 311 melanogaster. *Journal of Comparative Physiology* **206**, 273–287 (2020).
- 312 33. Mauro, A., Conti, F., Dodge, F. & Schor, R. Subthreshold behavior and
313 phenomenological impedance of the squid giant axon. *The Journal of General*
314 *Physiology* **55**, 497–523 (1970).
- 315 34. Tuthill, J. C., Nern, A., Rubin, G. M. & Reiser, M. B. Wide-field feedback neurons
316 dynamically tune early visual processing. *Neuron* **82**, 887–895 (2014).
- 317 35. Özel, M. N. *et al.* Neuronal diversity and convergence in a visual system
318 developmental atlas. *Nature* **589**, 88–95 (2021).
- 319 36. Land, M. F. Visual acuity in insects. *Annual Review of Entomology* **42**, 147–177
320 (1997).
- 321 37. Götz, K. G. Optomotorische Untersuchung des visuellen Systems einiger
322 Augenmutanten der Fruvhtfliege *Drosophila*. *Kybernetik* **2**, 77–92 (1964).
- 323 38. Ni, J. Q. *et al.* A genome-scale shRNA resource for transgenic RNAi in *Drosophila*.
324 *Nature Methods* **8**, 405–407 (2011).
- 325 39. Wilson, R. I., Turner, G. C. & Laurent, G. Transformation of olfactory representations
326 in the *Drosophila* antennal lobe. *Science* **303**, 366–370 (2004).
- 327 40. Schilling, T., Ali, A. H., Leonhardt, A., Borst, A. & Pujol-Martí, J. Transcriptional
328 control of morphological properties of direction-selective T4/T5 neurons in
329 *Drosophila*. *Development (Cambridge)* **146**, 1–15 (2019).
- 330 41. Gouwens, N. W. & Wilson, R. I. Signal propagation in *Drosophila*, central neurons.
331 *Journal of Neuroscience* **29**, 6239–6249 (2009).
- 332

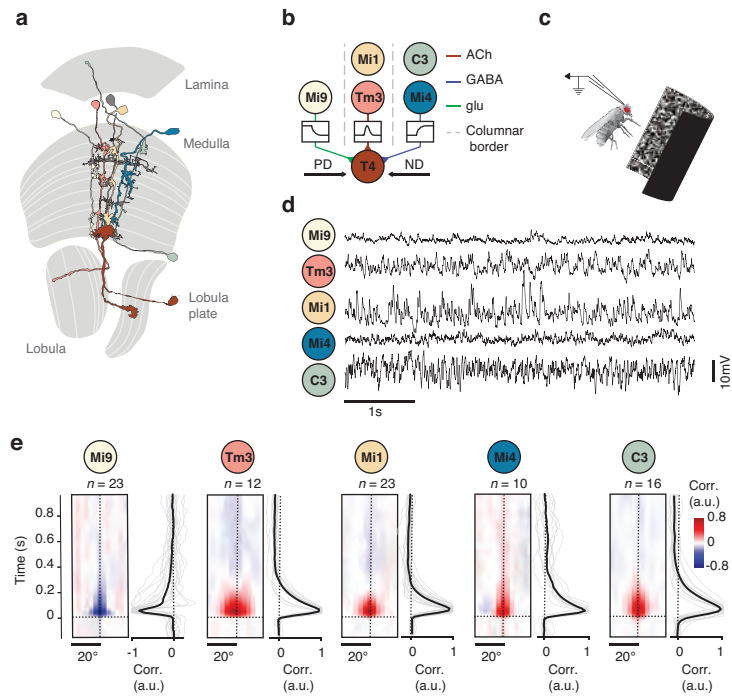


Fig. 1| Spatiotemporal receptive fields of the inputs to T4 neurons.

a, Optic lobe representation with single Mi9, Tm3, Mi1, Mi4, C3, TmY15, and T4 neurons. **b**, Circuit architecture for the ON motion detector. **c**, Targeted patch clamp recording *in vivo* during visual stimulation. **d**, Exemplary membrane potential recordings of Mi9, Tm3, Mi1, Mi4, and C3 neurons in response to visual stimulation with a white noise stimulus. **e**, Average spatiotemporal receptive field of Mi9, Tm3, Mi1, Mi4, and C3 neurons (left) with the average temporal kernel extracted from the center of each spatial receptive field (right). *n*, number of cells.

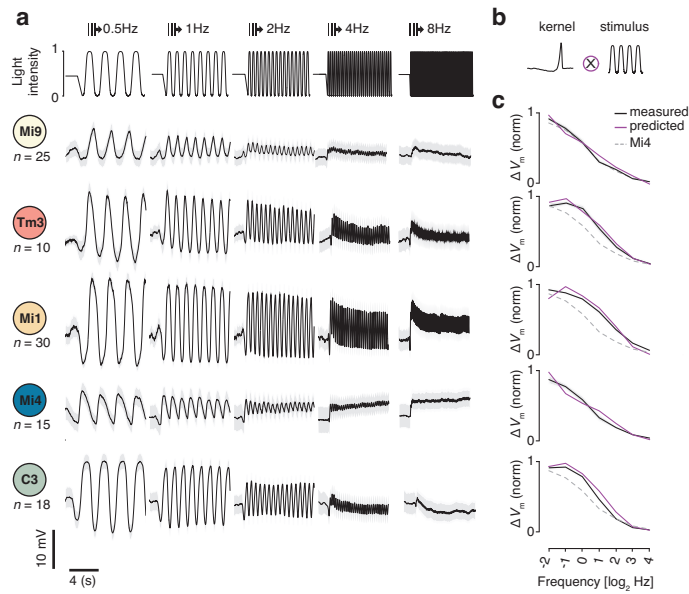


Fig. 2| Differential temporal filtering of moving gratings.

a, Membrane potentials in response to gratings moving at 0.5Hz, 1Hz, 2Hz, 4Hz, and 8Hz (top) of Mi9, Tm3, Mi1, Mi4, and C3 neurons. Membrane potentials are mean \pm s.e.m. n , number of cells. **b**, Convolution of the temporal kernel extracted at the center of the spatial receptive field of each cell type with the visual stimulus shown to the flies **c**, Temporal kernel in frequency space for each cell type in response to moving gratings (black). Kernels are mean \pm s.e.m. Prediction made from the convolution of the temporal kernels and the grating stimuli in **a** (purple). Average temporal kernel in frequency space of the slow Mi4 neuron (dashed).

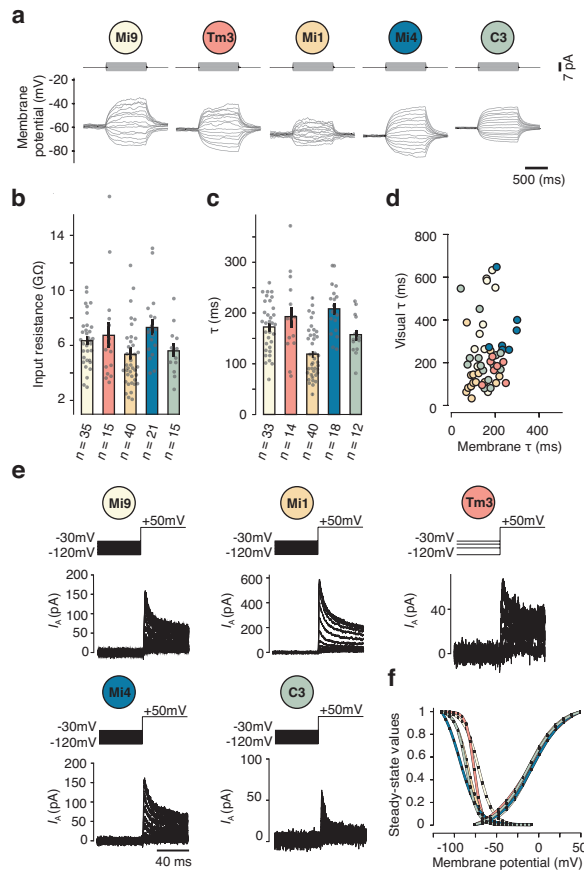


Fig. 3] Intrinsic membrane properties do not predict differential filtering.

a, Voltage responses (mV) of single Mi9, Tm3, Mi1, Mi4, and C3 neurons to steps of depolarizing current. **b**, Input resistance of each columnar input to T4 neurons. Circles, individual cells; bars, means \pm s.e.m. n , number of cells. **c**, Measured membrane time constants. Circles, individual cells; bars, means \pm s.e.m. n , number of cells. **d**, Visually evoked time constant (y-axis) plotted against membrane time constant (x-axis) for all cell types. Circles, individual cells. n , number of cells. **e**, Currents evoked by stepping each columnar input cell type from variable holding potentials (120 mV to -30 mV) to a probe potential of +50 mV. **f**, Gating of currents measured in Mi9 inactivation ($n = 26$ cells), activation ($n = 6$ cells), Tm3 inactivation ($n = 3$ cells), activation ($n = 3$ cells), Mi1 inactivation ($n = 16$ cells), activation ($n = 12$ cells), Mi4 inactivation ($n = 5$ cells), activation ($n = 5$ cells), and C3 inactivation ($n = 7$ cells), activation ($n = 4$ cells). Circles, means.

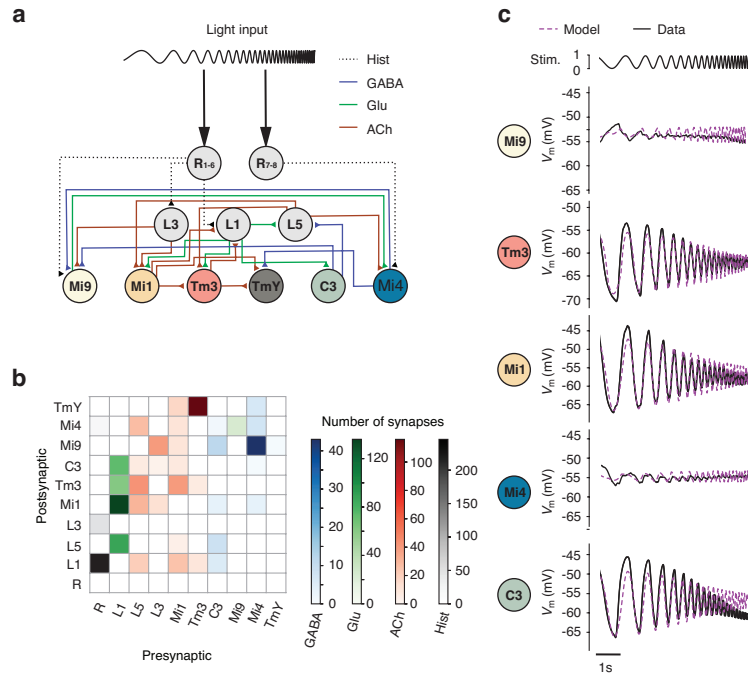


Fig. 4| Differential filtering is captured by a recurrent network model.

a, Circuit architecture for the inputs to the ON motion detector. **b**, Connectivity matrix between R, L1, L5, L3, Mi1, Tm3, C3, Mi9, Mi4, and TmY15 (TmY) neurons. Connections are color-coded based on the identity of the neurotransmitter and the number of synapses. **c**, Averaged recorded (black) and modelled membrane potentials (purple) in response to visual chirp stimuli (top) of Mi9 ($n = 7$ flies), Tm3 ($n = 7$ flies), Mi1 ($n = 8$ flies), Mi4 ($n = 4$ flies), and C3 ($n = 4$ flies) neurons.

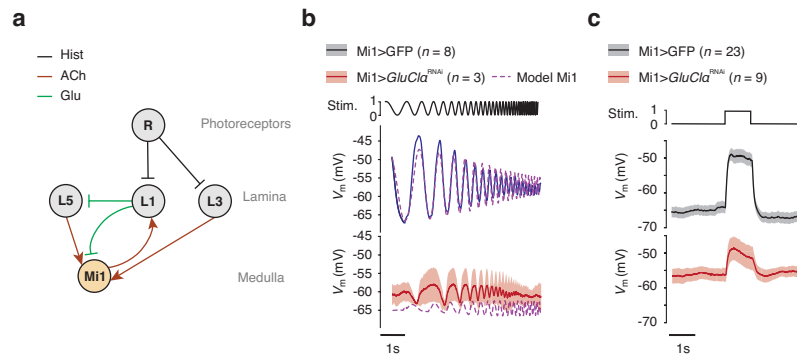


Fig. 5| L1 glutamatergic inputs allow the fast temporal tuning of Mi1.

a, Architecture of the Mi1 hyper-motif. **b**, Averaged membrane potentials recordings to visual chirp stimuli (top) Mi1>GFP ($n = 8$). Output of modelled Mi1 neurons to the same stimuli (dashed purple, top). Averaged membrane potentials recordings to visual chirp stimulation of Mi1> *GluCla*^{RNAi} (red, bottom). Membrane potentials are mean \pm s.e.m. Output of modelled Mi1 neurons without L1 input to the same stimuli (dashed purple, bottom). n , number of cells. **c**, Membrane potentials in response to ON flash stimuli (top) Mi1>GFP ($n = 23$). Membrane potentials recordings of Mi1> *GluCla*^{RNAi} (red, bottom). Membrane potentials are mean \pm s.e.m. n , number of cells.

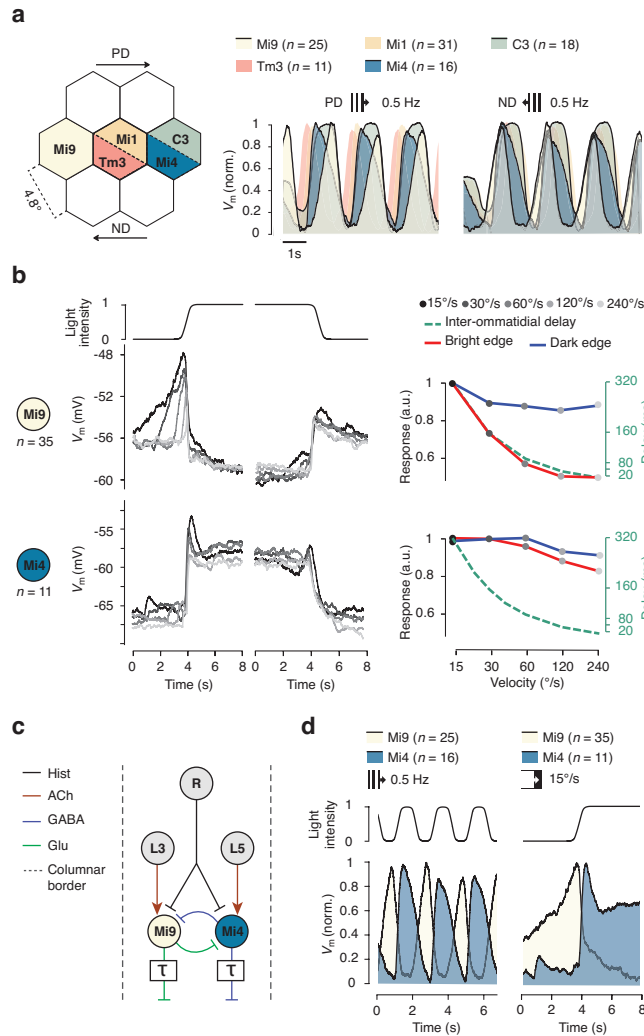


Fig. 6] Mi4 and Mi9 interconnections modulate their filtering time constants

a, Schematic of the inputs to one T4 neuron (left). Normalized membrane potentials of Mi9, Tm3, Mi1, Mi4, and C3 neurons in response to gratings moving at 0.5 Hz. Responses are time-shifted to simulate delays during visual motion in the T4 neuron's preferred (PD) and null direction (ND), respectively (right). Responses are mean and area under curve. *n*, number of cells. **b**, Time course of normalized light intensity at the receptive field centre is shown on top. Membrane potentials (mV) of Mi9 neurons (middle) or Mi4 neurons (bottom) in response to bright and dark edges (left) moving at different velocities. Integrated cellular response (right) to moving bright edges (red) and moving dark edges (blue) in comparison to the inter-ommatidial delay given at each velocity (green). *n*, number of cells. **c**, Schematic of the Mi9/Mi4 hyper-motif and of its inputs and outputs. **d**, Time course of normalized light intensity at the receptive field centre is shown on top. Average response of respectively Mi9 (white) and Mi4 (blue) neurons to gratings moving at 0.5 Hz (left) and to bright edges moving at 15°/s. Signals are normalized mean and area under curve. Signals were time-shifted to simulate visual motion in one column. *n*, number of cells.

Methods

Fly husbandry and genotypes

Flies were cultivated on a cornmeal, molasses, and yeast medium under a 12-hour light/12-hour dark cycle at 25 °C and 60% humidity. All experiments were carried out on female flies bearing at least one wild-type allele of the *white* gene. The experimenters were not blind to genotype.

Drosophila melanogaster of the following genotypes were used to target transgene expression to the respective types of neuron: $P\{R48A07-p65.AD\}attP40$, $P\{10XUAS-IVS-mCD8::GFP\}su(Hw)attP5$; $P\{VT046779-GAL4.DBD\}attP2$ was used to label Mi9 neurons, $P\{R13E12-p65.AD\}attP40/+$; $P\{R59C10-GAL4.DBD\}attP2/P\{40XUAS-IVS-mCD8::GFP\}attP2$ was used to label Tm3 neurons, $P\{R19F01-p65.AD\}attP40/+$; $P\{R71D01-GAL4.DBD\}attP2/P\{40XUAS-IVS-mCD8::GFP\}attP2$ was used to label Mi1 neurons, $P\{R48A07-p65.AD\}attP40$, $P\{10XUAS-IVS-mCD8::GFP\}su(Hw)attP5$; $P\{R13F11-GAL4.DBD\}attP2$ was used to label Mi4 neurons, $P\{R26H02-p65.AD\}attP40/+$; $P\{R29G11-GAL4.DBD\}attP2/P\{40XUAS-IVS-mCD8::GFP\}attP2$ was used to label C3 neurons, and $P\{R42F06-p65.AD\}attP40$, $P\{10XUAS-IVS-mCD8::GFP\}su(Hw)attP5$. In electrophysiological experiments, $P\{TRiP.HMC03585\}attP40/P\{R19F01-p65.AD\}attP40$, $P\{10XUAS-IVS-mCD8::GFP\}su(Hw)attP5/P\{R71D01-GAL4.DBD\}attP2/+$ (abbreviated Mi1 > *GluCl*^{RNAi}) was used to silence expression of *GluCl*³⁸.

All flies, including parental controls, were heterozygous for the respective transgenes.

With the exception of the strain used to label C3 (a gift from A. Nern and M. Reiser), all flies were obtained from the Bloomington *Drosophila* Stock Center (BDSC).

Patch clamp recordings

For whole-cell recordings *in vivo*^{39,40}, female flies aged 2-24 hours post-eclosion were cold-anaesthetized and fixed to a custom, laser-cut polyoxymethylene mount with soft thermoplastic wax (Agar Scientific). The preparation was submerged in extracellular solution

(pH 7.3) containing 5 mM TES, 103 mM NaCl, 3 mM KCl, 26 mM NaHCO₃, 1 mM NaH₂PO₄, 1.5 mM CaCl₂, 4 mM MgCl₂, 10 mM trehalose, 10 mM glucose, and 7 mM sucrose (280 mOsm, equilibrated with 5% CO₂ and 95% O₂). Cuticle, adipose tissue, and trachea were surgically removed in a window large enough to expose the left dorsal optic lobe. Patch pipettes (15-20 MΩ) were fabricated from borosilicate glass capillaries with outer and inner diameters of 1.5 and 1.17 or 0.86 mm, respectively, using a P-97 (Sutter Instruments) or a PC-10 (Narishige) micropipette puller. Pipettes were polished using a microforge (MF-830, Narishige) and filled with solution (pH 7.3) containing 10 mM HEPES, 140 mM potassium aspartate, 1 mM KCl, 4 mM MgATP, 0.5 mM Na₃GTP, 1 mM EGTA, and 10 mM biocytin (265 mOsm). Green-fluorescent somata were targeted visually using a combination of bright-field and epifluorescence microscopy on an InVivo SliceScope (Scientifica) or an Axio Scope.A1 microscope (Zeiss), each equipped with a 60×, 1.0 NA water immersion objective (LUMPLFLN60XW, Olympus) and an LQ-HXP 120 light source (Leistungselektronik Jena). Transillumination was achieved by butt-coupling a white LED (MCWHD5, Thorlabs) to a liquid light guide whose far end was positioned caudally at a distance of 1 cm to the fly allowing for an unobstructed field of view. To gain access to cell membranes, a micropipette was used to make a small incision in the perineural sheath. Signals were recorded at room temperature (21-23 °C) with a MultiClamp 700B amplifier, lowpass-filtered, and sampled at 10 kHz using a Digidata 1550B digitizer controlled through pCLAMP 11 software (all from Molecular Devices). Data were corrected for the liquid junction potential and analysed with custom-written software in Python 3.7 (Python Software Foundation) using NumPy 1.15, Pandas 0.24, SciPy 1.3, Matplotlib 3.0, and pyABF 2.1 (<https://pypi.org/project/pyabf/>). After temporal alignment, current clamp data were analysed at a sampling rate of 1 kHz. The most negative membrane potential recorded within 2 min after break-in, in darkness, and in the absence of a holding current, was taken to represent the resting potential. Only cells with a measured resting potential more negative than -25 mV

were characterized further. Input resistances, as plotted in Fig. 3, were calculated based on linear fits to the steady-state voltage changes elicited by 1-s steps of hyperpolarizing currents (1-pA increments, starting at -5 pA). Membrane time constants were determined by fitting a single exponential to the voltage deflection caused by a hyperpolarizing currents (1-pA increments, starting at -5 pA). Visually evoked time constants were determined by fitting a single exponential to the repolarization of the neurons following full-field flash stimuli. Correlation coefficient was calculated using the `corrcoef` function of the Numpy 1.21.2 module. In voltage-clamp recordings, steady-state activation parameters were determined by applying depolarizing 50 ms voltage pulses from a holding potential of -100 mV; the pulses covered the range to $+50$ mV in steps of 10 mV. Steady-state inactivation parameters were obtained with the help of a two-pulse protocol, in which a 500 ms pre-pulse (-120 to -30 mV in 5 mV increments) was followed by a 50 ms test pulse to $+50$ mV; non-inactivating outward currents, measured from a pre-pulse potential of -30 mV, were subtracted. Peak A-type currents (I_A) were normalized to the maximum current amplitude (I_{max}) of the respective cell and plotted against the pre-pulse potential (V).

Visual stimulation in electrophysiological experiments

Visual stimuli were projected, via two mirrors, onto a cylindrical screen using two DLP Lightcrafter 3000 pico projectors (Texas Instruments) as previously described⁸. The screen covered 180° in azimuth and 105° in elevation of the fly's left frontal visual field and doubled as a Faraday shield. Restricting the projectors to the green channel (500-600 nm) allowed for a refresh rate of 180 Hz at 8-bit colour depth and a maximal luminance of 1274 cd/m². The average luminance of stimuli, which were presented in full contrast, was set to an 8-bit greyscale value of 128 corresponding to an average luminance of ~ 637 cd/m². Stimuli were created and pre-distorted to account for the curvature of the screen using the Panda3D game engine in Python 2.7.

Receptive fields were located and characterized using a binary white noise stimulus with a pixel size of $2.8^\circ \times 2.8^\circ$. Samples were drawn at a rate of 60 Hz and projected onto the screen for durations ranging from three up to 20 min. Stimuli and simultaneously recorded membrane potentials were time-locked using a continuously recorded trigger signal on the screen. Stimulus files were exported after lossless compression and cross-correlated to each neuron's recorded membrane voltage using standard techniques for reverse correlation in Python 3.7. Slow voltage drifts were corrected post hoc by subtracting a low-pass filtered version of the signal obtained using a Gaussian blur with a standard deviation of 60 seconds. The reverse correlation was calculated as

$$K(x, \tau) = \int_0^T dt S(x, t - \tau) \cdot V_m(t) ;$$

Where V_m denotes the neuron's baseline-subtracted membrane voltage at time point t and S denotes the stimulus at position x and time point $t - \tau$ for values of τ ranging from -0.5 to $+3.0$ s. The resulting spatiotemporal receptive fields were converted into standard scores. Only neurons with clear standard score peaks (typically > 4 standard deviations from the mean) and with receptive field centres > 8 pixels (22.48°) from the bezel of the screen were included in the analysis to guarantee full coverage of the surround. Receptive fields were normalized and aligned in space using the extremum (i.e. the maximum or minimum with the highest absolute value) of the standard score as a point of reference, which was placed at 0° . After cropping the individual spatial receptive fields to the largest common region holding data from all neurons, scores were averaged across neurons of one class.

Temporal frequency tuning curves were measured using gratings of the above properties at temporal frequencies ranging from 0.25 to 64.0 Hz. ΔV_m was defined as the difference between maximal and minimal membrane potential. Impedance was calculated by dividing the fast Fourier transform of the minimum-maximum normalized membrane potentials by the fast Fourier transform of the minimum-maximum normalized chirp stimulus.

For experiments in Fig. 6, bright (ON) and dark (OFF) edges were moved across the screen at a velocity from 15°/s to 240°/s. The responses of individual neurons of one type were temporally aligned based on the cross-correlation maximum between the time derivative of the low-pass filtered membrane potential of each neuron and that of one hand-picked template neuron in response to ON edges. The responses of different input neuron classes were aligned based on the relative distances of the template neurons' receptive field centres on the screen. Correct alignment was verified by recording light intensities from a 5°-wide area of the screen located at the respective template neuron's receptive field centre using a custom-built photodiode under identical stimulus conditions.

Multi-compartment model

We built a passive compartmental model of Mi9, Tm3, Mi1, Mi4, and C3 neurons respectively (Supplementary Fig. 3) to account for possible space-clamp problems due to neuronal morphology in voltage clamp experiments and to assess signal propagation between dendrite and soma. The models were based on an electron microscopic reconstruction ⁷ (http://neuromorpho.org/neuron_info.jsp?neuron_name=Mi9-Q_179, http://neuromorpho.org/neuron_info.jsp?neuron_name=Tm3-C-post_172, http://neuromorpho.org/neuron_info.jsp?neuron_name=Mi1_Home_212, http://neuromorpho.org/neuron_info.jsp?neuron_name=97, and http://neuromorpho.org/neuron_info.jsp?neuron_name=18274) and all comprised 2,012 compartments. For each reconstruction, a connectivity matrix, which held values of one where two compartments were connected and values of zero otherwise, served as a template to calculate a conductance matrix M . The latter was based on the three-dimensional coordinates and the length as well as the diameter of each compartment assuming, unless stated otherwise, an axial resistivity (R_a) of 150 Ωcm , a membrane resistance (R_m) of 28 $\text{k}\Omega\text{cm}^2$, and a specific membrane capacitance (C_m) of 1 $\mu\text{F}/\text{cm}^2$. All parameters were on the same scale as those commonly used to model *Drosophila* neurons ⁴¹ and were considered to

be uniform across the entire cell. Varying R_a and R_m over a biophysically plausible range had negligible effects on model output (Extended Data Fig. 3a).

The voltage vector $V_m(t)$ indicating the membrane potential of each compartment and at each time point t was determined by using the `sparse.linalg.spsolve` function of the SciPy 1.3 module to iteratively solve the matrix equation $M \times V_m(t) = V_m(t-1) \times c_m / \Delta t + E_{\text{leak}} \times g_{\text{leak}} + I(t)$; where $V_m(t-1)$ denotes the voltage vector at the previous time point, c_m is the vector holding the specific capacitances of all compartments, Δt denotes the time step, E_{leak} denotes the leak reversal potential, g_{leak} denotes the vector holding the specific transmembrane leak conductances of all compartments, and $I(t)$ is the vector indicating the current injected at time point t into each compartment. Simulations were performed with a fixed Δt of 0.1 ms. If only steady-state was considered, the diagonal of the conductance matrix M held no capacitive conductances and the right-hand side of the equation simplified to $E_{\text{leak}} \times g_{\text{leak}} + I(t)$. At the time of transmitter application, synaptic conductances were added both to the diagonal of the conductance matrix and, multiplied by the reversal potential of the current, to the right-hand side of the equation.

To simulate voltage clamp, the current injected at the soma was calculated based on the difference between the chosen command voltage V_{cmd} and the actual potential at the soma $V_{m,\text{soma}}$ using a proportional-integral control loop that served to emulate a voltage clamp amplifier in Python 3.7. The current to be injected at time point t was calculated as $I(t) = K_p \times (V_{\text{cmd}}(t) - V_{m,\text{soma}}(t)) + K_i \times I(t-1)$; where K_p denotes the proportional gain and K_i the integral gain. With values of 2×10^9 and 1 for K_p and K_i , respectively, $V_{m,\text{soma}}$ could be clamped reliably at the desired V_{cmd} under all conditions and synaptic inputs.

Single-compartment model

Recorded membrane voltages of Mi9, Tm3, Mi1, Mi4, and C3 were averaged. EM connectivity data was separated into four matrices corresponding to the identity of the neurotransmitter released by the neurons (histamine, glutamate, ACh, and GABA). For each

neuron in the model, the membrane potentials of its inputs were transformed into conductances. The gain of each conductance was determined by the minimum-maximum normalized number of synapses received by each neuron. The network was defined as

$$\frac{1}{\tau} \frac{d\bar{y}}{dt} = \mathbf{M} * \bar{y}.$$

Here, \mathbf{M} represents the connectivity matrix for histaminergic, GABAergic, cholinergic, and glutamatergic inputs and \bar{y} is the matrix of the activity of each cell in the model.

The membrane potential of each neuron was calculated as

$$\frac{dV_m}{dt} = \frac{E_{\text{hist}} * \Sigma g_{\text{hist}}(t) + E_{\text{glu}} * \Sigma g_{\text{glu}}(t) + E_{\text{ACh}} * \Sigma g_{\text{ACh}}(t) + E_{\text{GABA}} * \Sigma g_{\text{GABA}}(t) + E_{\text{Leak}} * g_{\text{Leak}} + C * V_m(t-1) + \text{stim}(t)}{\Sigma g_{\text{hist}}(t) + \Sigma g_{\text{glu}}(t) + \Sigma g_{\text{ACh}}(t) + \Sigma g_{\text{GABA}}(t) + \Sigma g_{\text{Leak}} + C},$$

where g denotes the relative conductance associated with each input neuron and E denotes the reversal potential of the respective current with $E_{\text{hist}} = -64$ mV, $E_{\text{Glu}} = -74$ mV, $E_{\text{ACh}} = -48$ mV, and $E_{\text{GABA}} = -97$ mV. At time point (t), conductances g_{hist} , g_{glu} , g_{ACh} , and g_{GABA} for one neuron were defined by the minimum-maximum normalization of the membrane potentials of its cellular inputs at time point ($t-1$). The compact size of all neurons of the circuit eliminated the need for a differential equation to calculate V_m . Free parameters (C , E_{hist} , E_{glu} , E_{GABA} , E_{ACh} , E_{leak} , and g_{leak}) were estimated from a least-squares fit to measured membrane voltage traces of Mi9, Tm3, Mi1, Mi4, and C3 neurons, computed with the help of the optimize.minimize function of the SciPy 1.3 module. Upper and lower bounds for parameter values were set to 0 and 10 for C , -100 mV and 0 mV for E_{hist} , E_{glu} , E_{GABA} , E_{ACh} , E_{leak} respectively, and 0 and 1 for g_{leak} , respectively. The parameters used for simulations shown in Figs. 4c, 6b, and Extended Data Figs. 4, 5, and 8: $R_{E_{\text{leak}}} = -68$ mV, $L1_{E_{\text{leak}}} = -8$ mV, $L3_{E_{\text{leak}}} = -67$ mV, $L5_{E_{\text{leak}}} = -64$ mV, $Mi9_{E_{\text{leak}}} = -41$ mV, $Tm3_{E_{\text{leak}}} = -81$ mV, $Mi1_{E_{\text{leak}}} = -100$ mV, $Mi4_{E_{\text{leak}}} = -10$ mV, $Mi4_{E_{\text{leak}}} = -31$ mV, $C3_{E_{\text{leak}}} = -70$ mV, $TmY_{E_{\text{leak}}} = 0$ mV, $R_{g_{\text{leak}}} = 1.0$, $L1_{g_{\text{leak}}} = 0.3$, $L3_{g_{\text{leak}}} = 0.2$, $L5_{g_{\text{leak}}} = 1.0$, $Mi9_{g_{\text{leak}}} = 1.0$, $Tm3_{g_{\text{leak}}} = 0.0$, $Mi1_{g_{\text{leak}}} = 0.0$, $Mi4_{g_{\text{leak}}} = 0.0$, $C3_{g_{\text{leak}}} = 0.0$, $TmY_{g_{\text{leak}}} = 1.0$, $R_C = 0.8$, $L1_C = 0.6$, $L3_C = 0.8$, $L5_C = 0.2$, $Mi9_C = 0.6$, $Tm3_C = 10$, $Mi1_C = 3.3$, $Mi4_C = 1.0$, $C3_C = 3.6$, and $TmY_C = 0.6$.

All simulations were written in Python 3.7

Statistics and reproducibility

No sample size calculations were performed prior to experimentation. Sample sizes were chosen to match or exceed standard sample sizes in the field. Sample sizes in electrophysiological experiments correspond to the number of cells, each of which was recorded in a different animal. The investigators were not blind to genotype. Randomization was not applicable, because flies were grouped based on genotype.

Acknowledgments

We thank A. Nern, M. Reiser, G. Rubin, L. Luo, and T. Schilling for flies, M. Drews for software. This work was supported by the Max Planck Society, an EMBO Long-Term Fellowship ALTF 365-2019 to L.N.G., and by the European Union's Horizon 2020 programme under the Marie Skłodowska-Curie Action MOVIS grant agreement No 896143 to L.N.G. Flies obtained from the Bloomington *Drosophila* Stock Center (NIH P40OD018537) were used in this study. J.G.M is a member of the graduate School of Systemic Neurosciences, LMU Munich, Martinsried, Germany

Author contributions

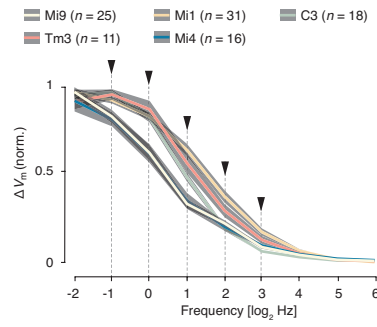
J.G.M., L.N.G., and A.B. conceived the study, designed experiments, and ran model simulations. J.G.M. and L.N.G. performed and analysed electrophysiological recordings. The manuscript was written by J.G.M. and edited by all authors.

Competing interests

The authors declare no competing interests.

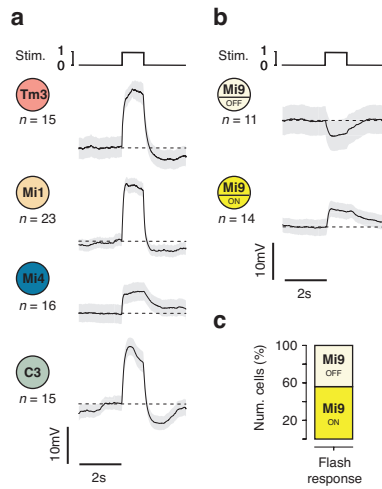
Additional information

Correspondence and requests for materials should be addressed to J.G.M. or A.B.

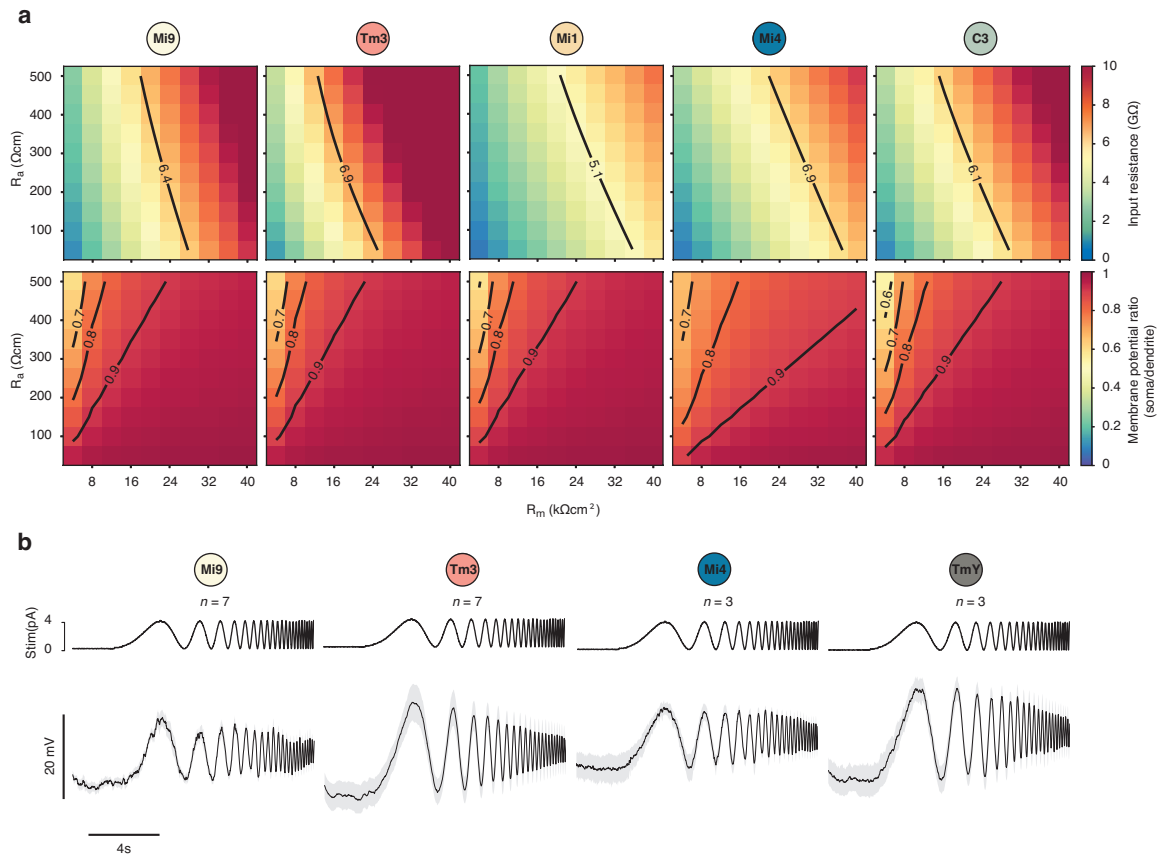


Extended Data Fig. 1 | Differential filtering of moving gratings.

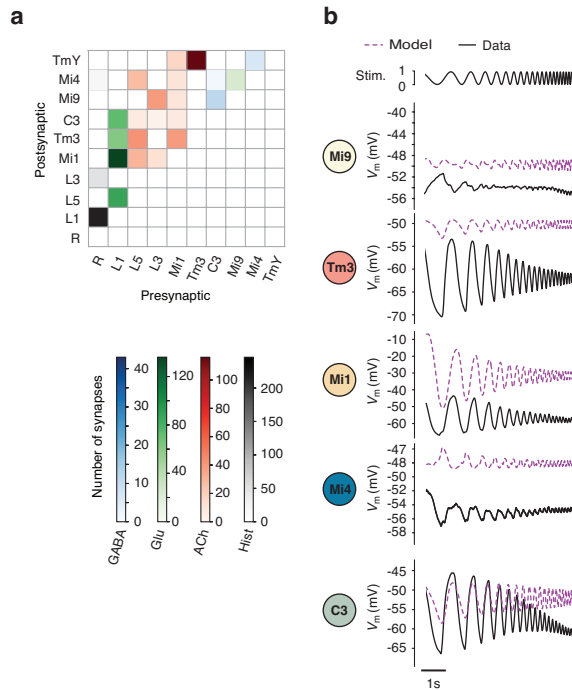
Frequency responses of Mi9, Tm3, Mi1, Mi4, and C3 neurons to moving gratings. Traces are mean \pm s.e.m. Arrows and dotted lines denote frequencies at which differential temporal tuning is visible. *n*, number of cells.



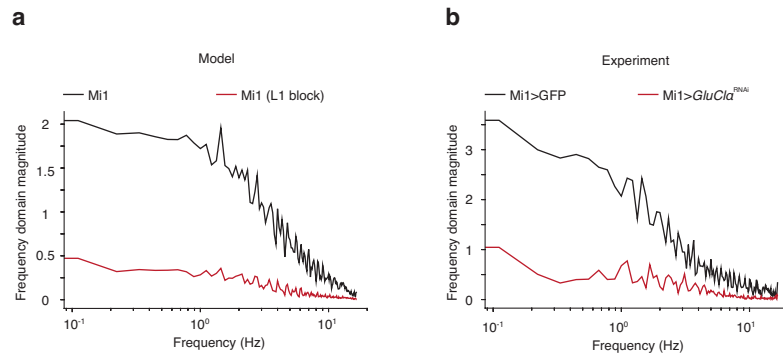
Extended Data Fig. 2|Full field flash responses. **a**, Membrane potentials in response to 1-s full-field flashes (top) of Tm3, Mi1, Mi4, and C3 neurons. Membrane potentials are mean \pm s.e.m. n , number of cells. **b**, Membrane potentials in response to 1-s full-field flashes of Mi9 neurons responding with a hyperpolarization (Mi9^{OFF}, top) or a depolarization (Mi9^{ON}, bottom) to ON full-field flashes. **c**, Percentage of recorded Mi9 cells which responded to ON full-field flashes with a hyperpolarization (Mi9^{OFF}, top) or with a depolarization (Mi9^{ON}, bottom).



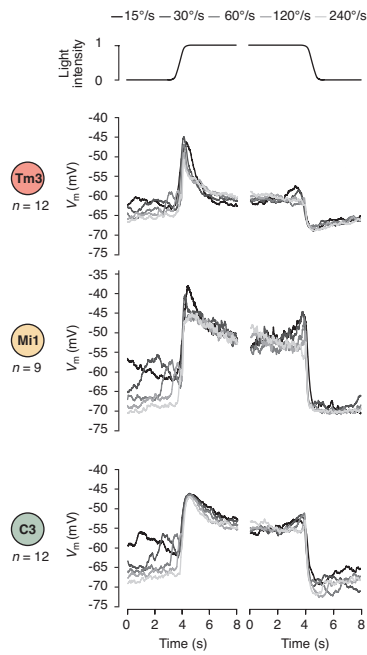
Extended Data Fig. 3 | Electrical morphology of each cell type. a, Modelled somatic input resistance as a function of the axial resistivity (R_a) and of the membrane resistance (R_m). Solid lines correspond to the measured mean input resistance for wild-type Mi9, Tm3, Mi1, Mi4, and C3 neurons (as shown in Fig. 3). Ratio of somatic to dendritic membrane potential in response to dendritic injection of 10 pA of depolarizing current as a function of membrane resistance (R_m) and axial resistivity (R_a) in the model (bottom). Note that for all cells soma and dendrite were quasi-isopotential (ratio > 0.9) across a wide range of parameters. **b**, Membrane potentials in response to current chirp injections for Mi9, Tm3, Mi1, and TmY15 (TmY) neurons. Membrane potentials are mean \pm s.e.m. n , number of cells.



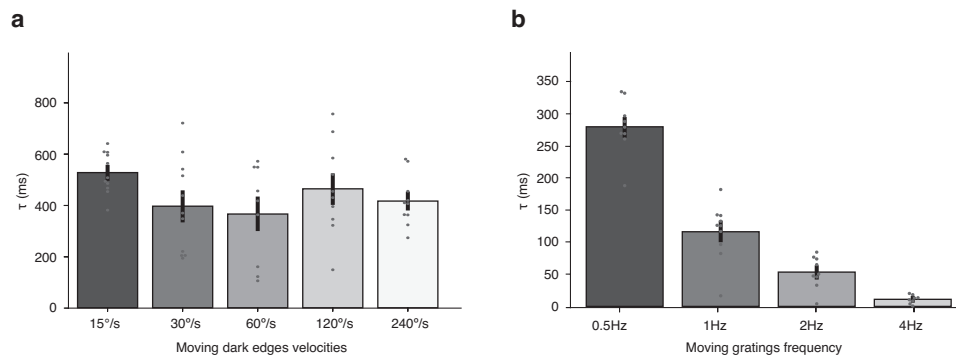
Extended Data Fig. 4 | Recurrent connections are essential to differential filtering. **a**, Connectivity matrix between R, L1, L5, L3, Mi1, Tm3, C3, Mi9, Mi4, and TmY15 neurons in a pure feedforward network. Connections are color-coded based on the identity of the neurotransmitter used and the number of synapses. **b**, Averaged membrane potential recordings in response to visual chirp stimuli (top, black) of Mi9 ($n = 7$ flies), Tm3 ($n = 7$ flies), Mi1 ($n = 8$ flies), Mi4 ($n = 4$ flies), and C3 ($n = 4$ flies). Output of modelled Mi9, Tm3, Mi1, C3, and Mi4 neurons to the same stimuli when the direction selective circuit has a strictly feedforward connectivity (purple).



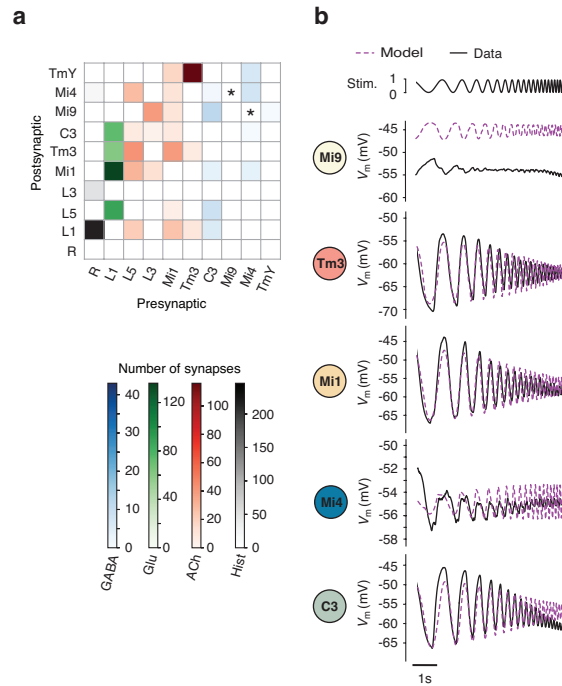
Extended Data Fig. 5| L1 accelerate Mi1. **a**, Impedance of modelled Mi1 neuron in response to visual chirps with L1 input (black) and without input from L1 (red). **b**, Impedance of mean recorded Mi1>GFP neurons (black) and of mean recorded Mi1> *GluCla*^{RNAi} neurons (red) in response to visual chirps.



Extended Data Fig. 6 | Responses to moving bright and dark edges. Time course of normalized light intensity at the receptive field center is shown on top. Membrane potentials of Tm3, Mi1, and C3 neurons respectively in response to ON (left) and OFF edges (right) moving at 15, 30, 60, 120, and 240°/s. *n*, number of cells.



Extended Data Fig. 7 | Time constants of Mi4 in response to moving gratings. **a**, Measured time constants of Mi4 membrane potential responses to dark edges moving at 15°/s ($n = 11$ flies), 30°/s ($n = 11$ cells), 60°/s ($n = 9$ cells), 120°/s ($n = 10$ cells), and 240°/s ($n = 10$ cells), respectively. Circles, individual cells; bars, means \pm s.e.m. **b**, Measured time constants of Mi4 membrane potential responses ($n = 10$ cells) to gratings moving at 0.5Hz, 1Hz, 2Hz, and 4Hz, respectively. Circles, individual cells; bars, means \pm s.e.m.



Extended Data Fig. 8 | Direction selective circuit without Mi9/Mi4 feedback loop. a, Connectivity matrix between R, L1, L5, L3, Mi1, Tm3, C3, Mi9, Mi4, and TmY15 neurons in a network lacking the Mi9/Mi4 interconnections. Pathways are color-coded based on the identity of the neurotransmitter used and the number of synapses for each connection. Asterisks denote connections which were removed. **b**, Membrane potential recordings in response to visual chirp stimuli (top, black) of Mi9 ($n = 7$ flies), Tm3 ($n = 7$ flies), Mi1 ($n = 8$ flies), Mi4 ($n = 4$ flies), and C3 ($n = 4$ flies). Output of modelled Mi9, Tm3, Mi1, C3, and Mi4 neurons to the same stimuli when the Mi9/Mi4 interconnection are removed (purple).

DISCUSSION

As I started my doctoral work, motion vision in *Drosophila melanogaster* was mainly studied by calcium imaging. These studies have undeniably led to a leap in the understanding of motion vision in the fly (Arenz et al., 2017; Clark et al., 2011; Haag et al., 2016, 2017; Maisak et al., 2013). However, *genetically encoded calcium indicators* (GECI) can only provide a limited insight into the biophysical properties leading to direction selectivity in the optic lobe. GECI neither reflect the hyperpolarization of the membrane, nor do they reveal the currents in cells. Furthermore, GECI cannot be used to measure the input resistance of neurons. In this thesis, I describe how my co-authors and I could – with electrophysiological recordings of T4 neurons and of its inputs – unravel biophysical mechanisms of direction selectivity in the fly, how we could build realistic models of these mechanisms, and how these findings are a starting point in the reconciliation between theories of signal processing in complex networks and experimental neurophysiology.

3.1 Mechanisms of direction selectivity in T4 cells

Our understanding of the computations underlying the ability to sense visual motion is guided by mechanistic models of motion vision. Correlation-type motion detectors compute the direction of motion using the coincidence of light inputs followed by the performance of nonlinear operational arithmetic (Barlow and Levick, 1965; Hassenstein and Reichardt, 1956). This coincidence of signals is possible through filtering mechanisms such as the ones seen in the presynaptic columnar partners to T4 neurons. The signal filtering implemented upstream of T4 neurons is thus a necessary part of the computation of the direction of motion.

3.1.1 Differential filtering of input signals to T4

Many studies looking at the origins of differential temporal filtering focus on the intrinsic temporal filtering properties of single neurons (Azevedo et al., 2017; Hutcheon and Yarom, 2000; Llinas, 1988). In such a constellation, rhythms seen in the brain are understood as emerging from the temporal properties of **individual** neurons. They have therefore been experimentally studied in the context of 1) the intrinsic passive properties of their membrane and 2) the patterns of expression of voltage-gated ion channels in their membrane (Section 1.2 of this thesis). Together, passive membrane properties and voltage-gated ion channels can dictate the level of

filtering implemented by a single neuron. This approach undeniably illustrates real filtering properties single neurons can have (Smotherman and Narins, 1999) but it ignores the temporal properties emerging from the architecture of neuronal networks.

Less experimentally studied, is the role of **networks of neurons** in the creation of temporal filters. This is not without reason. It is extremely difficult to biophysically study every node of a complex neuronal network. In the cortex, the prediction of the evolution of electrical potentials is made difficult by the size of neurons, the number of inputs they receive, and by the nonlinearities introduced by their voltage-gated ion channels (Lerner et al., 2016). Added to this, if the architecture of the network itself is one of the key mechanisms to temporally process signals, the state of the brain where neuronal activity is measured might have a crucial impact on cellular activity. Experiments performed *ex vivo* or *in vivo* – but under anesthesia (Pisokas et al., 2022) – might reveal cellular activity specific to the state the brain is forced into. For these reasons, the study of **network-based filtering** in complex neuronal circuits has mostly been theoretical and explored via model simulations. These simulations often involve ‘**point neurons**’ where each neuron is represented as an isopotential unit (Traub and Miles, 1991; Tzilivaki et al., 2019).

The motion vision circuit of *Drosophila melanogaster* can be more thoroughly explored than circuits found in the retina or in the cortex (Borst and Helmstaedter, 2015). The direction-selective circuit is relatively small, it is very stereotyped, a plethora of genetic tools is available (Chalfie et al., 1994), and much is already known about connectivity patterns between neurons (Davis et al., 2020; Shinomiya et al., 2019; Takemura et al., 2017). Furthermore, as we show in **manuscripts 1 and 2**, many of the cells involved in this network possess electrically compact morphologies which make them phenomenologically close to point neurons. These factors make the direction-selective circuit optimal to study **network-based filtering**. It further allows to bridge signal processing in complex networks with the biophysical dissection of neuronal networks in the brain.

In **manuscript 2**, we explore the origins of the differential filtering of Mi9, Tm3, Mi1, Mi4, and C3 neurons. We find that differential filtering seen in the inputs to T4 neurons is not an intrinsic property of each cell type. It is rather dictated by the architecture of the network. We further show that the differential expression of voltage-gated ion channels across the different cell types is not a decisive factor in

the implementation of differential temporal filtering. In our passive conductance model, we found that the differential temporal filtering of the columnar inputs to T4 neurons is reduced when the network is transformed into a pure feedforward network. We attribute the reduction to the direction-selective circuit's reliance on directed feedforward networks, feedback loop network motifs, and on feedforward loop network motifs. The use of network motifs as a filtering strategy is further discussed in 3.3.

Most of the recent studies which have explored differential temporal filtering in the optic lobe use so-called temporal kernels. These kernels result from the reverse correlation of signals acquired when presenting the fly with a noisy visual stimulus (Arenz et al., 2017; Behnia et al., 2014; Drews et al., 2020; Kohn et al., 2021). This way, each cell type is assigned a temporal kernel measured at the center of its receptive field. However, can a neuron's response to white noise stimuli predict its response to moving gratings or its response to moving edges?

The answer to this question is both “yes” and “no”. While some features of a neuron's response can be captured by white noise stimuli (Fig. 2b of manuscript 2), many others are still missing. In **manuscript 2**, contradictory pictures of the temporal properties of neurons are revealed. Sometimes, cells of one neuronal type respond as band-pass filters, while at other times they respond as low-pass filters. Response as a low-pass filter or as a band-pass filter is dependent on what visual stimulus is shown to the fly. For instance, in response to moving gratings and to visual chirp stimuli, C3 neurons behave as low-pass filters. In response to full-field flashes and to light flickers at the center of their receptive field, they respond as band-pass filters. Here, the variability of the temporal properties exhibited by a cell type is explained by the architecture of the circuit. Hence, the variability seen in the time constants of C3 neurons is a direct reflection of how temporal filtering properties can be dependent on a network's architecture.

Network-based filtering also explains how a recent study could find variability in the temporal properties of the inputs to T5 neurons (the equivalent of T4 neurons in the OFF pathway) in response to various visual stimuli (Kohn et al., 2021). Indeed, if the filtering of the inputs to T5 neurons is also mostly based on complex network architecture, then, it is to be expected that a cell's temporal filtering will change depending on the stimulus presented to the fly. This is an example of how a

hardwired microcircuit is able to expand the range of responses of a neuron across a battery of different visual stimuli.

3.1.2 Multiplication-like arithmetic on T4 dendrites

In 1.3.3, multiple strategies which neurons can use in order to implement multiplicative arithmetic are described. However, the multiplication that my co-authors and I find in T4 neurons is peculiar since it is free from the voltage dependence which limit threshold-based systems (Srinivasan and Bernard, 1976) and since it is not limited by the amplitude of the input signals (Borst, 2018). The question whether T4 neurons use multiplicative arithmetic in the computation of direction selectivity has been the object of heated scientific debate (Arenz et al., 2017; Behnia et al., 2014; Gruntman et al., 2018; Haag et al., 2016, 2017; Yang and Clandinin, 2018; Zavatone-Veth et al., 2020). Recently, a study has attempted to answer this question by performing whole-cell patch clamp of T4 neurons while showing the flies apparent-motion stimuli (Gruntman et al., 2018). Shortly, apparent motion stimuli consist of the alternating succession of multiple stationary visual stimuli which are separated by a fixed spatial distance (Cavanagh and Mather, 1989). Given proper calibration of the distance between the visual stimuli and of their timing, these stimuli create the illusion of motion. While recording the membrane potentials of T4 neurons in response to apparent motion stimuli, the authors did not find evidence of a multiplicative arithmetic operation. A shortcoming of this study is that – because it uses apparent motion stimuli – it ignores the complex spatiotemporal receptive fields of the input neurons to T4.

In **manuscript 1**, my co-authors and I show that multiplication-like arithmetic is indeed essential to motion vision in T4 cells. We show that Mi9 neurons control the input resistance of T4 neurons via the glutamate-gated chloride channel $\text{GluCl}\alpha$. While recording from T4 neurons during visual stimulation in its PD, we found a transient increase of the input resistance of the cells prior to voltage excursions. Such an increase of the input resistance is what is expected in cases of AND-NOT facilitation. This type of disinhibitive multiplication is reliant on the conductances elicited by the inputs to T4 neurons (reviewed in 1.3.3). This led us to electrophysiologically record from the columnar inputs to T4 neurons while subjecting the fly to the exact same battery of stimuli used when recording from T4 cells.

As of yet, it is impossible to record simultaneously from all the inputs to a single T4 neuron. However, because we can record the receptive field of the cells we measure, we can align the respective responses of different neurons to a single point in space. We know that the inputs a single T4 cell receives from Mi9, Mi1/Tm3, and Mi4/C3 originate in different columns. After measuring all of T4's columnar inputs, we can make a *post hoc* alignment of their responses to recreate the input sequences that are expected to shape the T4 cell's voltage responses to motion in its preferred direction (PD) and in its null direction (ND). After alignment, we show that there is a '**window of opportunity**' which appears only when visual stimuli move in a T4 neuron's preferred direction. In this case, Mi9 releases T4 from shunting inhibition while Tm3 and Mi1 are still not fully active. At this moment, the input resistance of T4 increases. When this state of high input resistance coincides with the excitatory inputs from Tm3 and Mi1 neurons, a multiplication-like operation eq. (14 to 19) is performed on the dendrites of T4. In the null direction (ND), we found that inhibitory Mi4 and C3 neurons perfectly overlap their responses with those of Tm3 and Mi1 neurons.

Finally, we show that the role of Mi9 is to shunt T4 neurons when stimuli move in a direction oblique to a T4' PD. This shunting occurs between $PD \pm 60^\circ$ and $PD \pm 90^\circ$. Mi9, Mi4, and C3 are thought to inhibit T4 neurons when stimuli move in a T4's ND (Arenz et al., 2017). It is only when visual stimuli move in a T4's PD that Mi9 releases T4 from shunting inhibition hence allowing for a disinhibitive multiplication. The further the angle of the stimulus is from the PD of a T4 neuron, the smaller the window of opportunity becomes (Extended Data Fig. 7 of manuscript 1). When the angle of the stimulus is too far from a T4's PD, inhibition from Mi9 neurons overlaps with the excitation from Tm3 and Mi1 neurons (Extended Data Fig. 7 of manuscript 1).

3.1.3 Mechanisms of null direction suppression

Measuring GCaMP signals in T4 neurons, recent studies have shown a suppression of T4 responses when visually stimulated with apparent motion in their ND (Haag et al., 2016, 2017). Here, the response to sequential stimulation of neuro-ommatidia in ND is less than the linear expectation of the responses to the stimulation of each single ommatidium. The so-called 'ND suppression' could result from an AND-NOT veto gate (reviewed in 1.3.3). Biologically, this would be implemented by the conjunction of inhibition from Mi4 and C3 inputs and excitation from Tm3 and Mi1 inputs onto T4 dendrites. In **manuscript 1**, we show that when a T4 neuron is

stimulated with bright edges moving in its ND, the respective membrane potential deflections of Mi4 and of C3 overlap perfectly with the respective membrane potential deflections of Mi1 and of Tm3 neurons. In **manuscript 2**, we show that when a T4 neuron is stimulated in its ND with moving gratings, aligned membrane potentials recorded from Mi4, C3, and Mi9 inputs overlap with the membrane potentials of Mi1 and of Tm3 inputs. In **manuscript 1**, we further show an asymmetric trailing of anticorrelated responses to light stimuli in the spatiotemporal receptive fields of T4 neurons (Fig. 1e of manuscript 1). This anticorrelation could either be due to the excitation of T4 in the dark or to its inhibition in the light. Because the trailing is on the null side of T4's receptive field, it is thought that it is a product of ON sensitive Mi4 and C3 inhibitory inputs mediated by GABAergic Rdl receptors (Fendl et al., 2020).

The nature of the arithmetic operation happening on the proximal side of T4 dendrites is still unknown. Indeed, a subtractive, or a divisive operation could be implemented. This is dependent on the reversal potentials associated to inhibitory currents and on the amplitude of these conductances. As seen in 1.3.2, the more negative E_i is compared to the resting membrane potential, the more the equation for the membrane eq. (12) resembles a linear subtraction. However, as seen in eq. (13), if E_i lies close to the resting membrane potential while g_i is high, then it is likely that the inhibition onto T4 is shunting and thus divisive. In **manuscript 1**, we show that a slight drop in T4's input resistance happens in response to motion in the ND. This is a hint to the implementation of a shunting divisive operation. Further electrophysiological experiments aiming to understand the operation involved in ND suppression are still needed. One could deplete T4 dendrites from Rdl by using cell type specific RNAi and see if T4 neurons still perform ND suppression, if there is a change in the reversal potentials of currents after local application of GABA, or if there are changes in the kinetics of the input resistance of T4 neurons in response to edges moving in its ND.

3.1.4 Other nonlinearities

Types of nonlinearities other than operational nonlinearities are known or hypothesized to happen in T4 neurons and in its inputs. These are 1) nonlinearities introduced by voltage-gated ion channels, 2) nonlinearities of the transformation from neurotransmitter to membrane potentials in the post-synapse, and 3) nonlinearities of the transformation from membrane potentials to neurotransmitter exocytosis.

1) **Voltage-gated ion channels** are a well-documented source of nonlinearity present in neurons. In T4 neurons, the voltage-gated Na^+ channels *paralytic* (para) is found along the axons while the inwardly rectifying *hyperpolarization-activated* I_h channel is present on the dendrites (Fendl et al., 2020). Yet, in T4 neurons the function of these voltage-gated ion channels is still unknown. They could for instance combine with the cell's intrinsic passive membrane low-pass filtering properties in order to create a phenomenological band-pass filter. Such mechanism of temporal filtering is reviewed in detail in 1.2.3. Yet, it is not clear which advantage T4 neurons would gain from acquiring band-pass filter properties. Indeed, this would be a step back from a direction-selective system which we describe in **manuscript 1** as being free from the voltage-dependence limiting threshold-based systems (Srinivasan and Bernard, 1976) and less sensitive to changes in signal amplitudes (Borst, 2018). In T4 neurons, voltage-gated ion channels could also be used to transform a graded signal coming from the dendrites into action potentials at the level of T4 terminals. The latter is less likely given the electrical compact morphology of T4 neurons which makes them quasi-isopotential. Indeed, any action potential happening in a quasi-isopotential neuron would be expected to be detectable at the soma. In any case, further experiments aimed at characterizing the properties of voltage-gated ion channels in T4 neurons and in its inputs are still needed.

2) Nonlinearities could be found at the level of the **neurotransmitter receptors** on the postsynaptic membrane. They would involve the transformation from ligand binding (to ionotropic or metabotropic receptors) into membrane potentials. In mechanistic models of neuronal networks, these non-linearities can be simulated by adding a threshold or a nonlinear transformation. In its simplest form, this can be implemented by the use of Hill functions (Adler and Medzhitov, 2021). Nonlinearities found at the level of receptors could help in the filtering of signals needed by elementary motion detectors. RNA sequencing has hinted to the possible expression of metabotropic receptors sensitive to ACh or to GABA in T4 neurons (Davis et al., 2020). The presence of metabotropic GABA_A receptors coupled to G proteins inwardly rectifying K^+ (GIRK) are a possible source of a delaying non-linearity (Davis et al., 2020; Lüscher and Slesinger, 2010). Such G protein-coupled receptor could be useful in leading to further delaying of inhibition provoked by GABAergic inputs. They could also explain the strong inward rectification of the currents induced by the application of GABA onto T4 dendrites (Extended Data

Fig.4 in manuscript 1). A biophysical characterization of each receptor present on T4 is ultimately a goal which would allow to understand the role of each receptor in the computations T4 neurons perform. This type of studies are pressing since in comparison with their mammalian counterpart, ion channels in invertebrate are not as well-characterized (Littleton and Ganetzky, 2000; Podlaski et al., 2017).

3) The level of linearity of the **transformation** from membrane potential to neurotransmitter release in T4 and in its inputs is still elusive. In **manuscript 1**, the assumption of the conductance model is that the inputs to T4 have a threshold under which the neurons do not release neurotransmitters. The instauration and the values given to such a rectilinear transformation are however arbitrary. The natural question which can be asked here is on the nature of the cells' encoding of information. Do neurons in the direction-selective circuit base their neurotransmitter release on a binary (action potentials) code, or, do they use an analogue (graded potentials) code? Given the quasi-isopotential nature of the neurons and the electrophysiological recordings shown in **manuscripts 1** and **2**, it is unlikely that T4 neurons or that their inputs use a spike-based code. If this was the case, one would record those spikes from the cell body.

If these neurons are 'graded-potential neurons', they could encode information similarly to vertebrate **photoreceptors**. Vertebrate photoreceptors demonstrate a **tonic graded** neurotransmitter release (Heidelberger, 2007). In the motion vision circuit of *Drosophila*, further knowledge about the transformation between membrane potentials and exocytosis would be advantageous when trying to build **biophysically realistic mechanistic models**. To that end, one could perform whole-cell recordings of an Mi9 neuron while simultaneously imaging glutamate release with the genetically encoded glutamate sensor iGluSnFR (Richter et al., 2018). Using iGluSnFR, a direct correlation between membrane potentials and glutamate release could be made. With the recent and constant creation and optimization of fluorescent neurotransmitter reporters (Jing et al., 2018; Marvin et al., 2013; Patriarchi et al., 2018), the ability to perform this type of experiments for all the columnar inputs to T4 dendrites is likely to be imminent.

3.2 Biophysically realistic, conductance-based modeling

It is not possible to simultaneously record the membrane potential of every single neuron in a neuronal circuit. Hence, neuroscientists build mechanistic models of neuronal networks. These models allow neuroscientists to simulate the temporal properties emerging from these circuits. The simplest type of network is the one

containing **nodes** representing neurons and **edges** representing the connections between neurons. The connections between neurons are at best based on anatomical reconstructions of the neuronal circuit of interest. This type of reconstruction is reviewed in 1.5.3 and was used in the conductance-based single-compartment models described in **manuscripts 1** and **2**.

3.2.1 Single- vs. multi-compartmental modeling

In **manuscript 1**, we built a passive **single-compartment model** reflecting the direction-selective operation happening at the level of T4 dendrites. For that, we used measured electrophysiological membrane potentials from T4 neurons and from all its columnar inputs in response to an identical set of stimuli. In other words, we measured the inputs to T4 as well as T4 responses. We further measured the reversal potential associated with the currents carried by each major ionotropic receptor type. Using the membrane equation eq. (11) we built a passive conductance-based model which contained free parameters representing the reversal potential and the gain of the leak conductance of T4 neurons as well as two free parameters per input to T4: a threshold below which all conductances were set to zero, and a gain. Using a least-square regression algorithm to find values for the free parameters, we could mechanistically describe the operations resulting in T4's direction selectivity. In **manuscript 2**, we used a similar approach. We simulated a neuronal circuit containing the ten neuronal classes of the direction-selective network. Here, the gain of each connection was set according to the number of synapses present between the cells. The model was ultimately trained on electrophysiological recordings from Mi9, Tm3, Mi1, Mi4, and C3 neurons in response to an identical battery of stimuli. However, it is important to note that single-compartment models reduce the neurons to **isopotential** units (Herz et al., 2006). In a single-compartment model, the shape and the length of the processes, the spatial segregation of neurotransmitter receptors, or the segregation of voltage-gated ion channels on the membrane do not influence the propagation of currents.

Neurons have varying morphologies and it is likely that the morphology of a neuron can have an effect on its electrical properties (Gulledge and Bravo, 2016; Koch, 1999). According to notions brought by cable theory, the length of a cable given an axial resistivity and a membrane resistance has an impact on the propagation of current (Agmon-snrir and Segev, 1993). The branching of dendrites also plays a role in the propagation of current (Debanne, 2004; Koch, 1999). In many cases, the use

of single-compartment models might not be appropriate in order to model neurons (Tzilivaki et al., 2019).

Multi-compartmental models take into account the morphology of the cell in the prediction they make about the evolution of electrical potentials along its membrane (Herz et al., 2006). Here, the neuron is not simplified as a single isopotential unit. It is divided into isopotential compartments linked by cables. A recent study made the comparison between the use of single compartment models and multi-compartment models of *Drosophila*'s local5 neurons in the lateral horn (Liu et al., 2021b). It found that a multi-compartment model can make better predictions of the amplitude of EPSPs measured in a local5 neuron than a single compartment model could. In **manuscripts 1 and 2**, we show that in T4 neurons and in their columnar inputs, the use of multi-compartment simulations does not provide any added advantage. These neurons are so small that they already are quasi-isopotential. This type of **electrical compact morphology** allows the clamping of an entire neuron (at steady state) from the soma. It also negates the role of its morphology in the computation of direction selectivity or in the differential filtering of signals.

3.2.2 Parameter Search

Parameters are the foundation on which all models rest. The challenge when building mechanistic models of biological phenomena is to find a realistic set of parameters which can **fit** and ultimately predict experimental data. The **error**, that is how far the output of the model deviates from experimental data is used to define how accurate the model is. In **manuscript 1**, we used a conductance model in order to understand the mechanisms underlying multiplicative arithmetic in the direction-selective T4 neurons. To this end, we used the recorded membrane potentials of T4 neurons and of their columnar inputs in response to a set of stimuli. We then tried to model the input/output transformation. Using the equation for the membrane potential V_m eq. (11), responses of T4 neurons can be understood as resulting from the interactions between a set of inhibitory, excitatory, and leak conductances and a set of reversal potentials. The conductances on T4 dendrites are controlled by the leak and by Mi9, Tm3, Mi1, Mi4, and C3 neurons. The response of a T4 neuron R_{T4} can then be calculated as

$$R_{T4} = \frac{E_{Glu} g_{Mi9} + E_{ACh} (g_{Tm3} + g_{Mi1}) + E_{GABA} (g_{Mi4} + g_{C3}) + E_{leak} g_{leak}}{g_{Mi9} + g_{Tm3} + g_{Mi1} + g_{Mi4} + g_{C3} + g_{leak}}, \quad (20)$$

where g denotes the relative conductance associated with each input neuron or with the leak. E denotes the reversal potential associated to the various currents.

Based on this simplified understanding of the input/output functions of T4 neurons, the modeled response of a T4 neuron M_{T4} is

$$M_{T4} = f(\theta) . \quad (21)$$

Here, $f()$ is a function based on eq. (20). It transforms the set of conductances and reversal potentials into the modeled membrane potential of T4 neurons. $f()$ takes θ as argument. $\theta = [\theta_1, \theta_2, \theta_3, \dots]$ is a set of free parameters applying a gain and a threshold to each conductance. M_{T4} is thus the output of the model given the free parameters θ .

In a next step, M_{T4} is compared with R_{T4} . This comparison gives the error such that

$$J(\theta) = \Sigma (R_{T4} - M_{T4}(\theta))^2 = Error. \quad (22)$$

To avoid confusion, $J(\theta)$ can also be referred to as the **cost function** or as the **fit function** (Baldi, 1995). The model is then fit to the experimental data R_{T4} by searching free parameter settings such that *Error* is minimized. The parameter search can be achieved via the use of a so-called **gradient descent**, an algorithm used to minimize the error (Fig. 15) (Baldi, 1995). In the simplest form of gradient descent, $J(\theta)$ is fed with initial random values of θ (comprised within set bounds). This results in a value for *Error*. The values of θ then keep on being changed until *Error* reaches a minimum. This works by simultaneously updating each free parameter (Baldi, 1995) such that

$$\theta_k := \theta_k - \alpha \frac{\partial}{\partial \theta_k} J(\theta) . \quad (23)$$

Here, k is one of n parameters. The variable α is the learning rate. It defines the size of each step (simultaneous change for each value of θ). The derivative gives the direction where each step should be made in order to minimize *Error*. By iterating this process, one hopes to reach a **convergence** (Baldi, 1995), that is a minimum where there are no new steps which can further minimize *Error* (Fig. 15).

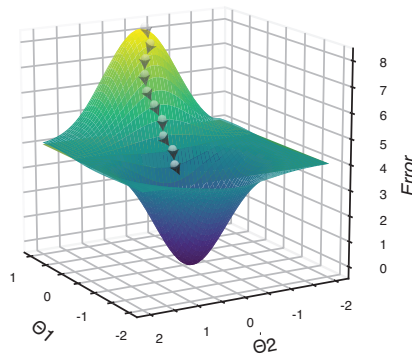


Fig. 15. Gradient descent and output of the fit function in parameter space

Output of the fit function in the parameter space of two parameters θ_1 and θ_2 . High *Error* (yellow) represents parameter settings for which there is a bad fit of the data. Low *Error*

(dark blue) represents parameter settings which fit the experimental data best. The grey ball represents the error for each new update of θ . The ball moves towards convergence.

3.2.3 Assessment of parameter-estimation

To repeat the gradient descent multiple times with different random initial settings of θ helps to discern a global minimum from local minima. When $J(\theta)$ is plotted for all possible combinations of free parameter settings θ , the output of the fit function in parameter space is revealed (Fig. 15). **Grid search** which performs a brute-force complete search over all possible parameter settings is a common strategy used to obtain all outputs of the fit function in parameter space (Bergstra and Bengio, 2012). The output of the fit function in parameter space can reveal if the relationship between the parameters of a model and its output is **degenerate** (Marder and Taylor, 2011). Different types of degeneracy exist. **Zero-slope degeneracy** occurs when the relationships between system parameters and system outputs have a slope of zero. In such a case, the parameter does not contribute to the behavior of the studied system (Marder and Taylor, 2011). **Compensating degeneracy** is found when multiple parameters compensate for each other. Compensating degeneracy leads to a strong positive correlation between the parameters compensating each other (Marder and Taylor, 2011) (Fig.16). In **manuscript 1**, compensating degeneracy was found between E_{Leak} and g_{Leak} .

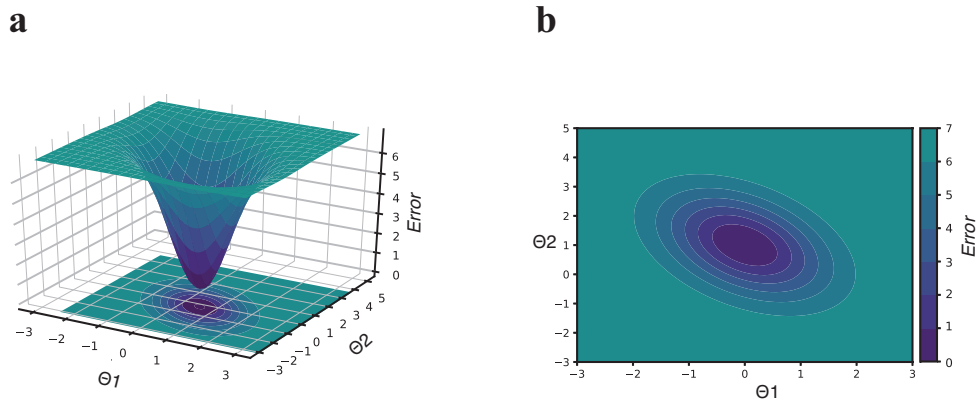


Fig. 16. Compensating degeneracy

(a) Output of the fit function in parameter space of two parameters θ_1 (x-axis) and θ_2 (y-axis). The z-axis is $Error = J(\theta)$ and described in eq. 22. In blue is the minimum where values of parameters θ_1 and θ_2 allow for the best fit of the model to the experimental data. **(b)** A 2-dimensional representation of the parameter space of θ_1 and θ_2 from **(a)** where dark blue values represent the minimal error. Here, compensating degeneracy is clearly visible.

In parameter space, the description of compensating degeneracy can be achieved via the use of **Hessian matrices**. Given parameters $\theta = [\theta_1, \theta_2]$ and a matrix \mathcal{S}

representing output of the fit function in parameter space, the resulting Hessian matrix is

$$\mathbf{H}(\mathbf{S}) = \begin{bmatrix} \frac{\partial^2 \mathcal{S}}{\partial \theta_1^2} & \frac{\partial^2 \mathcal{S}}{\partial \theta_1 \partial \theta_2} \\ \frac{\partial^2 \mathcal{S}}{\partial \theta_2 \partial \theta_1} & \frac{\partial^2 \mathcal{S}}{\partial \theta_2^2} \end{bmatrix}. \quad (24)$$

Because the Hessian matrix is based on the second-order partial derivatives of \mathbf{S} , it reflects the curvature of the fit function's output in parameter space. Using the Eigenvectors and the Eigenvalues of matrix \mathbf{H} , it is then possible to define the direction of **robustness** and the direction of **sensitivity** of the fit function in parameter space.

Robustness-direction is found along the Eigenvector with the smallest absolute eigenvalue. This Eigenvalue determines the range in robustness. **Sensitivity-direction** is found along the Eigenvector with the largest absolute Eigenvalue. This Eigenvalue determines the range in sensitivity. Explained in terms of linear transformations, the Eigenvector with the smallest absolute Eigenvalue represents the smallest determinant of the linear transformation. It points to the elongated axis of this distribution which is the robustness. The Eigenvector with the largest absolute Eigenvalue represents the largest determinant of the linear transformation. It points to the sensitivity of the fit function. Describing the robustness of degenerate solutions allows to know how resistant the solution is to perturbations (Goldman et al., 2001). On the other hand, sensitivity analysis is used to determine how changes in one parameter influence a model's behavior (Marder and Taylor, 2011).

Compensating degenerate solutions of a model might hint to the existence of homeostatic mechanisms (Maffei and Fontanini, 2009). In this case, the addition of extra parameters to the model could help discern if the degeneracy reflects real biological phenomena. However, increasing the dimensionality of the parameter space increases the computing time exponentially. This is prohibitively long for a grid search. High-dimensional parameter sets can in fact only be explored.

3.2.4 Simulator-based models

Mechanistic models are used to understand and predict how systems behave in various circumstances but they are not suited for statistical inference (Cranmer et al., 2020). An essential ingredient to both frequentist and Bayesian inference methods is the **likelihood** (Cranmer et al., 2020). Likelihood is expressed as $p(D|\theta)$. Here, D is the observed data. In our case, an analytical expression for the likelihood of the parameters given experimental observations is not available (Papamakarios and

Murray, 2018). Conventional Bayesian inference is therefore not applicable. For such cases, a set of algorithms for **simulation-based inference** (also known as **likelihood-free inference**) have been developed (Cranmer et al., 2020). These algorithms are based on **Approximate Bayesian computation** (ABC) (Papamakarios and Murray, 2018). In their simplest form, algorithms such as the **ABC rejection algorithm** repeatedly simulate data from a given model and from a given set of parameters (Papamakarios and Murray, 2018). They then reject parameter settings which generate synthetic data too different from the experimentally observed data. Such an approach, although it bypasses the need to calculate likelihoods, comes with its own limitations. The resulting parameter sample does not come from the real Bayesian posterior $p(\theta|D)$ but from the synthetic data. A solution to this is to directly learn the parametric approximation to the exact posterior (Papamakarios and Murray, 2018). This can be accomplished using **conditional density estimation** (Cranmer et al., 2020; Rothfuss et al., 2019). Here, what can be modeled is a conditional density such as the likelihood $p(D|\theta)$ or the posterior $p(\theta|D)$. Conditional density estimation has been implemented using neural density estimators (Gonçalves et al., 2020). Conditional density estimators which are based on deep neural networks do not reject the parameter settings generating data different from the observed data. They train deep neural conditional density estimators or classifiers on the observed data (Tejero-Cantero et al., 2020). **Deep generative neural networks** are a type of neural network which can be trained into density estimators (Liu et al., 2021a). Deep generative neural networks possess many hidden layers which are trained to approximate high dimensional probability distributions (Ruthotto and Haber, 2021). In **manuscript 1**, we were able to use a deep neural density estimator in order to estimate a posterior distribution consistent with measured voltage traces of T4 neurons.

3.3 Temporal filtering strategies in the optic lobe

The experimental study of network-based filtering in the brain has until now been a difficult task. Indeed, it cannot be achieved without a precise knowledge about neuronal connectivity or without a way to record simultaneously from all neurons of a circuit. Few animal models are suitable to these types of studies. In zebrafish, the ability to non-invasively record GCaMP signals (Yildizoglu et al., 2020), the extensive work currently being done to map neuronal connectivity (Kunst et al., 2019), and progress made in two-photon light-sheet microscopy (Wolf et al., 2015) make the larval zebrafish an promising vertebrate model to the study of neuronal networks.

In the motion vision pathway of *Drosophila*, we showed that simultaneous recording from multiple nodes of a network could be by-passed by *post-hoc* alignment of signals. This is reviewed in section 3.1.2. Alignment is only possible when a precise receptive field of the recorded neurons has been measured. As reviewed in section 1.6, the direction-selective circuit can be drawn as a complex network where photoreceptors first transform light information into biophysical signals. These signals are then relayed to neurons in the lamina and medulla. The lamina and medulla further transform and relay this information to the lobula and to the lobula plate. The flow of information goes unhindered to the central brain. However, this flow does not follow a simple feedforward pattern. There is a great amount of parallel, recurrent, and self-looping connectivity. Taken together, this complexity allows for the temporal and spatial filtering of the nodes in the motion vision pathway. Ultimately, it is a prerequisite to the computation of the direction of motion. Nevertheless, the more complex a network becomes, the more difficult it is to get an intuitive grasp of how its connectivity leads to specific patterns of activity. To this effect, the study of some of the recurring motifs contained within the motion vision pathway is a first step in understanding the temporal filtering strategies which emerge from it. Examples of such emerging patterns of connectivity are described in **manuscripts 1 and 2**.

3.3.1 Feedforward network motifs

Complex networks, be they biological, electronic, or linguistic, are studied across multiple fields of science because they can be reduced to patterns of connectivity between nodes in a network (Milo et al., 2002). A network consists of a set of nodes linked together by edges. The graphs thus formed can be **undirected**, that is where edges do not have a direction. They can also be **directed** and thus have edges with directionality. In the brain, edges between nodes (neurons) can be undirected via the use of bidirectional gap junctions (Nielsen et al., 2008). They can be directed via chemical synapses. In this thesis, only the latter is reviewed. The first step in understanding a directed

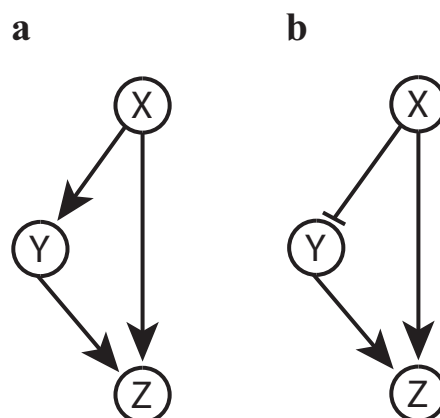


Fig. 17. Feedforward loop motifs
(a) Representation of a coherent feedforward loop with input X excites Y and Z, and Y excites Z. **(b)** Representation of an incoherent feedforward loop with input X inhibits Y but excites Z while Y excites Z (Adler and Medzhitov, 2021).

complex network is to reduce it to a set of interconnected **network motifs**. These motifs are recurring patterns of connections occurring in a complex network but not in a randomized way. The **feedforward loop** is one of these recurring network motifs (Adler and Medzhitov, 2021; Mangan and Alon, 2003; Milo et al., 2002). In its simplest form, the feedforward loop can be represented by three vertices X, Y, and Z where X is the input node, Y is the intermediate node, and Z is the output node (Fig. 17). If Y excites Z, the feedforward loop is **coherent** (Fig. 17a). If Y inhibits Z, the feedforward loop is termed **incoherent** (Fig. 17b). Coherent and incoherent feedforward loops exhibit distinct emerging temporal properties. A recent study has described the temporal properties of the feedforward loops present in the transcription networks of the bacterium *Escherichia coli* and the yeast *Saccharomyces cerevisiae* (Mangan and Alon, 2003). Intriguingly, the authors found that coherent feedforward loop can serve to delay regulation of an ‘output’ gene. Conversely, incoherent feedforward loops can accelerate the regulation of the output gene. In the direction-selective circuit of *Drosophila*, the connection between Mi1 as input node, Tm3 as intermediate node, and T4 as output node is an example of a coherent feedforward loop (Mangan and Alon, 2003).

3.3.2 Feedback network motifs

Network motifs termed **feedback loops** have been observed in many systems (Fig. 18). Notably, feedback loops have been an object of interest because of their ability to create oscillations (Adler and Medzhitov, 2021) or because they allow for the persistent activity of cells possessing short time-constants (Goldman, 2009).

In other words, feedback loops could be the mechanisms underlying the rhythmic activation of neuronal populations. They could also be network motifs essential to the

formation of short-term memories. The **self-loop** consists of a vertex with outputs onto itself (Fig. 18a). If this output is positive, it autoregulates its own levels which allows for the stability of the vertex (Adler and Medzhitov, 2021). In the optic lobe, L1 lamina neurons are glutamatergic. Yet they express the GluCl α receptor on their

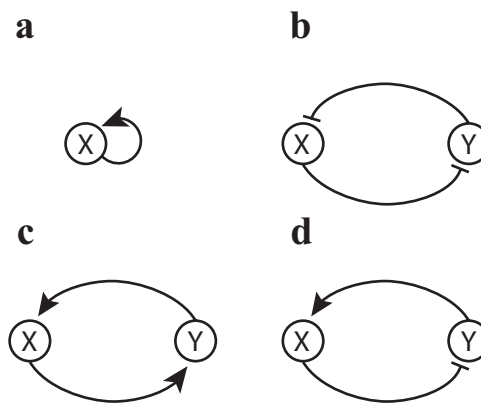


Fig. 18. Feedback loop motifs (a) Self-loop motif where X excites itself. (b) Toggle switch motif where X and Y mutually inhibit each other. (c) Lock-ON motif where X and Y mutually excite each other. (d) Oscillator motif where X excites Y while Y inhibits X (Adler and Medzhitov, 2021).

axon terminals (personal communications, Sandra Fendl). Each time L1 releases glutamate, it most likely also opens the GluCl α receptors on its terminals and thus inhibits itself. This could be an example of a negative feedback self-loop. Contrary to the positive (excitatory) self-loop, a negative self-loop allows to speed-up the kinetics of the node (Adler and Medzhitov, 2021). This is in accordance with L1's role in the fast kinetics of the ON motion vision circuit (Ammer et al., 2015). The possibility of describing the use and the function of a self-loop motif in the optic lobe is intriguing and requires further exploration.

Other feedback network motifs are the so-called **mutual feedback circuits**. The **toggle-switch** circuit where X and Y inhibit each other allows the nodes to switch between their final levels (Fig. 18b). Mi9 and Mi4 neurons – because of their mutual inhibition – are an example of toggle-switch feedback motif. In the **lock-ON** circuit, both X and Y are turned ON because of their mutual excitation (Fig. 18c). The interconnections between Mi1 and Tm3 make the connectivity between the two neurons a lock-ON motif. The **oscillator** circuit where X excites Y while Y inhibits X leads to the emergence of oscillations (Fig. 18d). The interconnections between L1 and Mi1 neurons is an example of oscillator circuit. However, the functional relevance of various feedback loops is also dependent on the strength of the connections between the neurons. For instance, any asymmetry found in the number of input/output connections between L1 and Mi1 neurons would be expected to influence the temporal properties emerging from this network motif. As a matter of fact, EM studies have revealed that L1 sends more inputs onto Mi1 than it receives from it (Shinomiya et al., 2019; Takemura et al., 2017). Finally, even if these motifs are present in the optic lobe, they are only small pieces of the complex network making for the whole direction-selective circuitry. It is thus essential, to not only explore these small network motifs, but to also study the bigger networks that they build together.

3.3.3 Hyper-motifs

Network motifs assembled to create larger networks are called **network hyper-motifs** (Adler and Medzhitov, 2021). Because of their increased complexity, network hyper-motifs are closer to the biological reality of neuronal circuits than network motifs are. As expected, increase in complexity of the connectivity also leads to a diversification of the temporal properties emerging from network hyper-motifs. It is possible to create a network performing any wished temporal low-pass filtering by building a hyper-motif composed of many coherent feedforward loops

(Goldman, 2009). In such a network, each vertex represents a different temporal filtering stage. Depending on the architecture of the hyper-motif, the responses of individual cells in the network are only limited by the fact that the response of the i^{th} neuron (node) in the hyper-motif has to be the sum of the first i neuronal activities (Goldman, 2009). A similar circuit has been suggested to be implemented in the cat's oculomotor neural integrator (Delgado-García et al., 1989; Escudero et al., 1992). In the optic lobe of the fly, such a feedforward construction of the network could be used to implement the differential filtering shown in **manuscript 2**. However, the physiological and morphological study of the neurons belonging to the motion vision circuit as well as their modelling hint to the implementation of a different mechanism.

A recurrent network behaving in a feedforward manner could also result in differential filtering of individual nodes (Goldman, 2009). An advantage this type of recurrent network brings to a circuit is that it allows for a richer set of emerging temporal properties. Concretely, because it encompasses the temporal properties of feedforward but also of feedback loops, it can react differently to different stimuli. It can thus allow a circuit to optimally respond to a battery of stimuli. While the motion vision circuit in *Drosophila* possesses many feedback loops, it is still a feedforward circuit since it ultimately propagates activity from the retina through the lamina, the medulla, the lobula, and the lobula plate (Fig. 19). In **manuscript 2**, the

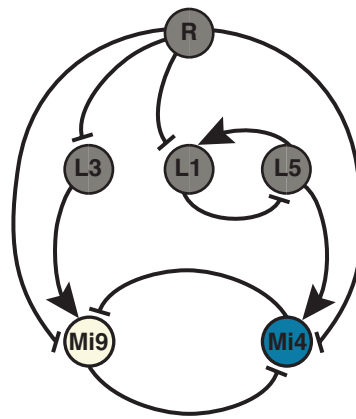


Fig. 19. Feedforward in disguise
Schematic representation of the network hyper-motif containing the L1/L5 oscillatory feedback loop and the Mi4/Mi9 toggle-switch feedback loop. Yet information is processed in a feedforward manner from photoreceptors (R) to Mi9 (white) and Mi4 (blue) neurons.

effect such a “feedforward loop in disguise” (Goldman, 2009) has on the time constants of single neurons is studied. We show that the direction-selective network can be described as a hyper-motif containing both feedforward loop and feedback loop characteristics. This in turn, allows it to mediate the emergence of a vast number of temporal filters.

3.4 Conclusion and outlook

More than half a century after Hassenstein and Reichardt propose their correlation type motion detector (Hassenstein and Reichardt, 1956), the manuscripts in this thesis describe the biophysical implementation of multiplication-like arithmetic in T4 neurons as well as the emergence of differential filtering in the inputs to T4. Taken together, these describe the biological implementation of the two first stages of a Hassenstein–Reichardt half-detector.

Similar arithmetic operations and filtering strategies are possibly occurring in other systems. In the mammalian retina, local computation of direction-selectivity has been revealed at the connections single bipolar cells make onto direction-selective retinal ganglion cells (Matsumoto et al., 2021). Direction selective boutons on the dendrites of retinal ganglion cells result from the activity of bipolar cells, starburst amacrine cells, and wide-field cells (Fig. 20) (Matsumoto et al., 2021). The biophysical mechanisms described in this thesis could be implemented in this type of microcircuit. Recording unitary synaptic events in mammalian neurons is possible (Vandael et al., 2021). However, because the axon terminals of bipolar cells are situated in the inner plexiform layer of the retina, the use of electrophysiology to

describe the operations happening at single boutons under visual stimulation of the retina still remains a challenge. In this regard, the easily accessed and quasi-isopotential neurons in the medulla and the lobula plate of *Drosophila* remain an ideal playground to explore the physiological basis of this type of passive neuronal computation.

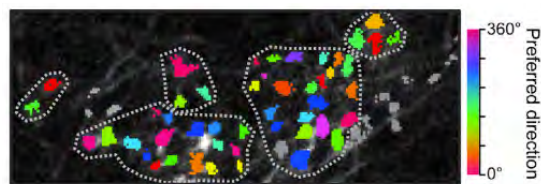


Fig. 20. Direction selectivity at single boutons
Field of view during glutamate imaging in direction selective retinal ganglion cells and using iGluSnFR. Preferred direction of identified tuned single boutons (color). The dotted lines are the rough borders of each cell. Image taken with permission from Matsumoto et al., 2021.

In *Drosophila*, many of the central questions still remain unanswered. For instance, a biophysical inspection of ND suppression in T4 neurons is still lacking. It is still unclear if this suppression is implemented via subtraction- or via division-like arithmetic. Further use of RNAi tools to target different channels presumed to be involved in the ND suppression of T4 neurons while performing whole-cell patch clamp is likely to give insights fundamental to answer this question. Furthermore, it is still unclear how the direction of motion is computed by T5 neurons in the OFF pathway (Gruntman et al., 2019; Serbe et al., 2016). If multiplication-like arithmetic

similar to the one implemented by T4 neurons is also implemented by T5 neurons, is still elusive. Given the neuronal inputs to T5 neurons (Shinomiya et al., 2019), there is no intuitive explanation for the implementation of disinhibitive multiplication. An electrophysiological characterization of T5 neurons and of their inputs following strategies described in this thesis is still missing. Such experiments are likely to give new insights into the biophysical mechanisms underlying direction selectivity in T5 neurons.

Finally, the membrane potentials of T4 and T5 neurons are determined by the opening and the closing of ion-channels. The manuscripts in this thesis explore properties of only a few of these channels. The biophysical properties and the role of ionotropic, voltage-gated, and of metabotropic channels present in the membrane of T4 and of T5 neurons still needs to be investigated (Davis et al., 2020; Fendl et al., 2020; Pankova and Borst, 2016). Taken together, these remaining questions give a breath of possibilities and challenges to future researchers using the visual system of *Drosophila* as a model to understand how the brain computes.

BIBLIOGRAPHY

- Adler, M., and Medzhitov, R. (2021). Emergence of dynamic properties in network hyper-motifs. *arXiv* 1–28
- Agmon-snir, H., and Segev, I. (1993). Signal delay and input synchronization in passive dendritic structures. *Journal of Neurophysiology* **70**, 2066–2085
- Ammer, G., Leonhardt, A., Bahl, A., Dickson, B.J., and Borst, A. (2015). Functional specialization of neural input elements to the *Drosophila* ON motion detector. *Current Biology* **25**, 2247–2253
- Arenz, A., Drews, M.S., Richter, F.G., Ammer, G., Arenz, A., Drews, M.S., Richter, F.G., Ammer, G., and Borst, A. (2017). The temporal tuning of the *Drosophila* motion detectors is determined by the dynamics of their input elements. *Current Biology* **27**, 929–944
- Azevedo, A.W., Wilson, R.I., Azevedo, A.W., and Wilson, R.I. (2017). Active mechanisms of vibration encoding and frequency filtering in central mechanosensory neurons. *Neuron* **96**, 446–460
- Baldi, P. (1995). Gradient descent learning algorithm overview: a general dynamical systems perspective. *IEEE* **6**, 182–195
- Barlow, H.B., and Levick, W.R. (1965). The mechanism of directionally selective units in rabbit's retina. *The Journal of Physiology* **178**, 477–504
- Behnia, R., Clark, D.A., Carter, A.G., Clandinin, T.R., and Desplan, C. (2014). Processing properties of ON and OFF pathways for *Drosophila* motion detection. *Nature* **512**, 427–430
- Bergstra, J., and Bengio, Y. (2012). Random search for hyper-parameter optimization. *Journal of Machine Learning Research* **13**, 281–305
- Borst, A. (2018). A biophysical mechanism for preferred direction enhancement in fly motion vision. *PLoS Computational Biology* **14**, 1–15
- Borst, A., and Abarbanel, H.D.I. (2007). Relating a calcium indicator signal to the unperturbed calcium concentration time-course. *Theoreticcal Biology and Medical Modelling* **13**, 1–13
- Borst, A., and Helmstaedter, M. (2015). Common circuit design in fly and mammalian motion vision. *Nature Neuroscience* **18**, 1067–1076
- Borst, A., Haag, J., and Reiff, D.F. (2010). Fly motion vision. *Annual Review of Neuroscience* **33**, 49–70
- Brand, A.H., and Perrimon, N. (1993). Targeted gene expression as a means of altering cell fates and generating dominant phenotypes. *Development* **118**, 401–415
- Briggman, K.L., and Bock, D.D. (2012). Volume electron microscopy for neuronal

- circuit reconstruction. *Current Opinion in Neurobiology* **22**, 154–161
- Brown, B.D., Heinze, W.J., and Davis, J.M. (1979). How does adrenaline accelerate the heart?. *Nature* **280**, 235–236
- Buzsáki, G. (2006). *Rhythms of the brain* (New York: Oxford University Press)
- Carr, C.E. (1993). Delay line models of sound localization in the barn owl. *American Zoologist* **33**, 79–85
- Cascio, M. (2004). Structure and function of the glycine receptor and related nicotinic receptors *. *The Journal of Biological Chemistry* **279**, 19383–19386
- de Castro, F. (2019). Cajal and the spanish neurological school: neuroscience would have been a different story without them. *Frontiers in Cellular Neuroscience* **13**, 1–14
- Catterall, W.A. (1998). Structure and function of neuronal Ca²⁺ channels and their role in neurotransmitter release. *Cell Calcium* **24**, 307–323
- Cavanagh, P., and Mather, G. (1989). Motion: the long and short of it. *Spatial Vision* **4**, 103–129
- Chalfie, M., Tu, Y., Euskirchen, G., Ward, W.W., and Prasher, D.C. (1994). Green fluorescent protein as a marker for gene expression. *Science* **263**, 802–804
- Chen, T., Wardill, T.J., Sun, Y., Pulver, S.R., Renninger, S.L., Baohan, A., Schreiter, E.R., Kerr, R.A., Orger, M.B., Jayaraman, V., et al. (2013). Ultrasensitive fluorescent proteins for imaging neuronal activity. *Nature* **499**, 295–302
- Clark, D.A., Bursztyn, L., Horowitz, M.A., Schnitzer, M.J., and Clandinin, T.R. (2011). Defining the computational structure of the motion detector in *Drosophila*. *Neuron* **70**, 1165–1177
- Cole, K.S., and Moore, J.W. (1960). Ionic current measurements in the squid giant axon membrane. *The Journal of General Physiology* **44**, 123–167
- Cranmer, K., Brehmer, J., and Louppe, G. (2020). The frontier of simulation-based inference. *PNAS* **117**, 30055–30062
- Cruse, H. (2009). *Neural networks as cybernetic systems* (Bielefeld: Brains, Minds & Media)
- Cully, D.F., Paress, P.S., Liu, K.K., Schaeffer, J.M., and Arena, J.P. (1996). Identification of a *Drosophila melanogaster* glutamate-gated chloride channel sensitive to the antiparasitic agent avermectin. *Journal of Biological Chemistry* **33**, 20187–20191
- Cummins, T.R., Xia, Y., and Haddad, G.G. (1994). Functional properties of rat and

- human neocortical voltage-sensitive sodium currents. *Journal of Neurophysiology* **71**, 1052–1064
- Darrow, K.N., Maison, S.F., and Liberman, M.C. (2006). Cochlear efferent feedback balances interaural sensitivity. *Nature Neuroscience* **9**, 1474–1476
- Davis, F.P., Nern, A., Picard, S., Reiser, M.B., Rubin, G.M., Eddy, S.R., and Henry, G.L. (2020). A genetic, genomic, and computational resource for exploring neural circuit function. *eLife* **9**
- Debanne, D. (2004). Information processing in the axon. *Nature Reviews Neuroscience* **5**, 304–316
- Delgado-García, J.M., Vidal, P.P., Gómez, C., and Berthoz, A. (1989). A neurophysiological study of prepositus hypoglossi neurons projecting to oculomotor and preoculomotor nuclei in the alert cat. *Neuroscience* **29**, 291–307
- Denk, W., and Horstmann, H. (2004). Serial block-face scanning electron microscopy to reconstruct three-dimensional tissue nanostructure. *PLOS Biology* **2**
- Dietzl, G., Chen, D., Schnorrer, F., Su, K., Barinova, Y., Fellner, M., Gasser, B., Kinsey, K., Oettel, S., Scheibla, S., et al. (2007). A genome-wide transgenic RNAi library for conditional gene inactivation in *Drosophila*. *Nature* **448**, 151–157
- DiFrancesco, D., and Ojeda, C. (1980). Properties of the current i_f in the sino-atrial node of the rabbit compared with those of the current i_K in purkinje fibres. *Journal of Physiology* **308**, 353–367
- DiFrancesco, D. (1981). A study of the ionic nature of the pace-maker current in calf purkinje fibres. *Journal of Physiology* **314**, 377–393
- Dorkenwald, S., Schubert, P.J., Killinger, M.F., Urban, G., Mikula, S., Svara, F., and Kornfeld, J. (2017). Automated synaptic connectivity inference for volume electron microscopy. *Nature Methods* **14**, 435–442
- Drews, M.S., Leonhardt, A., Pirogova, N., Richter, F.G., Schuetzenberger, A., Braun, L., Serbe, E., and Borst, A. (2020). Dynamic signal compression for robust motion vision in flies. *Current Biology* **30**, 209–221
- Egelhaaf, M., Borst, A., and Reichardt, W. (1989). Computational structure of a biological motion-detection system as revealed by local detector analysis in the fly's nervous system. *Journal of the Optical Society of America* **6**, 1070–1087
- Egelhaaf, M., Borst, A., Pils, B., Kybernetik, M., and Tiibingen, E.R.G. (1990).

- The role of GABA in detecting visual motion. *Brain Research* **509**, 156–160
- Escudero, M., de la Cruz, R.R., and Delgado-García, J.M. (1992). A physiological study of vestibular and prepositus hypoglossi neurones projecting to the abducens nucleus in the alert cat. *The Journal of Physiology* **458**, 539–560
- Fendl, S., Vieira, R.M., and Borst, A. (2020). Conditional protein tagging methods reveal highly specific subcellular distribution of ion channels in motion-sensing neurons. *eLife* **9**, 1–26
- Fischbach, K.F., and Dittrich, A.P.M. (1989). The optic lobe of *Drosophila melanogaster*. I. A Golgi analysis of wild-type structure. *Cell and Tissue Research* **258**, 441–475
- Fisher, Y.E., Leong, J.C.S., Sporar, K., Ketkar, M.D., Gohl, D.M., Clandinin, T.R., Fisher, Y.E., Leong, J.C.S., Sporar, K., Ketkar, M.D., et al. (2015). A class of visual neurons with wide-field properties is required for local motion Detection. *Current Biology* **25**, 3178–3189
- Frolov, R. V, Bagati, A., Casino, B., Singh, S., Frolov, R. V, Bagati, A., Casino, B., and Singh, S. (2012). Potassium channels in *Drosophila*: historical breakthroughs, significance, and perspectives. *Journal of Neurogenetics* **26**, 275–290
- Goldman, M.S. (2009). Memory without feedback in a neural network. *Neuron* **61**, 621–634
- Goldman, M.S., Golowasch, J., Marder, E., and Abbott, L.F. (2001). Global structure, robustness, and modulation of neuronal models. *Journal of Neuroscience* **21**, 5229–5238
- Gonçalves, P.J., Lueckmann, J.M., Deistler, M., Nonnenmacher, M., Öcal, K., Bassetto, G., Chintaluri, C., Podlaski, W.F., Haddad, S.A., Vogels, T.P., et al. (2020). Training deep neural density estimators to identify mechanistic models of neural dynamics. *eLife* **9**, 1–46
- Götz, K.G. (1964). Optomotorische Untersuchung des visuellen Systems einiger Augenmutanten der Fruvhtfliege *Drosophila*. *Kybernetik* **2**, 77–92
- Groschner, L.N., and Miesenbock, G. (2019). Mechanisms of sensory discrimination: insights from *Drosophila* olfaction. *Annual Review of Biophysics* **48**, 209–229
- Gruntman, E., Romani, S., and Reiser, M.B. (2018). Simple integration of fast excitation and offset, delayed inhibition computes directional selectivity in *Drosophila*. *Nature Neuroscience* **21**, 250–257
- Gruntman, E., Romani, S., and Reiser, M.B. (2019). The computation of

directional selectivity in the *Drosophila* OFF motion pathway. *eLife* **8**, 1–26

- Gulledge, A.T., and Bravo, J.J. (2016). Neuron morphology influences axon initial segment plasticity. *eNeuro* **3**, 255–265
- Haag, J., Arenz, A., Serbe, E., Gabbiani, F., and Borst, A. (2016). Complementary mechanisms create direction selectivity in the fly. *eLife* **5**, 1–15
- Haag, J., Mishra, A., and Borst, A. (2017). A common directional tuning mechanism of *Drosophila* motion-sensing neurons in the ON and in the OFF pathway. *eLife* **6**, 1–15
- Hardie, R.C. (1989). A histamine-activated chloride channel involved in neurotransmission at a photoreceptor synapse. *Nature* **339**, 704–706
- Harris, K.M., Perry, E., Bourne, J., Feinberg, M., Ostroff, L., and Hurlburt, J. (2006). Uniform serial sectioning for transmission electron microscopy. *The Journal of Neuroscience* **26**, 12101–12103
- Harrison, J.B., Chen, H.H., Sattelle, E., Barker, P.J., Huskisson, N.S., Rauh, J.J., Bai, D., and Sattelle, D.B. (1996). Immunocytochemical mapping of a C-terminus anti-peptide antibody to the GABA receptor subunit, RDL in the nervous system of *Drosophila melanogaster*. *Cell and Tissue Research* **284**, 269–278
- Hassenstein, B. (1951). Ommatidienraster und Afferente Bewegungs-Integration. *Zeitschrift für vergleichende Physiologie* **33**, 301–326
- Hassenstein, B., and Reichardt, W. (1956). Systemtheoretische Analyse der Zeit-, Reihenfolgen- und Vorzeichenauswertung bei der Bewegungsperzeption des Rüsselkäfers *Chlorophanus*. *Zeitschrift für Naturforschung* **11**, 513–524
- Hauswirth, O., Noble, D., and Tsien, R.W. (1968). Adrenaline: mechanism of action on the pacemaker potential in cardiac Purkinje fibers. *Science* **162**, 916–917
- Heidelberger, R. (2007). Mechanisms of tonic, graded release: lessons from the vertebrate photoreceptor. *Journal of Physiology* **585**, 663–667
- Heisenberg, M., and Buchner, E. (1977). The rôle of retinula cell types in visual behavior of *Drosophila melanogaster*. *Journal of Comparative Physiology* **117**, 127–162
- Hermann, L. (1874). *Gründniss der physiologie des menschen* (Berlin: August Hirschwald)
- Herz, A.V.M., Gollisch, T., Machens, C.K., and Jaeger, D. (2006). Modeling single-neuron dynamics and computations: a balance of detail and

- abstraction. *Science* **314**, 80–85
- Hille, B. (1984). Ionic channels of excitable membranes (Sunderland: Sinauer)
- Hille, B. (1991). Ionic channels of excitable membranes (Sunderland)
- Hodgkin, A.L., and Huxley, A.F. (1952a). A quantitative description of membrane current and its application to conduction and excitation in nerve. *J. Physiol.* **117**, 500–544
- Hodgkin, A.L., and Huxley, A.F. (1952b). The components of membrane conductance in the giant axon of *Loligo*. *The Journal of Physiology* **116**, 473–496
- Hodgkin, A.L., and Katz, B. (1949). The effect of sodium ions. *J. Physiol.* **108**, 37–77
- Hodgkin, A.L., Huxley, A.F., and Katz, B. (1952). Measurements of current-voltage relations in the membrane of the giant axon of *Loligo*. *Journal of Physiology* **116**, 424–448
- Hutcheon, B., and Yarom, Y. (2000). Resonance, oscillation and the intrinsic frequency preferences of neurons. *Trends Neuroscience* **23**, 216–221
- Jeffress, L.A. (1948). A place theory of sound localization. *Journal of comparative and physiological psychology* **41**, 35–39
- Jing, M., Zhang, P., Wang, G., Feng, J., Mesik, L., Zeng, J., Jiang, H., Wang, S., Looby, J.C., Guagliardo, N.A., et al. (2018). A genetically encoded fluorescent acetylcholine indicator for *in vitro* and *in vivo* studies. *Nature Biotechnology* **36**, 726–737
- Joesch, M., Schnell, B., Raghu, S.V., Reiff, D.F., and Borst, A. (2010). ON and OFF pathways in *Drosophila* motion vision. *Nature* **468**, 300–304
- Kamb, A., Iverson, L.E., and Tanouye, M.. (1987). Molecular characterization of *Shaker*, a *Drosophila* gene that encodes a potassium channel. *Cell* **50**, 405–413
- Koch, C. (1999). Biophysics of computation (New York: Oxford University Press)
- Koch, C., and Poggio, T.A. (1987). *Biophysics of Computation : Neurons , Synapses and Membranes*. In Synaptic Function, G.M. Edelman, W.E. Gall, and W.M. Cowan, eds. (John Wiley), pp. 0–500
- Koch, C., and Segev, I. (2000). The role of single neurons in information processing. *Nature Neuroscience* **3**, 1171–1177
- Kohn, J.R., Portes, J.P., Christenson, M.P., Abbott, L.F., and Behnia, R. (2021). Flexible filtering by neural inputs supports motion computation across states and stimuli. *Current Biology* **31**, 5249–5260

- Kumar, J.P. (2012). Building an ommatidium one cell at a time. *Developmental Dynamics* **241**, 136–149
- Kunst, M., Laurell, E., Mokayes, N., Kramer, A., Kubo, F., Fernandes, A.M., Förster, D., Dal Maschio, M., and Baier, H. (2019). A cellular-resolution atlas of the larval zebrafish brain. *Neuron* **103**, 21–38
- Lapicque, L. (1907). Recherches quantitatives sur l'excitation électrique des nerfs traitée comme une polarisation. *J. Physiol. Pathol. Gen* **9**, 620–635
- Lerner, T.N., Ye, L., and Deisseroth, K. (2016). Communication in neural circuits: tools, opportunities, and challenges. *Cell* **164**, 1136–1150
- Littleton, J.T., and Ganetzky, B. (2000). Ion channels and synaptic organization: analysis of the *Drosophila* genome. *Neuron* **26**, 35–43
- Liu, W.W., and Wilson, R.I. (2013). Glutamate is an inhibitory neurotransmitter in the *Drosophila* olfactory system. *PNAS* **110**, 10294–10299
- Liu, Q., Xu, J., Jiang, R., and Wong, W.H. (2021a). Density estimation using deep generative neural networks. *PNAS* **118**, 1–6
- Liu, T.X., Davoudian, P.A., and Lizbinski, K.M. (2021b). Connectomic features underlying diverse synaptic connection strengths and subcellular computation
- Llinas, R.R. (1988). The intrinsic electrophysiological properties of mammalian neurons: Insights into central nervous system function. *Science* **242**, 1654–1664
- Lüscher, C., and Slesinger, P.A. (2010). Emerging roles for G protein-gated inwardly rectifying potassium (GIRK) channels in health and disease. *Nature Reviews Neuroscience* **11**, 301–315
- Maffei, A., and Fontanini, A. (2009). Network homeostasis: a matter of coordination. *Current Opinion in Neurobiology* **19**, 168–173
- Maisak, M.S., Haag, J., Ammer, G., Serbe, E., Meier, M., Leonhardt, A., Schilling, T., Bahl, A., Rubin, G.M., Nern, A., et al. (2013). A directional tuning map of *Drosophila* elementary motion detectors. *Nature* **500**, 212–216
- Mangan, S., and Alon, U. (2003). Structure and function of the feed-forward loop network motif. *PNAS* **100**, 11980–11985
- Marder, E., and Taylor, A.L. (2011). Multiple models to capture the variability in biological neurons and networks. *Nature Neuroscience* **14**, 133–138
- Marvin, J.S., Borghuis, B.G., Tian, L., Cichon, J., Harnett, M.T., Akerboom, J., Gordus, A., Renninger, S.L., Chen, T.W., Bargmann, C.I., et al. (2013). An optimized fluorescent probe for visualizing glutamate neurotransmission. *Nature Methods* **10**, 162–170

- Masuda, N., Hayashi, Y., Matsuyoshi, H., Chancellor, M.B., de Groat, W.C., and Yoshimura, N. (2006). Characterization of hyperpolarization-activated current (I_h) in dorsal root ganglion neurons innervating rat urinary bladder. *Brain Research* **1096**, 40–52
- Matsumoto, A., Agbariah, W., Nolte, S.S., Andrawos, R., Levi, H., Sabbah, S., and Yonehara, K. (2021). Direction selectivity in retinal bipolar cell axon terminals. *Neuron* **109**, 2928-2942.e8
- McCulloch, W.S., and Pitts, W. (1943). A logical calculus of the ideas immanent in nervous activity. *Bulletin of Mathematical Biophysics* **5**, 115–133
- McKenna, T., Davis, J., and Zornetzer, S.F. (1992). Single neuron computation
- Meier, M., and Borst, A. (2019). Extreme compartmentalization in a *Drosophila* amacrine cell. *Current Biology* **29**, 1545–1550
- Milo, R., Shen-Orr, S., Itzkovitz, S., Kashtan, N., Chklovskii, D., and Alon, U. (2002). Network motifs: simple building blocks of complex networks. *The Structure and Dynamics of Networks* **298**, 824–827
- Miyawaki, A., Llopis, J., Heim, R., Michael McCaffery, J., Adams, J.A., Ikura, M., and Tsien, R.Y. (1997). Fluorescent indicators for Ca^{2+} based on green fluorescent proteins and calmodulin. *Nature* **388**, 882–887
- Montell, C. (2012). *Drosophila* visual transduction. *Trends Neuroscience* **35**, 356–363
- Nakai, J., Ohkura, M., and Imoto, K. (2001). A high signal-to-noise Ca^{2+} probe composed of a single green fluorescent protein. *Nature Biotechnology* **19**, 137–141
- Nielsen, M.S., Axelsen, L.N., Sorgen, P.L., Verma, V., Delmar, M., and Holstein-Rathlou, N.H. (2008). Gap junctions. *Comprehensive Physiology* **2**, 0–105
- Nietzsche, F. (1882). Die fröhliche Wissenschaft (Chemnitz: Contumax GmbH & Co. KG)
- Nowak, L., Bregestovski, P., and Ascher, P. (1984). Magnesium gates glutamate-activated channels in mouse central neurones. *Nature* **307**, 462–465
- Orger, M.B., Smear, M.C., Anstis, S.M., and Baier, H. (2000). Perception of Fourier and non-Fourier motion by larval zebrafish. *Nature Neuroscience* **3**, 1128–1133
- Pak, W.L., and Pinto, L.H. (1976). Genetic approach to the study of the nervous system. *Annual Review of Biophysics* **5**, 397–448
- Pankova, K., and Borst, A. (2016). RNA-seq transcriptome analysis of direction-selective T4/T5 neurons in *Drosophila*. *PLoS ONE* **11**
- Papamakarios, G., and Murray, I. (2018). Fast likelihood-free inference of

- simulation models with Bayesian conditional density estimation
- Patriarchi, T., Cho, J.R., Merten, K., Howe, M.W., Marley, A., Xiong, W.H., Folk, R.W., Broussard, G.J., Liang, R., Jang, M.J., et al. (2018). Ultrafast neuronal imaging of dopamine dynamics with designed genetically encoded sensors. *Science* **360**, 1–8
- Perkins, L.A., Holderbaum, L., Tao, R., Hu, Y., Sopko, R., Mccall, K., Foos, M., Randkelv, S., Kelley, C., Namgyal, P., et al. (2015). The transgenic RNAi project at Harvard medical school : resources and validation. *Genetics* **201**, 843–852
- Pisokas, I., Rössler, W., Webb, B., Zeil, J., and Narendra, A. (2022). Anesthesia disrupts distance, but not direction, of path integration memory. *Current Biology* **32**, 1–8
- Podlaski, W.F., Seeholzer, A., Groschner, L.N., Miesenböck, G., Ranjan, R., and Vogels, T.P. (2017). Mapping the function of neuronal ion channels in model and experiment. *eLife* **6**, 1–22
- Poggio, T., and Reichardt, W. (1976). Visual control of orientation behaviour in the fly. *Quarterly Reviews of Biophysics* **9**, 377–438
- Puil, E., Gimbarzevsky, B., and Miura, R.M. (1986). Quantification of membrane properties of trigeminal root ganglion neurons in guinea pigs. *Journal of neurophysiology* **55**, 995–1016
- Raji, J.I., and Potter, C.J. (2021). The number of neurons in *Drosophila* and mosquito brains. *PLoS ONE* **16**, 1–11
- Rall, W. (1959). Branching dendritic trees and motoneuron membrane resistivity. *Experimental Neurology* **1**, 491–527
- Richter, F.G., Fendl, S., Drews, M.S., Borst, A., Richter, F.G., and Fendl, S. (2018). Glutamate signaling in the fly visual system. *iScience* **7**, 85–95
- Rivera-alba, M., Vitaladevuni, S.N., Mischenko, Y., Lu, Z., Scheffer, L., Meinertzhagen, I.A., Chklovskii, D.B., and Gonzalo, G. (2011). Wiring economy and volume exclusion determine neuronal placement in the *Drosophila* brain. *Current Biology* **21**, 2000–2005
- Rothfuss, J., Ferreira, F., Walther, S., and Ulrich, M. (2019). Conditional density estimation with neural networks: best practices and benchmarks
- Ruthotto, L., and Haber, E. (2021). An introduction to deep generative modeling. *arXiv* 1–26
- Schnupp, J.W.H., and King, A.J. (2001). Neural processing : The logic of multiplication in single neurons. *Current Biology* **11**, 640–642
- Serbe, E., Meier, M., Leonhardt, A., and Borst, A. (2016). Comprehensive

- characterization of the major presynaptic elements to the *Drosophila* OFF motion detector. *Neuron* **89**, 829–841
- Seyfarth, E., and Peichl, L. (2002). Vor 100 Jahren : Julius Bernstein (1839-1917) formuliert seine „Membrantheorie“. *e-Neuroforum* **4**, 2–4
- Shinomiya, K., Huang, G., Lu, Z., Parag, T., Xu, C.S., Aniceto, R., Ansari, N., Cheatham, N., Lauchie, S., Neace, E., et al. (2019). Comparisons between the ON- and OFF- edge motion pathways in the *Drosophila* brain. *eLife* **8**, 1–19
- Smotherman, M.S., and Narins, P.M. (1999). The electrical properties of auditory hair cells in the frog amphibian papilla. *The Journal of Neuroscience* **19**, 5275–5292
- Srinivasan, M. V., and Bernard, G.D. (1976). A proposed mechanism for multiplication of neural signals. *Biological Cybernetics* **21**, 227–236
- Stafstrom, C.E. (2007). Persistent sodium current and its role in epilepsy. *Current Review in Basic Science* **7**, 15–22
- Steriade, M., Datta, S., Paré, D., Oakson, G., and Curró Dossi, R. (1990). Neuronal activities in brain-stem cholinergic nuclei related to tonic activation processes in thalamocortical systems. *The Journal of Neuroscience* **10**, 2541–2559
- Takemura, S., Bharioke, A., Lu, Z., Nern, A., Vitaladevuni, S., Rivlin, P.K., Katz, W.T., Olbris, D.J., Plaza, S.M., Winston, P., et al. (2013). A visual motion detection circuit suggested by *Drosophila* connectomics. *Nature* **500**, 175–183
- Takemura, S., Nern, A., Chklovskii, D.B., Scheffer, L.K., Rubin, G.M., and Meinertzhagen, I.A. (2017). The comprehensive connectome of a neural substrate for ‘ON’ motion detection in *Drosophila*. *eLife* **6**, 1–16
- Tejero-Cantero, A., Boelts, J., Deistler, M., Lueckmann, J.-M., Durkan, C., Gonçalves, P., Greenberg, D., and Macke, J. (2020). sbi: a toolkit for simulation-based inference. *Journal of Open Source Software* **5**, 2505
- Thorson, J. (1966). Small-signal analysis of a visual reflex in the locust. *Kybernetik* **4**, 41–53
- Tochitsky, I., Helft, Z., Meseguer, V., Fletcher, R.B., Vessey, K.A., Teliás, M., Denlinger, B., Malis, J., Fletcher, E.L., and Kramer, R.H. (2016). How azobenzene photoswitches restore visual responses to the blind retina. *Neuron* **92**, 100–113
- Traub, R.D., and Miles, R. (1991). Neuronal networks of the hippocampus (Cambridge: Cambridge University Press)

- Tzivilivaki, A., Kastellakis, G., and Poirazi, P. (2019). Challenging the point neuron dogma: FS basket cells as 2-stage nonlinear integrators. *Nature Communications* **10**
- Unwi, P.N.T., and Zampighi, G. (1980). Structure of the junction between communicating cells. *Nature* **283**, 545–549
- Vandael, D., Okamoto, Y., Borges-Merjane, C., Vargas-Barroso, V., Suter, B.A., and Jonas, P. (2021). Subcellular patch-clamp techniques for single-bouton stimulation and simultaneous pre- and postsynaptic recording at cortical synapses. *Nature Protocols* **16**, 2947–2967
- Wang, Y., Ye, M., Kuang, X., Li, Y., and Hu, S. (2018). A simplified morphological classification scheme for pyramidal cells in six layers of primary somatosensory cortex of juvenile rats. *International Brain Research Organization Reports* **5**, 74–90
- Warmke, J.W., Reenan, R.A.G., Wang, P., Qian, S., Arena, J.P., Wang, J., Wunderler, D., Liu, K., Kaczorowski, G.J., Ploeg, L.H.T. Van Der, et al. (1997). Functional expression of *Drosophila para* sodium channels *Modulation by the membrane protein TipE and toxin Pharmacology. J.Gen.Physiol.* **110**, 119–133
- Wolf, S., Supatto, W., Debrégeas, G., Mahou, P., Kruglik, S.G., Sintes, J.M., Beaurepaire, E., and Candelier, R. (2015). Whole-brain functional imaging with two-photon light-sheet microscopy. *Nature Methods* **12**, 379–380
- Xu, C.S., Hayworth, K.J., Lu, Z., Grob, P., Hassan, A.M., Weinberg, R.J., and Hess, H.F. (2017). Enhanced FIB-SEM systems for large-volume 3D imaging. *eLife* **6**, 1–36
- Yamaguchi, S., Desplan, C., and Heisenberg, M. (2010). Contribution of photoreceptor subtypes to spectral wavelength preference in *Drosophila*. *PNAS* **107**, 5634–5639
- Yang, H.H., and Clandinin, T.R. (2018). Elementary motion detection in *Drosophila*: algorithms and mechanisms. *Annual Review of Vision Science* **4**, 1–21
- Yildizoglu, T., Riegler, C., Fitzgerald, J.E., and Portugues, R. (2020). A neural representation of naturalistic motion-guided behavior in the zebrafish brain. *Current Biology* **30**, 2321–2333
- Yin, T.C.T. (2002). Neural mechanisms of encoding binaural localization cues in the auditory brainstem. 99–159
- Zavatone-Veth, J.A., Badwan, B.A., and Clark, D.A. (2020). A minimal synaptic model for direction selective neurons in *Drosophila*. *Journal of Vision* **20**,

1-22

Zeleny, C. (1922). The effect of selection for eye facet number in the white bar-eye race of *Drosophila melanogaster*. *Genetics* **7**, 2-31

APPENDIX

5.1 Acknowledgements

First and foremost, I wish to thank Axel for having given me the opportunity to work in his laboratory. Despite being a renowned scientist and a director of the MPI for Neurobiology, his down to earth attitude, his humility, and his passion for science make him a role model to me. I deeply thank you for your trust and your support.

I wish to thank Lukas Groschner who taught me about electrophysiology and whose encounter was transformative. His teachings have made me into a better scientist. The scientific challenges we faced and overcame together are in hindsight the highlight of these past five years. Thank you for never giving up on me and for always being supportive in good and in bad times.

Furthermore, I am very grateful to the many people who supported me on my PhD journey: My TAC committee members, Ruben Portugues and Laura Busse for their advices and the time they spent discussing my projects. Jesus for always being ready to discuss scientific questions. I consider myself lucky that you have shared your passion for science and your friendship with me. Birte with whom I was very lucky to work with and who was a fantastic teammate. Amalia with whom I could always share a laugh and whose friendship has been a highlight of the past few years. Niko whose resolution and aspirations where a model for me to emulate. Tabea for always being ready to help me with her expertise, for her patience, and for her kindness. Aicha for many scientific discussions and for her selfless support of her coworkers. Renee whose joviality and interest in electrophysiology made my day. Georg for the countless interesting scientific discussions. Alexander Arenz for shortly being my supervisor and for teaching me about 2-photon imaging. Romina for always being ready to help me.

P1 for always being a refuge in hard times. The Borst lab for holding together and for making it possible to navigate the murky waters of the actual pandemic.

Finally, I wish to thank my parents and grandparents for always unconditionally supporting my scientific inquiry. Most importantly, I wish to thank Sandra for always supporting me in bad times and for sharing my happiness in good times. Without her, I would not be half the person and the scientist I am today.

5.4 List of manuscripts and author contributions

Manuscript 1

Groschner, L.N.*, **Malis, J.G.***, Zuidinga, B., and Borst, A. (2022). A biophysical account of multiplication by a single neuron. *Nature* 1–46

*These authors contributed equally: **Jonatan G. Malis**, Lukas N.

Groschner.

L.N.G., **J.G.M.**, and A.B. conceived the study, designed experiments, and ran model simulations. L.N.G. and **J.G.M.** performed and analysed electrophysiological recordings. L.N.G., **J.G.M.**, and B.Z. performed histological analyses and B.Z. conducted and analysed behavioural experiments. The manuscript was written by L.N.G and edited by all authors, chiefly by B.Z.

Manuscript 2

Malis, J.G.*, Groschner, L.N.*, and Borst, A. Differential temporal filtering in a small neuronal network.

*These authors contributed equally: **Jonatan G. Malis**, Lukas N. Groschner.

J.G.M., L.N.G., and A.B. conceived the study, designed experiments, and ran model simulations. **J.G.M.** and L.N.G. performed and analyzed electrophysiological recordings. The manuscript was written by **J.G.M.** and edited by all authors.

.....
Dr. Lukas Groschner

.....
Prof. Dr. Alexander Borst (supervisor)